File ID	uvapub:154854
Filename	Thesis
Version	final

SOURCE (OR PART OF THE FOLLOWING SOURCE):

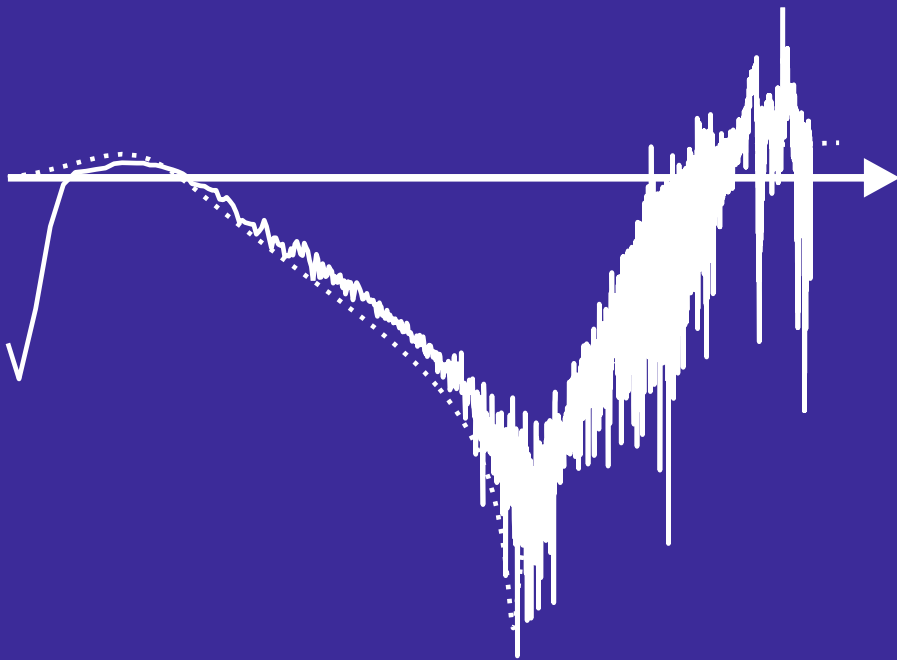|	
Type	PhD thesis
Title	Stabilisation and precision pointing quadrupole magnets in the Compact Linear Collider (CLIC)
Author(s)	S.M.J. Janssens
Faculty	FNWI
Year	2015

FULL BIBLIOGRAPHIC DETAILS:
   http://hdl.handle.net/11245/1.437914

CERN-THESIS-2015-004
14/01/2015

Stabilisation and precision pointing quadrupole magnets in the Compact Linear Collider (CLIC)

Stef M.J. Janssens

Stabilisation and precision pointing quadrupole magnets in the Compact Linear Collider (CLIC)

Stef M.J. Janssens

Stabilisation and precision pointing quadrupole magnets in the Compact Linear Collider (CLIC)

Stabilisation and precision pointing quadrupole magnets in the Compact Linear Collider (CLIC)

Stabilisation and precision pointing quadrupole magnets in the Compact Linear Collider (CLIC)

Acknowledgements

Contents

Chapter 1

Introduction

1.1 Why future particle accelerators?

A more fundamental model of particles and fields is expected to exist beyond the Standard Model of particle physics. The Standard Model for example does not contain gravity and dark matter. It has been theorized that this model can be investigated by using TeV (10^{12} electron-Volt) particle accelerators. The most famous is the Large Hadron Collider (LHC), a circular machine, which performs collisions between proton beams up to 14 TeV of centre of mass energy [1] and is capable of performing collisions between Lead nuclei (Pb-Pb) up to 2.76 TeV/nucleon [2]. A proton is filled with quarks, anti-quarks and gluons interacting according to the rules of Quantum Chromodynamics (QCD). The various possible collisions allow scientists to probe a wide energy region for particles, making a hadron collider a good discovery machine. As a next step, detailed research is done with lepton colliders, usually with electrons and positrons; producing cleaner collisions at a certain energy allowing to produce the same type of particle over and over in order to study it in detail. An overview of the history of particle colliders is shown in Fig. 1.1.

There are two main configurations for a particle collider. It can be a circular or a linear machine. In a linear collider, two beams are accelerated at opposite sides of the Interaction Point (IP) at which they collide. In a circular machine the beam passes the IP multiple times. However, when accelerating particles, the energy loss per turn is dependent on the beam energy E_b, the particle mass m and the radius of the collider R [4] as:

$$dE_b \propto (E_b)^4/(m^4 R). \tag{1.1}$$

Since electrons and positrons have a much smaller mass than a proton ($m_e = 0.5110$ MeV/c^2 versus $m_p = 938.272$ MeV/c^2), they are much more susceptible to energy loss by radiation. One option would be to increase the radius of the accelerator. However this will become increasingly expensive as more magnets are
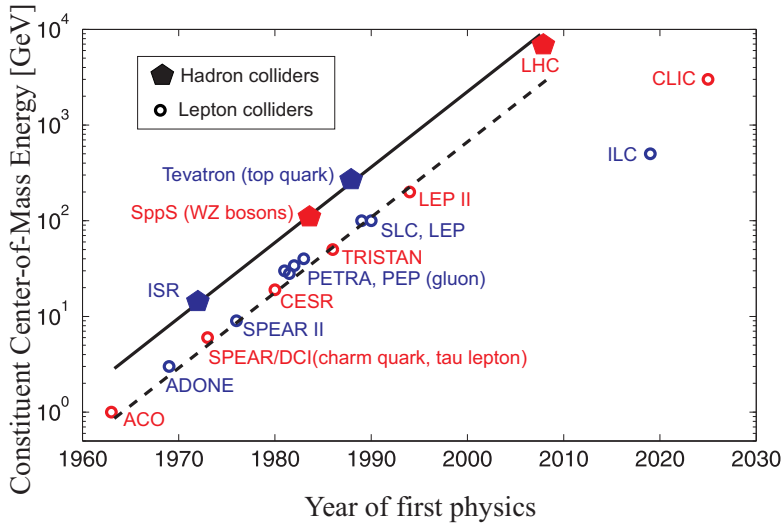
Figure 1.1: *History of particle accelerators and their discoveries: Both hadron colliders (pentagons) and lepton colliders (circles) are indicated (adapted from Ref. [3]).*

needed to bend the beam (and the LHC already has a circumference of 27 km). The point where a linear collider becomes more beneficial for lepton colliders is situated around 200 GeV according to Ref. [4].

1.2   The CLIC project

One of the proposed linear colliders to complement the LHC, is the Compact Linear Collider (CLIC) (see Fig. 1.2).

CLIC is a linear collider with a 3 TeV centre of mass collision energy in the interaction point with a luminosity of 2×10^{34} cm^{-2}s^{-1} [5]. In order to reach this high energy while achieving high luminosity, a novel two-beam acceleration scheme is proposed. In this scheme the usual klystron powering is replaced by a second Drive Beam. This Drive Beam consists of pulses of electrons with a 1 GHz repetition rate. These pulses are accelerated in two Drive Beam linear accelerators until an energy of 2.38 GeV. The pulses are recombined in the Delay Loops and Combiner Rings (CR1 and CR2) in order to increase the frequency of the pulses to the required repetition rate of 12 GHz. This scheme results in a Drive Beam with a peak current of about 100 A and a beam energy of 2.38 GeV. The Drive Beam pulses are redirected through power extraction elements in order to generate RF power for the accelerating structures of the Main Beams. This RF power is used to accelerate the electrons and positrons with a gradient
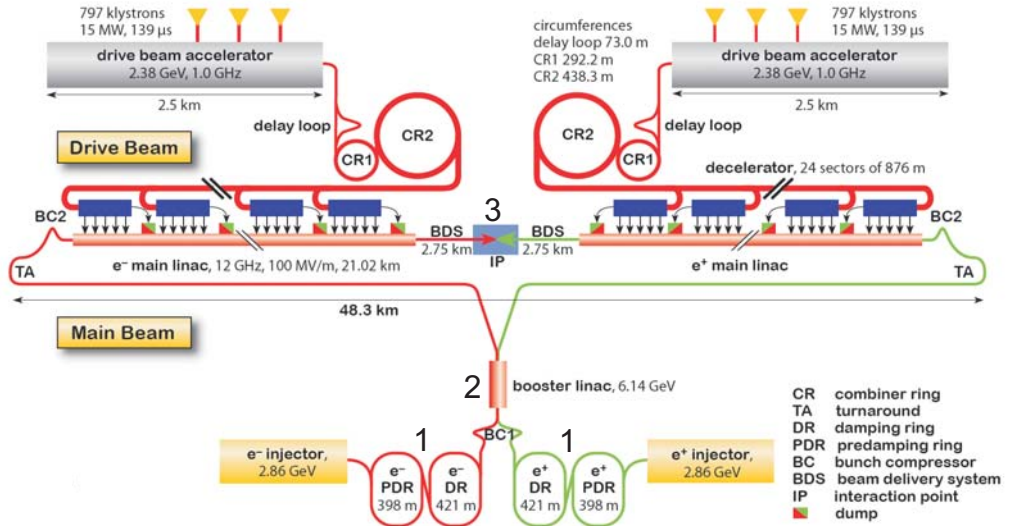
Figure 1.2: *The Compact Linear Collider (CLIC) with a novel two beam accelerator scheme. A drive beam is generated and accelerated up to 2.38 GeV after which it is recombined in combiner rings to reach the required 12 GHz repetition rate and 100 A peak current. The power of this drive beam is transferred to the main lepton beam along the two main linacs after which they collide in the interaction point (3) and physics data can be taken [4].*

of 100 MV/m. Such an accelerating gradient would be much more costly with traditional klystrons [5].

The electrons, for the beam used for the physics experiments, are produced by shining a circularly polarized laser on a GaAs cathode, causing it to emit polarized electrons. In another process, positrons are created by shooting electrons at a target. The Main Beams are pre-accelerated in the injector linacs and then enter the Damping Rings for emittance reduction (1). The beams are damped to 500 nm and 5 nm in the horizontal and vertical planes respectively, expressed in the standard deviation of the beam distribution, at the exit of the injector complex. The small emittance beams are further accelerated in a booster linac (2) before being transported through the main tunnel to the turnarounds [5]. After the turnarounds the beams are accelerated in the main linac up to the required energy at the interaction point (3) where the beam will have a transverse size of $e_y = 1$ nm in the vertical direction and $e_x = 40$ nm in the lateral direction [6]. The challenge to transport these small beam sizes through the main linac to the interaction point will be the subject of this thesis. An overview of the CLIC main parameters is given in Table 1.1.

Description	500 GeV	3 TeV
Total (peak 1%) luminosity [cm^{-2}s^{-1}]	2.3(1.4)×10^{34}	5.9(2.0)×10^{34}
Total site length [km]	13.0	48.4
Loaded accel. gradient [MV/m]	80	100
Main Linac RF frequency [GHz]	12	12
Beam power/beam [MW]	4.9	14
Bunch charge [10^9 e$^+$/e$^-$]	6.8	3.72
Bunch separation [ns]	0.5	0.5
Bunch length [μm]	72	44
Beam pulse duration [ns]	177	156
Repetition rate [Hz]	50	50
Hor./vert. IP beam size [nm]	202/2.3	40/1
Electric Power requirement [MW]	272	589

Table 1.1: *CLIC main parameters for the 500 GeV and 3 TeV configurations; adapted from Ref. [5].*

1.3   Research motivation and requirements

The linear configuration of CLIC creates several new challenges. One of these challenges is that for a linear collider, the beams cross the interaction point only once. As a consequence, the collision brightness or luminosity needs to be as high as possible.

If the collision process is performed correctly then the luminosity $\mathcal{L}$ is described by:

$$\mathcal{L} = \frac{A}{e_x e_y},\tag{1.2}$$

where A is a function of a combination of several parameters depending on the accelerator settings, and the vertical e_y and lateral e_x size of the beam at the interaction point [1].

To get the highest possible luminosity the product of the lateral and vertical beam size needs to be as low as possible, resulting in a high particle density and collision rate. A second effect on the performance of the beam is called the disruption $\mathcal{D}$ which is a measure of beam turbulence at the collision point diminishing the collision effectiveness [7]. The disruption is a function of a parameter B, which again is a combination of several parameters depending on the accelerator settings, and both the vertical and lateral beam size at the interaction point [7]:

$$\mathcal{D} = \frac{B}{e_x + e_y}.\tag{1.3}$$

To keep the disruption low the sum of the lateral and vertical beam size needs to be as high as possible. In order to optimize both the requirements for the luminosity and the disruption, one of the beam axes needs to be much smaller than the other. It was decided that for CLIC the beam would have a vertical size of $e_y = 1$ nm and a lateral beam size of $e_x = 40$ nm at the interaction point [6]. The shape and size of the beam is thus of utmost importance.

The main linear accelerator will be built up out of modules. Each module will have an accelerating structure to accelerate the particles, a dipole magnet to steer the beam, and a quadrupole magnet to keep the beam in the required shape. The focus of this thesis will lie with the quadrupole magnets. An example of the magnetic field lines of a quadrupole magnet (left panel) and the forces exerted on an electron moving into the page (right panel) is shown in Fig. 1.3.
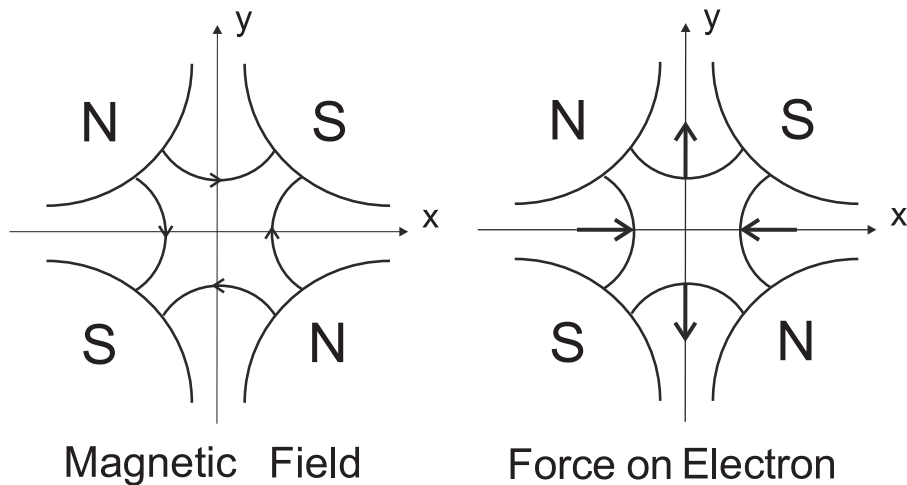
Figure 1.3: *The magnetic field lines of a quadrupole (left) and the force components on an electron due to the magnetic field for an electron moving into the page (right) [8].*

From the forces it can be inferred that a particle that deviates from the y-axis is forced back towards the centre of the magnet. However the opposite is true for deviations from the x-axis. Therefore quadrupoles are usually used in pairs, one focusing towards the x-axis and one towards the y-axis, in this way focusing all particles to the centre of the magnet. If all quadrupoles are perfectly aligned, both positrons and electrons are delivered at the same location at the interaction point.

However all the quadrupoles of the different modules will never be perfectly aligned, and a misalignment will affect the particles with a slightly different energy in a different way. The particles will start to oscillate along the beam line differently, increasing the effective cross section of the beam and decreasing lu-

minosity. This misalignment can be both static, due to installation tolerances, or
dynamic due to vibrations coming from the ground, ventilation, vacuum pumps
etc. as is shown in Fig. 1.4. A first stage alignment will be performed with eccen-
tric cam motors which will realign the magnets to 1 μm in a range of 3 mm while
the beam is off. On top of this pre-alignment system, the to be designed sys-
tem will have to perform the positioning to the nanometre and provide vibration
isolation.
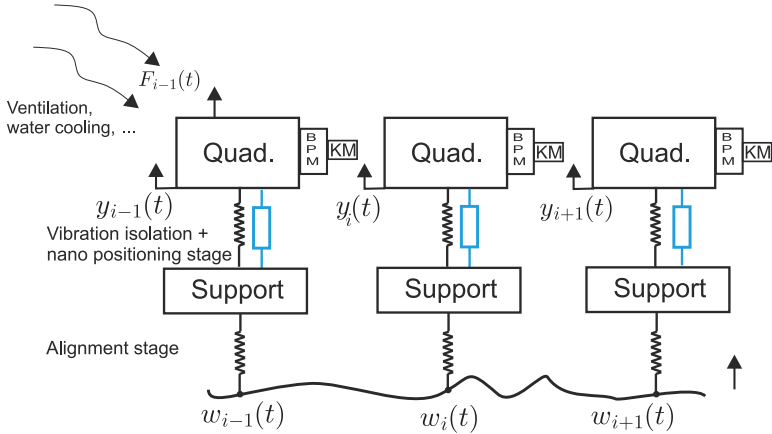
Figure 1.4: *A schematic overview of a part of the Main Linear Accelerator
with the influences of ground vibrations (w_i) and vibrations coming from venti-
lation, cooling, etc. (F_i) on quadrupole vertical displacement y_i. Beam position
monitors (BPM) measure the beam position at the quadrupole and kicker dipole
magnets (KM) can steer the beam in a plane. An alignment stage performs a
first alignment when the beam is off and the vibration isolation and positioning
stage, subject of this thesis, will be active during the beam.*

In order to estimate the maximum allowed alignment error due to ground
motion, an estimation for the total effect of the luminosity loss ($\Delta\mathcal{L}$), integrated
over the entire beam length, is approximated by [9]:

$$\langle\Delta\mathcal{L}\rangle = \int\int P_w(\omega, n)|T_{wy}(\omega)|^2 G(n)dnd\omega, \qquad (1.4)$$

with $P_w(\omega, n)$ the two dimensional power spectral density (PSD) of the ground
vibrations depending on the frequency ω and the wavelength λ with $n = 2\pi/\lambda$,
$|T_{wy}(\omega)|^2$ the transfer function from the ground to the quadrupole centre and $G(n)$
is called the sensitivity function of the beam through the quadrupole (or any other
accelerator element). For more information see Ref. [10]. The same is done for
the induced forces $F_i(t)$ coming from the ventilation, cooling *etc.* with $|T_{Fy}(\omega)|^2$
the transfer function between the forces and the centre of the quadrupole magnet.

In order to have a first clear requirement it was estimated that the quadrupole vibrations should be lower than $\sigma_y = 1.5$ nm in vertical and $\sigma_x = 5$ nm integrated root mean square (RMS) at 1 Hz, defined by [11]:

$$\sigma_y = \sqrt{\int_{2\pi}^{\infty} P_y(\omega)d\omega}. \tag{1.5}$$

with $P_y(\omega)$ the power spectral density (PSD) of the residual vibrations in y-direction of the quadrupole, integrated for n. The vibrations in the z-direction are not transmitted to the beam, and hence do not require reduction.

This problem of static and dynamic misalignment of the quadrupoles is tackled through a beam based orbit feedback and an active mechanical stabilisation and positioning system. Figure 1.5 shows a schematic representation of the collaboration between mitigation techniques. For the beam based orbit feedback, the beam position is measured with Beam Position Monitors (BPM) as is shown in Fig. 1.4. The result of this measurement, passes through a controller and is sent to a kicker dipole magnet which deflects the beam to the required position. Alternatively, the quadrupole magnet position can be changed, imposing a dipole field to steer the beam.
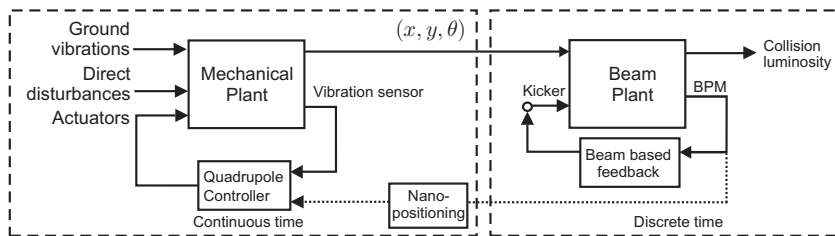
Figure 1.5: *Block diagram of the combination of beam based feedback and stabilisation. Ground motion (w) and Direct disturbances (F) disturb the mechanical plant changing the position (x, y, θ) of the quadrupole. These displacements have an effect on the beam (and luminosity) through the beam plant. To mitigate this effect, beam position monitors measure the position of the beam which is used as an input to the kicker dipole magnets or to reposition the quadrupoles, thus leading to a dipole component in the magnet as seen by the beam, resulting in a correction of the beam trajectory. Locally, a vibration sensor measures the vibrations of the quadrupole. This measurement is used to control actuators in order to reduce the transmitted vibrations to the quadrupole [12].*

The beam based feedback reduces the transmissibility especially at low frequencies (under 1 Hz) and at the multiples of 50 Hz, to reduce the effect of the induced noise coming from the main power grid. However it amplifies at half of the repetition rate of 50 Hz and its multiples. More information can be found in reference [10]. For these frequencies, the mechanical stabilisation, subject of this

thesis, is used. Fig. 1.6 shows the PSD of the ground motion measured in the LHC tunnel. The situation for the CLIC tunnel is expected to be similar.
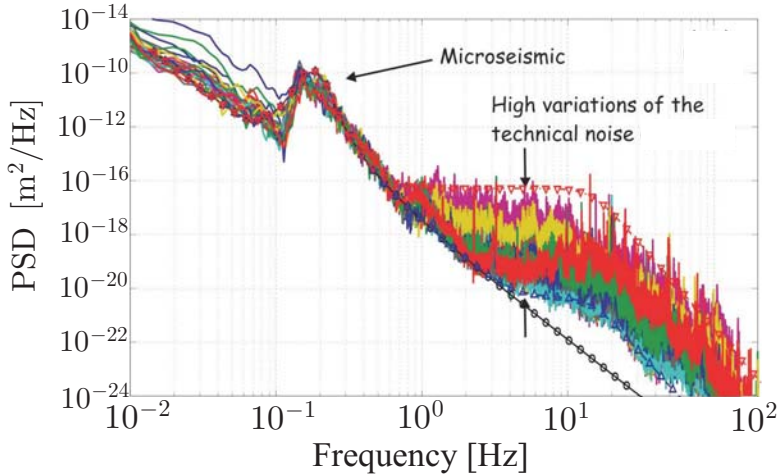
Figure 1.6: *Results of ground motion measurements, at different locations at the LHC site. Measurements near the experiments and near cryogenic pumps had more technical noise above 1 Hz than measurements in parts of the tunnel with little equipment. The bandwidth above 1 Hz hence shows high variations in technical noise. Below 1 Hz vibrations are dominated by vibrations coming from the earth. The micro-seismic peak at 0.17 Hz is due to incoming sea waves for example [13].*

The main vibration sources are located at frequencies below 50 Hz. Since the beam based control reduces vibrations below a few Hz, the main focus for the active stabilisation system will be in the bandwidth between 1 and 50 Hz. In addition, resonances should be avoided or damped in the range between 50 and 100 Hz. The goal of this thesis is to research the possibilities for reducing quadruple vibrations due to ground motion and indirect forces, by using a vibration isolation and positioning system. This system has to be developed for quadrupoles with a length from 500 to 2000 mm and a mass ranging from 100 to 400 kg.

An additional requirement is to reposition the quadrupoles every 20 ms (between beam pulses) with steps of tens of nano-metres with a precision of ±1 nm. This allows to give an additional option to 'kick' the beam back to its required position reducing the number of expensive kicker magnets needed. Further the direct environment of the future CLIC collider is subjected to stray magnetic fields, *e.g.* from the stray magnetic fields of the quadrupole and the kicker. This excludes all electromagnetic equipment in the vibration isolation system, as there is a high risk of interference.

Finally, during operating conditions, the stabilisation and positioning system will also be subjected to radiation. Preliminary calculations give in a worst case scenario, close to the beam, absorbed doses of 250 Gy/year [14], 1 MeV Neutron

Requirement	
stabilisation requirement vertical	$\sigma_y = 1.5$ nm
stabilisation requirement horizontal	$\sigma_x = 5$ nm
Repositioning step	10 nm
Repositioning frequency	every 20 ms
Repositioning precision	± 1 nm
High radiation environment	300 Gy/year
Static stray magnetic fields of quadrupole	0.15×10^{-4} T at 0 Hz

Table 1.2: *The requirements for the vibration isolation and positioning system for the main beam quadrupoles of CLIC.*

Equivalent Fluence of 10^{10} cm^{-2} and < 20 MeV Hadron Fluence of 10^8 cm^{-2} normalized to 180 days [15].

The requirements for the stabilisation and positioning system are summarized in Table 1.2.

This thesis is structured as follows. In chapter 2, an overview of existing vibration isolation strategies is presented and the state of the art of several components is shown. Two possible strategies are chosen and investigated in chapter 3 through simplified modelling. The multiple degree of freedom system and the effects on the control system are presented in chapter 4. The consequences of implementing the designed control system in an accelerator environment is researched in chapter 5. In chapter 6 the results of a step by step experimental program are shown. Finally, the conclusions and future work are described in chapter 7.

Chapter 2

Isolation strategies

2.1 Introduction

In this chapter several vibration isolation systems are investigated as shown in Fig. 2.1. The basic mass spring system for isolation purposes is described in section 2.2.
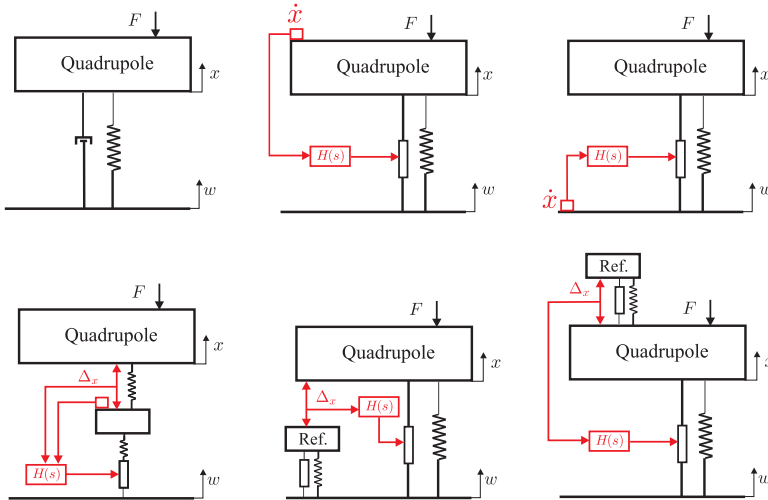
Figure 2.1: *Schematic view of various approaches to vibration isolation systems which will be addressed in this chapter. The spring mass system is presented on the top left (see section 2.2). A simple feedback isolator is shown in middle and the feed-forward configuration is described in the top right panel (see section 2.3). A stabilisation table produced by the TMC company (see Refs. [16], [17] and [18]) is displayed on the bottom left. Finally a stabilisation system using a reference mass on the ground and on top is represented in bottom middle and right panels respectively (see section 2.4).*

Active vibration control through feedback and feed-forward configurations are presented in section 2.3. Section 2.4 shows several vibration isolation strategies reported on in the literature.

2.2   Mass spring system

Vibration isolation can be done in numerous ways. The most simple approach is putting a mass M (the quadrupole in our case) on a spring with stiffness k and dashpot with damping coefficient c.
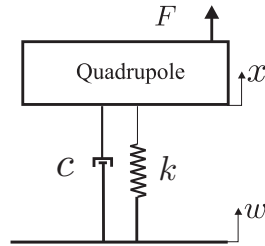
Figure 2.2: *Schematic view of a basic mass spring system.*

The equation of motion of the mass is given by:

$$M\ddot{x} + c(\dot{x} - \dot{w}) + k(x - w) = F. \tag{2.1}$$

The variable w represents the vibrations coming from the ground and F represents the direct forces on the magnet. The position x is then recalculated in the Laplace domain to be:

$$X(s) = \frac{cs + k}{Ms^2 + cs + k}W(s) + \frac{1}{Ms^2 + cs + k}F = T_{wx}W(s) + T_{Fx}F(s). \tag{2.2}$$

The first term T_{wx} is called the transmissibility between the ground motion w and the quadrupole position x. The second term T_{Fx}, represents the transmissibility between the external force F and the position of the quadrupole x. This is also called the compliance of the system.

The transmissibility T_{wx} for a typical mass spring system with different values of c is shown in Fig. 2.3. It has a resonance at $\omega_n = 2\pi f_n = \sqrt{\frac{k}{M}}$ rad/s. For frequencies lower than this natural frequency the ground and the quadrupole move together ($T_{wx}(s \to 0) = 1$). At frequencies higher than $\sqrt{2}\omega_n$, the transmissibility $T_{wx} < 1$. The effect of the ground vibrations on the movement of the quadrupole is reduced. The lower ω_n the larger the bandwidth of isolation. At the natural frequency, the vibrations coming from the ground are amplified while they are transmitted to the quadrupole. In order to reduce this amplification, a dashpot can be used. The use of a dashpot however reduces the downward slope of the

transfer function after the resonance frequency. This is unwanted behaviour as the steeper the slope, the better the vibration isolation as illustrated in Fig. 2.3.
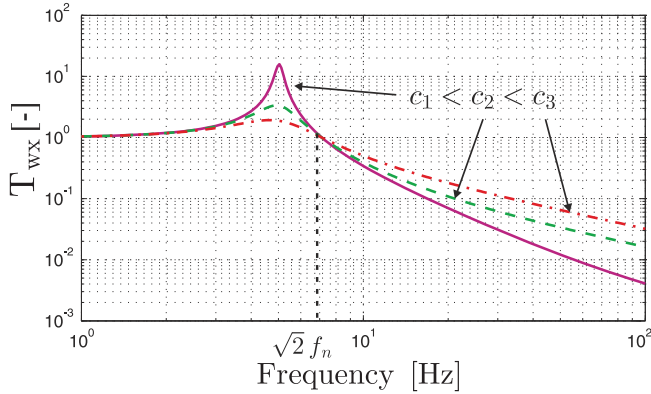
Figure 2.3: *Transfer function of a basic mass spring system with several different viscous damping factors.*

2.3   Active control of a mass spring system

To perform vibration isolation at low frequencies with the passive isolation method, the resonance ω_n has to be as low as possible. This is done by reducing the stiffness k as is shown in Fig. 2.4 (left panel). Lowering the stiffness has the effect of increasing the compliance of the system which is shown in Fig. 2.4 (right panel). The lower the compliance, the less sensitive the system is to disturbance forces.
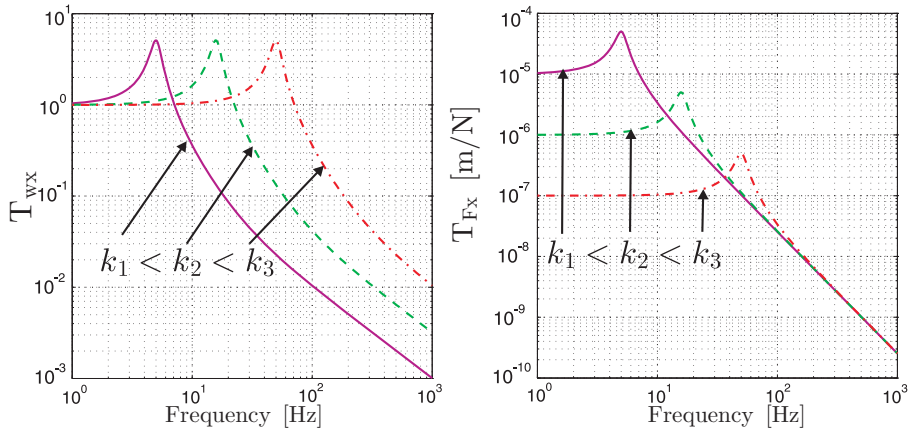
Figure 2.4: *The effect of the stiffness on the transfer function between the ground w and the mass x (left panel) and the transfer function between the disturbance force F and the mass position x (right panel).*

This trade-off between isolation bandwidth and compliance is a known effect for passive isolation systems. One way to avoid this trade-off is with active control either through feedback or feed-forward control.

2.3.1   Feedback system

To avoid the trade-off between isolation bandwidth and compliance, an active control system consisting of a sensor and an actuator can be used. A schematic representation of an active feedback control system is given in Fig. 2.5.
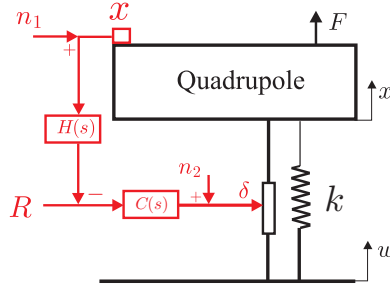
Figure 2.5: *Set up for an actively controlled mass spring system. A sensor measures the position x of the quadrupole with the addition of a certain amount of sensor noise n_1, while the actuator changes the quadrupole position with a displacement δ disturbed by the actuator noise n_2, in order to minimize the error to the requested position R.*

The equation of motion for this system is given by:

$$M\ddot{x} + k(x - w - \delta) = F, \tag{2.3}$$

with δ the elongation of the actuator. This elongation is given in the Laplace domain by:

$$\Delta(s) = C(s)(R - H(s)(X(s) + N_1(s))) + N_2(s), \tag{2.4}$$

with $C(s)$ the control filters and gains, $R(s)$ the requested position, $H(s)$ the sensor transfer function, $N_1(s)$ induced noise (sensor, ADC,...) and $N_2(s)$ secondary induced noise (actuator, DAC,...). Implementing this in Eq. (2.3) and rearranging terms gives a new expression for the quadrupole position:

$$\begin{aligned}
X(s) =& GW + GCR - GCHX - GCHN1 + GN_2 + T_{Fx}F \\
=& \frac{G}{1+GD}W + \frac{GC}{1+GD}R - \frac{GD}{1+GD}N_1 + \\
& \frac{G}{1+GD}N_2 + \frac{T_{Fx}}{1+GD}F(s),
\end{aligned} \tag{2.5}$$

with $G = T_{wx} = \frac{k}{Ms^2+ks}$ the passive transmissibility between the ground $W(s)$ and the quadrupole position $X(s)$ and $D(s) = C(s)H(s)$. The Laplace variable s was omitted in this equation to improve readability. For the quadrupoles, it is not the actual position x which is of interest, but the closed loop error signal for a given position (E_{cl}). In order to avoid a frequency component in R, which is not observable by the sensor, R is filtered through an input shaping filter (H_i) similar to the sensor sensitivity function (H). This is a standard practice according to Ref. [19]. The corresponding closed loop error is given by:

$$
\begin{aligned}
E_{cl} = R - X &= \frac{1}{1+GD}R - \frac{G}{1+GD}W + \frac{GD}{1+GD}N_1 \\
&\quad - \frac{G}{1+GD}N_2 - \frac{T_{Fx}}{1+GD}F(s) \\
&= SR - SGW + \Im N_1 - GSN_2 - ST_{Fx}F,
\end{aligned}
\tag{2.6}
$$

with $S = \frac{1}{1+GD}$ the sensitivity function to the error related to R and $\Im = 1 - S$ the complementary sensitivity curve related to the error related to the sensor noise n_1.

As an example we take a spring mass system with a natural resonance at $f_n = \frac{1}{2\pi}\sqrt{\frac{k}{M}} = 350$ Hz. A sensor measures the position with a sensitivity curve resembling a second order high pass filter at 1 Hz while the input signal R is equally filtered. The controller $(C(s))$ consists of a gain $(g = 1)$. The transfer function between the quadrupole position (x) and the ground motion (w) is represented by (T_{wx}) and shown in Fig. 2.6.
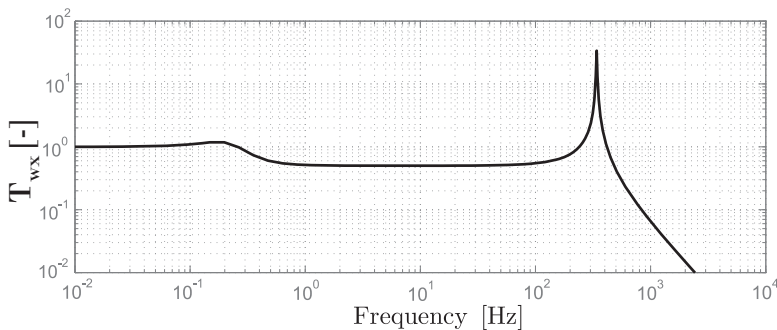
Figure 2.6: *The transfer function between the quadrupole position (x) and the ground motion (w) with $R = 0$, for a spring mass system with a $f_n = 350$ Hz and a second order high pass filter as a controller.*

The sensitivity and its complementary for this system are presented in Fig. 2.7. This plot shows a classical trade-off in an actively controlled system; in order to keep the influence of both the disturbance due to ground motion (W) and the sensor noise N_1 small and simultaneously keep the error E_{cl} due to R small, both

the sensitivity S and the complementary sensitivity $\Im$ have to be small. However this is not possible as they are each others complement.
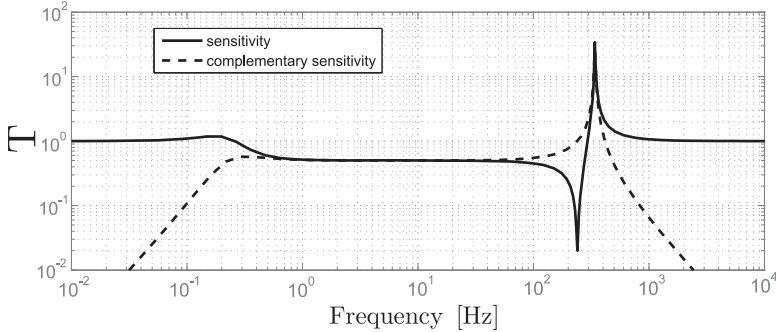
Figure 2.7: *The sensitivity and its complementary for a spring mass system with a $f_n = 350$ Hz and a second order high pass filter and gain ($g = 1$) as a controller.*

Therefore the sensor will have to be carefully designed so that N_1 is small in the bandwidth where the transmissibility T_{wx} of W to X has to be reduced.

There are three basic ways to perform active feedback [20]. There is acceleration feedback, by using $\ddot{x}$, velocity feedback by using $\dot{x}$ and position feedback by using x as a feedback signal. Implementing these in the closed loop transfer function and omitting the dashpot for simplicity results in:

$$T_{wx} = \frac{G}{1+GD} = \frac{k}{Ms^2 + k + kD} = \frac{k}{(M+kg_a)s^2 + ksg_v + k(1+g_p)}. \quad (2.7)$$

By using an acceleration feedback and a gain g_a, virtual mass is added to the system. In this way the natural frequency of the system is reduced artificially, increasing the bandwidth of the passive isolation as can be seen in Fig. 2.8. Performing velocity feedback or "sky-hook" control, adds a dashpot to the "sky" as it uses the absolute velocity of the payload instead of the relative velocity between the payload and the ground to damp the system, as is done by a conventional dashpot. This allows to perform damping without reducing the drop off at higher frequency (see Fig. 2.8) as was the case with the passive damping shown in Fig. 2.3.

These two approaches require that the natural frequency, and thus the stiffness is quite low to avoid excessively high control forces due to the high bandwidth of the system. By using a displacement feedback, the stiffness of the system is increased with a spring attached to the sky since the absolute position is measured. This allows to increase the stiffness (and thus reducing the compliance of the system) and allows to reduce the transmissibility of the vibrations coming from the ground ($W(s)$) to the quadrupole as is shown in Fig. 2.8. Displacement feedback would be an ideal solution for the stabilisation problem of the quadrupole.
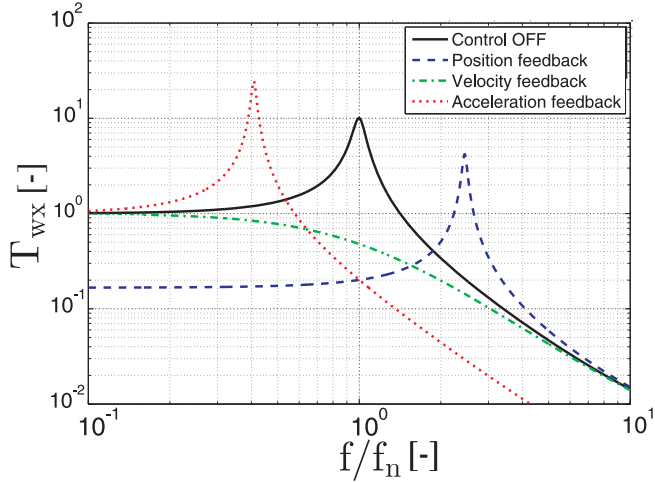
Figure 2.8: *Transfer functions between the ground w and the payload mass x for different active feedback systems with a frequency scale normalized to the natural frequency $f_n = 2\pi \sqrt{\frac{k}{M}}$ [20].*

A feedback system can however be unstable. This is most easily seen by looking at the solution for the differential equation of the system given by Eq. (2.3). This is always of the form:

$$x(t) = \sum_{i=1}^{n} K_i e^{p_i t}, \tag{2.8}$$

where K_i represents the gains and p_i the poles or resonances of the system. If the poles are positive, then $x(t)$ will grow exponentially and the system will be unstable. Therefore it is required that all poles have a negative real part. The poles of the system can be found by solving the denominator of the transfer function between the measured d.o.f. x and the actuator input δ for s. For example for the passive system, without damping, given by Eq. (2.1) the resulting poles are given by:

$$p_{1,2} = \pm i \sqrt{\frac{k}{M}} = \omega_n. \tag{2.9}$$

The zeros or anti-resonances can be calculated from the numerator of the transfer function between the measured d.o.f. and the actuator input, solving for s. If a gain is applied in the controller of the feedback, then the poles will start to move on a path towards the zeros or infinity. This movement is plotted in a graph called the root-locus of the system. The path of the poles is determined by the number of poles and also by the number of zeros calculated from the numerator of the transfer function. A pole will always move towards a zero unless there are

more poles (n) than zeros (m). Then the pole will follow an asymptote with an angle ϕ_l radiating from a position α given by [19]:

$$\phi_l = \frac{180° + 360°(l-1)}{n-m}, l = 1, 2, ..., n-m,$$

$$\alpha = \frac{\sum p_i - \sum z_i}{n-m}. \tag{2.10}$$

An example of this is shown in Fig.2.9 (left panel). There are two poles and no zeros, resulting in an asymptote aligned with the imaginary axis. The root-locus for the position, velocity and acceleration feedback is shown in Fig. 2.9. For position feedback there are no zeros resulting in two asymptotes parallel to the imaginary axis. The poles move outward on the imaginary axis, increasing the natural frequency as a higher gain adds more stiffness to the system. Velocity feedback introduces a zero in the origin coming from the derivation. Now there is one asymptote on the real axis and the other pole moves towards the zero. For a small gain, the two poles move on a quarter circle. The radius of the circle is given by the natural frequency of the system ω_n, and the sine of the angle between the imaginary axis and the pole represents the damping ratio ξ. A system is thus critically damped when the poles first touch the real axis. By performing acceleration feedback a second zero is introduced and both poles move towards the origin of the root-locus, so both the natural frequency and the damping of the system is reduced.

More complex systems will have additional poles risking to have a pole go towards the right half plane of the root-locus, making the real part positive and the system unstable. One way to avoid this is to use a feed-forward strategy.

2.3.2   Feed-forward control

By using a sensor on the ground the induced vibrations are measured and the effect on the magnet can be estimated and the transmissibility can be reduced. As a result Eq. (2.4), representing the actuator extension changes to:

$$\Delta(s) = C(s)(R - H(s)(W(s) + N_1(s))) + N_2(s), \tag{2.11}$$

resulting in a new expression for the position of the quadrupole:

$$X(s) = (1 - CH)GW + GCR - GCHN_1 + GN_2 + T_{Fx}F. \tag{2.12}$$

A feed-forward system thus only has an effect on the transmissibility T_{wx}. There is no effect on the compliance T_{Fx} and there is no effect on the tracking capability in relation to the requested position $R(s)$. Therefore, in general a feedback system is preferred.

There are several possible configurations to practically perform position feedback. The next section will give an overview of position feedback systems used for vibration isolation found in the literature.
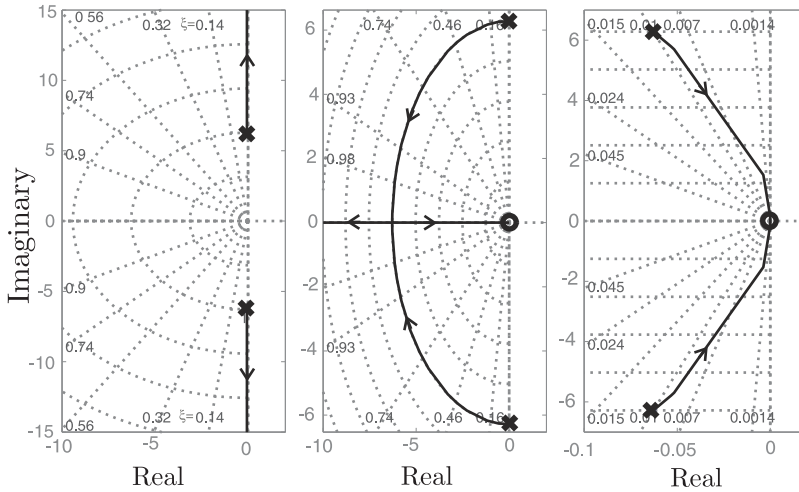
Figure 2.9: *The root-locus showing the position of the poles (indicated by X) and zeros (indicated by O) as a function of gain. Movements of the poles are indicated for position feedback (left panel); velocity feedback (middle panel); acceleration feedback (right panel).*

2.4 Overview of active feedback systems

This section will give an overview of several position feedback systems used for vibration isolation found in the literature Refs. [16, 17, 18, 21, 22, 23, 24]. Many more systems exist that use active damping of the resonances and passive isolation. These will not be modelled here, as they mainly use the passive drop off to perform vibration isolation which was shown to be too sensitive to external forces in section 2.2. An overview table of these systems is given in Appendix A.

2.4.1 Stiff actuator with intermediate mass and elastomer

With an elastomer between an intermediate mass and the payload on top of a stiff actuator a soft strategy can be created. This solution has been patented by the Technical Manufacturing Corporation (TMC) and is described in Refs. [16], [17] and [18]. Instead of using an elastomer directly between the piezo and the actuator, an intermediate mass is used to reduce the frequency of the first mode of the system. Two control loops are described in this section that are based on this strategy. One with a geophone as sensor and one with a capacitive gauge. A schematic view of the system is shown in Fig. 2.10.

The equations of motion are given by:
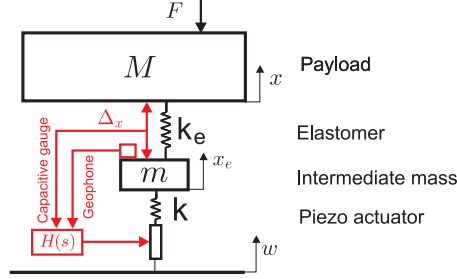
Figure 2.10: *Schematic view of a system with a stiff piezo actuator and elastomer.*

$$m\ddot{x}_e + k(x_e - w - \delta) + c(\dot{x}_e - \dot{w}) + k_e(x_e - x) + c_e(\dot{x}_e - \dot{x}) = 0,$$
$$M\ddot{x} + k_e(x - x_e) + c_e(\dot{x} - \dot{x}_e) = F. \tag{2.13}$$

If we define $X_1 = \begin{bmatrix} x_e & x \end{bmatrix}^T$ and $X_2 = \dot{X}_1$, then this set of equations can be rewritten in matrix form as:

$$\begin{bmatrix} \dot{X}_1 \\ \dot{X}_2 \end{bmatrix} = \begin{bmatrix} 0 & 1 \\ K/M & C/M \end{bmatrix} \begin{bmatrix} X_1 \\ X_2 \end{bmatrix} + B \begin{bmatrix} \delta \\ w \\ F \end{bmatrix} \tag{2.14}$$

with $K = \begin{bmatrix} k_e + k & -k_e \\ -k_e & k_e \end{bmatrix}$ the stiffness matrix, $C \begin{bmatrix} c_e + c & -c_e \\ -c_e & c_e \end{bmatrix}$ the damping

matrix, $M = \begin{bmatrix} m & 0 \\ 0 & M \end{bmatrix}$ the mass matrix and $B = \begin{bmatrix} 0 & 0 & 0 \\ 0 & 0 & 0 \\ k & k & 0 \\ 0 & 0 & 1 \end{bmatrix}$ the matrix for all

the control and disturbance forces. This can simply be written as:

$$\dot{X} = AX + BU \tag{2.15}$$

and is called the input matrix of the system. The output of the system is given by:

$$Y = C_s X + DU. \tag{2.16}$$

Eq. (2.15) and (2.16) together are called the state space description of a linear set of equations. This is usually used for multiple input multiple output (MIMO) systems. Assuming zero initial conditions, the input equation for the system can be rewritten in the Laplace domain as:

$$X(s) = (sI - A)^{-1} BU(s), \tag{2.17}$$

with I an identity-matrix the same size as A. The output then becomes:

$$Y(s) = [C_s(sI - A)^{-1}B + D]U(s) = G(s)U(s). \tag{2.18}$$

Matrix $G(s)$ is called the transfer function matrix linking all control and disturbances (δ, w, F) to all outputs $(x_e, x, \dot{x}_e, \dot{x})$ for the open loop system.

Geophone position feedback

For the first control loop, a geophone is used to measure the velocity of the intermediate mass which is integrated to obtain the position. The geophone is modelled with a high pass filter at 0.7 Hz and a low pass filter at 50 Hz. Its sensitivity curve is combined in a transfer function $H(s)$ together with a lag and a lead to increase stability. The lag and lead are compensator filters, constructed from a pole and a zero which are given by:

$$H_l(s) = g_l \frac{Ts + 1}{\alpha Ts + 1}. \tag{2.19}$$

The variable g_l a gain and T is the period that defines the position of the compensator in the frequency domain. For $\alpha > 1$, a lag compensator is obtained as the pole will be located at a lower position than the zero creating a local phase decrease. If $\alpha < 1$ then the zero will be located before the pole and it is a lead, creating a local phase increase. The point of maximum phase change is located at $\omega_c = 1/(\sqrt{\alpha}T)$.

The expression for the piezo actuator elongation is then given by:

$$\delta = -H(s)x_e, \tag{2.20}$$

which can be used in the state space equations. If the actuator elongation is split off from the disturbances with $W_1 = \begin{bmatrix} w \\ F \end{bmatrix}$, then the input equation can be rewritten as [25]:

$$\dot{X} = AX - BB_gX + EW_1, \tag{2.21}$$

with

$$B_g = \begin{bmatrix} Z_{2\times2} & Z_{2\times2} \\ P & Z_{2\times2} \end{bmatrix}, \text{ and } P = \begin{bmatrix} -H(s) & 0 \\ 0 & 0 \end{bmatrix}. \tag{2.22}$$

In this equation, the $Z_{2\times2}$ variable is a two by two matrix filled with zeros. The closed loop system matrix is then given by $G_{cl} = A - BB_g$ and its eigenvalues are the closed loop poles. The closed loop transmissibility T_{wx} between the quadrupole position (x) and the ground motion (w) is shown in Fig. 2.11 (left panel) and the compliance T_{Fx} is shown in Fig. 2.11 (right panel). The root-locus for the system is shown in Fig. 2.12 (left panel) and the open loop Nichols plot

shows the phase margins in Fig. 2.12 (right panel). Conclusions will be drawn in the final part of this section by comparing the different strategies.

Capacitive gauge feedback

Instead of using a geophone on the intermediate mass, a capacitive sensor can be used to measure the distance between the intermediate mass and the payload mass. A model is shown in Fig. 2.2. The elongation of the piezo actuator is then given by:

$$\delta = -H(s)(x - x_e), \tag{2.23}$$

where $H(s)$ includes a gain, and a lead and a lag to increase the phase margins at the two cross-over points. This results in a minimum phase margin of 50 degrees as is shown in Fig. 2.13d. Matrix B_g then becomes:

$$B_g = H(s) \begin{bmatrix} Z_{2\times2} & Z_{2\times2} \\ P & Z_{2\times2} \end{bmatrix}, \text{ and } P = \begin{bmatrix} 1 & -1 \\ 0 & 0 \end{bmatrix} \tag{2.24}$$

The closed loop transmissibility T_{wx} and compliance T_{Fx} are shown in Fig. 2.11 (left panel) and (right panel), respectively in order to compare performances with the geophone control loop. The root-locus showing unconditional stability is presented in Fig. 2.13 (left panel).

Results and conclusions

A comparison is made in terms of stabilisation performance in Fig. 2.11 (left panel) and compliance in Fig. 2.11 (right panel).
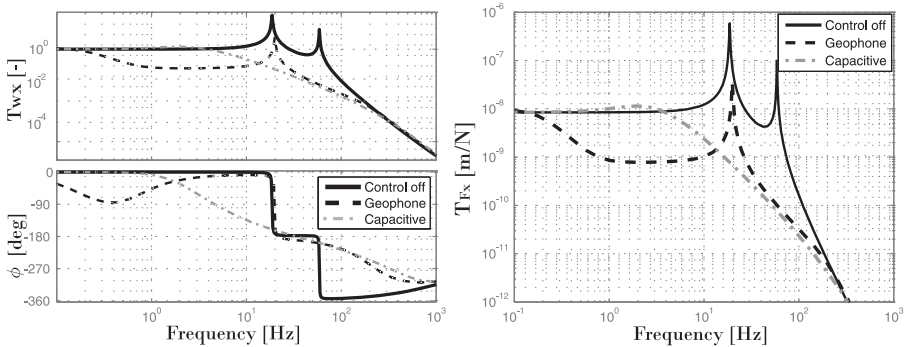
Figure 2.11: *The closed loop transmissibility T_{wx} (left panel) and compliance T_{Fx} (right panel) for a stiff actuator with intermediate mass and elastomer using a geophone or a capacitive gauge as a sensor.*

Using a geophone with a cut off frequency as low as 0.7 Hz allows for a better stabilisation performance at low frequencies. However, since the geophone

is located on the intermediate mass, it has hardly any effect on the first mode, due to the elastomer and the payload, as this mode is not observable to the geophone. The second mode caused by the stiff piezo actuator is damped by a local velocity feedback as a result from the lead compensator used. Using a relative measurement between the two masses allows to measure and consequently damp both modes.

Both approaches are infinitely stable as is shown by their rootlocus shown in Figs. 2.12 and 2.13.
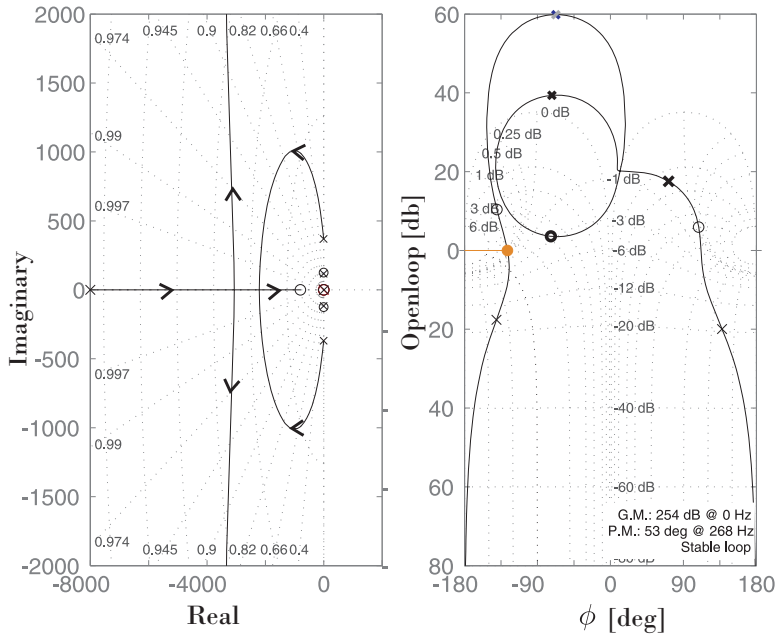
Figure 2.12: *The root-locus (left panel) and the Nichols graph (right panel) for a system composed of a stiff piezo actuator with an elastomer in series; a geophone is used as feedback sensor.*

The robustness of the system towards unpredicted changes in the controller due to delay, sensor tolerances, ... is given by the phase margin of the system. From the root-locus it can be derived that for the point of neutral stability, where the system transfers between stable and unstable and poles cross from the left half plane to the right, the following must hold [26]:

$$|H(s)G(s)| = 1, \phi(s) = 180^o \qquad (2.25)$$

for the first neutral point and

$$|H(s)G(s)| = 1, \phi(s) = -180^o \qquad (2.26)$$

for the second. The smallest margin between the system phase and these phase limits at the two cross-over points is the minimum phase margin. The Nichols diagrams shown in Fig. 2.12 and 2.13 show the minimum phase margin for both approaches is around 50 degrees. A comparison will be performed at the end of this section between the different vibration isolation systems investigated.
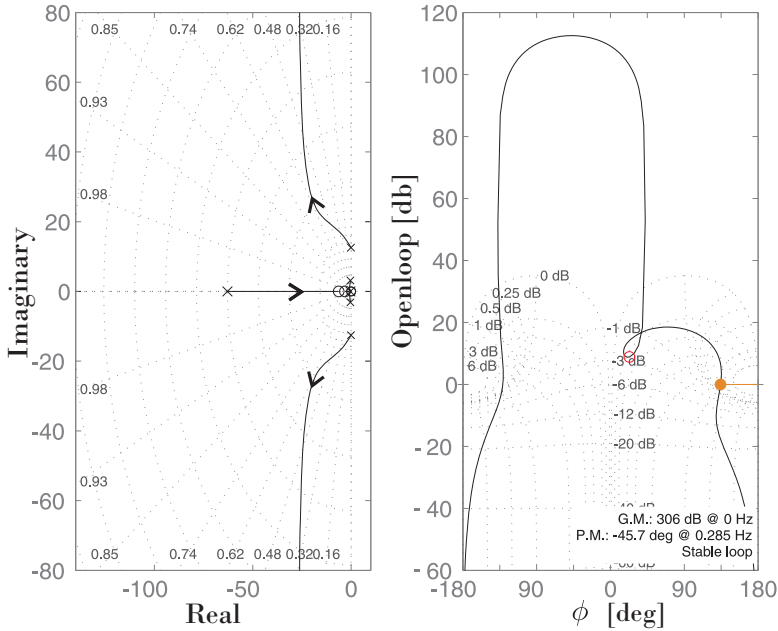
Figure 2.13: *The root-locus (left panel) and the Nichols graph (right panel) for a system composed of a of a stiff piezo actuator with an elastomer in series; a capacitive gauge between the payload mass and the intermediate mass is used as feedback sensor.*

2.4.2   Reference mass as a sensor

In this subsection, the importance of the position of the vibration sensor is investigated. Most vibration sensors are based on a soft reference mass to which the payload position is compared. In this sub-section, the difference between a reference mass on the ground and on top is investigated.

A. Reference mass on the ground with soft actuator

The Advanced Isolation modules (AIMS) table, which is described in Refs. [21, 22, 23, 24], uses a reference mass on the ground. The aim is to increase the compliance down to 0 Hz as the reference mass is not influenced by the disturbance force F. The AIMS table uses an electromagnetic actuator to get a low natural frequency

for the payload mass. A capacitive gauge is used to measure the distance between the payload and the reference mass, which itself has a Sky-hook controller to reduce the resonance peak of the reference spring mass system.

Fig. 2.14 shows a schematic of the AIMS isolation system.
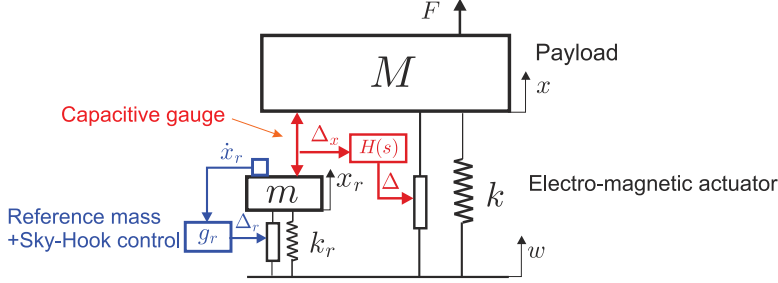
Figure 2.14: *Schematic of the AIMS isolation system.*

The equations of motion of the masses are given by:

$$m\ddot{x}_r + k_r(x_r - w - \delta_r) = 0,$$
$$M\ddot{x} + c(\dot{x} - \dot{w}) + k(x - w - \delta) = F. \tag{2.27}$$

A so-called sky-hook system is used for the reference mass, with:

$$\Delta_r = g_r s X_r(s). \tag{2.28}$$

The reference mass m is suspended with a stiffness k_r in order to obtain a natural frequency of 0.5 Hz. The gain g_r is chosen so the reference mass is critically damped. The stiffness k of the payload system is chosen so the natural frequency of the payload mass is 2 Hz. A modal damping of 1% was added to the system. The elongation of the electro-magnetic actuator is given by:

$$\Delta(s) = H(s)\Delta_x = H(s)(X(s) - X_r(s)). \tag{2.29}$$

A Proportional Integral Derivative (PID) compensator is used which is described by Ref.[25]. We have:

$$H(s) = -(g/s)(s + 1/T_I)(T_D s + 1), \tag{2.30}$$

with relation between the pole and zero given by:

$$\frac{b}{T_I} \sim \frac{1}{T_D}. \tag{2.31}$$

The factor b depends on the bandwidth needed for the proportional control. An example of a PID compensator is shown in Fig. 2.15.
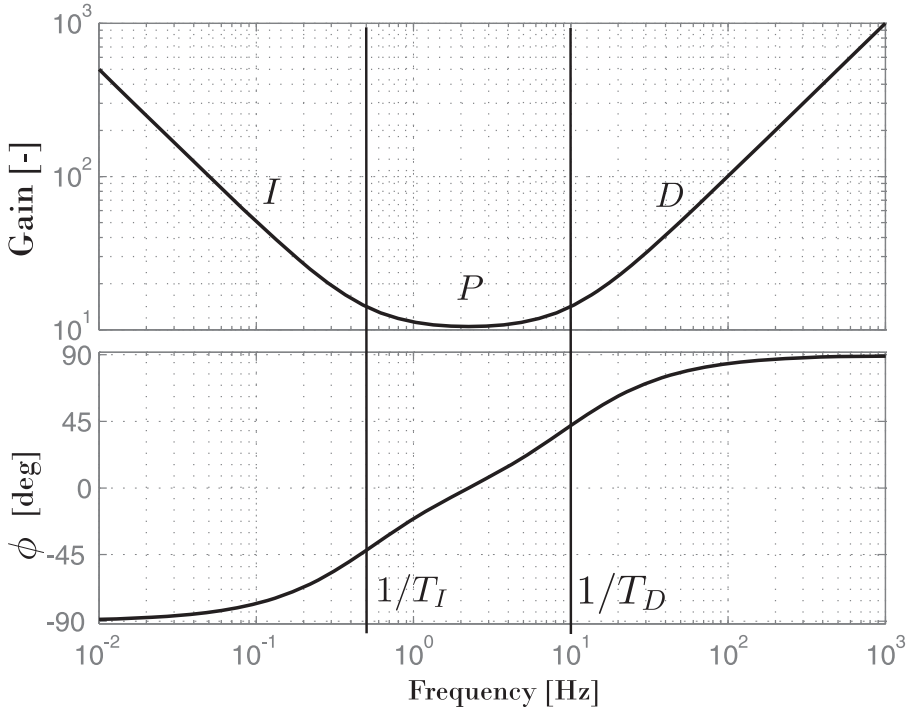
Figure 2.15: *An example of a PID compensator.*

The integrator below $f_i = 1/(T_I)$ ensures the elimination of drift while the differentiator above $f_d = 1/(T_D)$ increases stability by improving the phase margin by +90 degrees. The closed loop transmissibility T_{wx} and compliance T_{Fx} are shown in Fig. 2.17 (left panel) and (right panel) respectively.

B. Reference mass system on the payload with soft actuator

An active vibration isolation system with reference mass placed on top of the payload has been described by different authors [[18], [27],[28],[23]]. It consists of a payload mass with a reference mass on top. The displacement between the payload mass and the reference mass is measured with a capacitive sensor. Alternatively, a coil with a magnet can be used to measure the velocity after which it is integrated to obtain the displacement. This is the working principle of a geophone as will be explained in section 2.6. A schematic of the system with a reference mass on the payload, using a capacitive gauge to measure Δx, is shown in Fig. 2.16.
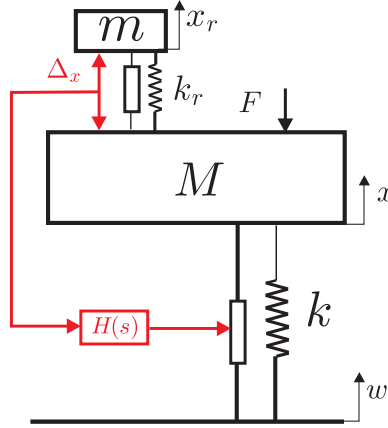
Figure 2.16: *Schematic view of a vibration isolation system with a reference mass m, using a capacitive gauge, on top of the payload with mass M.*

The equations of motion are given by:

$$m\ddot{x}_r + k_r(x_r - x) = 0,$$
$$M\ddot{x} + k(x - w - \delta) + k_r(x - x_r) = F, \tag{2.32}$$

and the elongation of the actuator is given in the Laplace domain by:

$$\Delta(s) = -H(s)(x_r - x) = -\overbrace{\frac{\omega_{clp}^2}{s^2 + \sqrt{2}\omega_{clp}s + \omega_{clp}^2}}^{low-pass\,filter} \overbrace{\frac{T_{lead}s + 1}{\alpha_{lead}T_{lead}s + 1}}^{lead}$$

$$\overbrace{\frac{T_{lag}s + 1}{\alpha_{lag}T_{lag}s + 1}}^{lag}(x_r - x) \tag{2.33}$$

The controller $H(s)$ consists of a low pass second order Butterworth filter, limiting the sensitivity curve of the relative measurement between x_r and x, and a lag-lead filter to increase stability. The closed loop transmissibility T_{wx} and compliance T_{Fx} are shown in Fig. 2.17 (left panel) and (right panel) respectively.

Results and conclusions

Fig. 2.17 (left panel) shows the performance in terms of isolation capability and Fig. 2.17 (right panel) the compliance for both strategies. The reference mass on top allows better vibration isolation performance around the resonance of the reference mass at 0.5 Hz. Placing the reference mass on the ground and measuring displacements relative to the payload eliminates the sensitivity of the reference

mass to the external force F. Therefore this configuration reduces the compliance down to 0 Hz, this is even increased by the integrator of the PID controller.
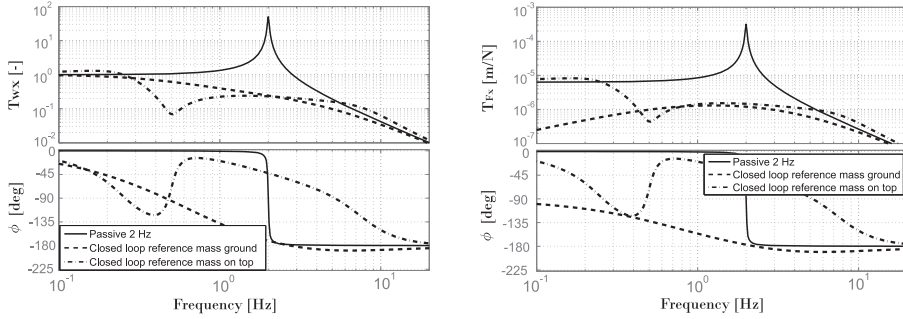
Figure 2.17: *The closed loop transmissibility T_{wx} (left panel) and compliance T_{Fx} (right panel) for the different systems found in the literature.*

Both approaches are infinitely stable as is shown by their root-locus displayed in Figs. 2.18 and 2.19 . The Nichols diagrams shown in Figs. 2.18 and 2.19 show that the phase margin for both approaches is around 32 and 45 degrees for a system with mass m on the ground and on top of the payload, respectively.
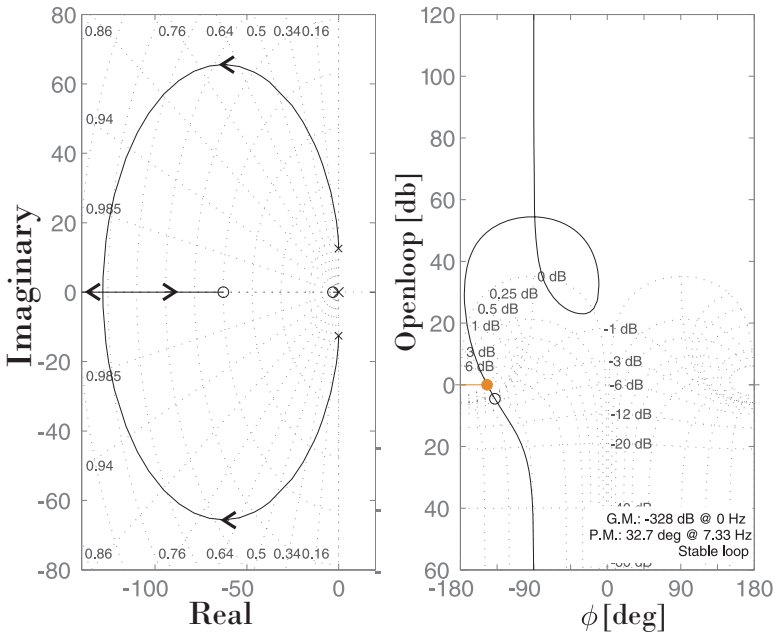
Figure 2.18: *The root-locus (left panel) and the Nichols graph (right panel) for a system composed of a soft actuator and a reference mass on the ground.*
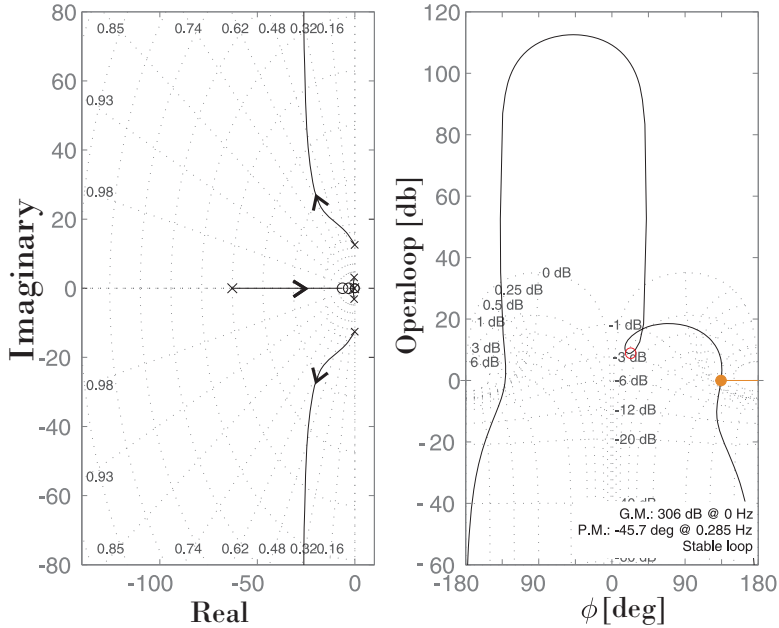
Figure 2.19: *The root-locus (left panel) and the Nichols graph (right panel) for a system composed of a soft actuator and a reference mass placed on top of the payload.*

2.4.3 State of the art in Vibration isolation for accelerators

Two Ph.D. researchers have pioneered the vibration isolation possibilities for linear accelerators. The first one was C. Montag in 1996 (see Ref. [29]). He used a piezo actuator and a KEBE geophone on a magnet with one leg. Vibrations were reduced from 100 nm to 26 nm integrated RMS at 2 Hz [29] and from 40 nm to 10 nm integrated RMS at 4 Hz [1]. It was also suggested that the effect of the water cooling was minimal due to the stiff support. Although the values are a factor 10 higher than required, this approach is promising for both disturbance rejection from water cooling and isolation from ground vibrations.

The second pioneer was S. Redaelli (see Ref. [1]). He used an adapted TMC table using high performance seismometers to perform vibration isolation. This resulted in a vibration reduction to 0.43 nm from 6 nm integrated RMS at 4 Hz. Performance drops off near 1 Hz to almost a transfer of 1 between the ground and the magnet. Concerns were raised about the alignment capability of the system due to its relative softness. This research was continued by B. Bolzon [30] where a STACIS table was used to perform vibration isolation of a magnet, similar to efforts done by G.M. Bowden at Stanford Linear accelerator Laboratory (SLAC)

[31]. The research at SLAC has since been continued with custom made solutions as shown in Ref. [32], [33].

Vibration isolation for cryogenic accelerators is also being performed with interesting methods shown in Ref. [34] and [35].

Very soft suspension isolation systems have also been designed [36]. These are not further discussed due to their inherent sensitivity to external forces.

2.4.4   Summary

The literature review of systems with a position feedback has shown that such systems can perform satisfactory in terms of vibration isolation but are well below the requirement in terms of compliance as most systems move several μm for a force as low as 1 N. The system proposed by TMC is the most promising in terms of performance for both isolation and compliance. Ideally there would be no elastomer as it is not compatible with the accelerator environment. Therefore a more comprehensive investigation is carried out of a system that solely uses a piezo actuator and a vibration sensor partly based on Ref. [29]. In the next two sections the basics of piezo actuators and vibrations sensors are discussed.

2.5   Piezo actuator basics

The working principle of the piezo actuator was discovered by Pierre and Jacques Curie [37]. They found that certain crystalline materials generate an electrical charge that is directly proportional to an applied force which changes the length of the test block. Inversely, when an electrical field is applied, the material changes size.

Some of the most known piezo-electric materials are Lead-Zirconate-Titanate (PZT) and Polyvinylidene fluoride. These materials react in the following way to external influences [37]:

$$\begin{aligned} D &= \varepsilon^T E + d_{33} T, \\ S &= d_{33} E + s^E T. \end{aligned} \tag{2.34}$$

In these equations, D responds to the electric displacement (Coulomb/m), E the electrical field (V/m), T the stress (N/m^2) and S the strain. The variable ε^T responds to the dielectric constant or permittivity under constant stress. This is a property of the material. The compliance or inverse of the Young's modulus is defined by s^E, while d_{33} is the piezo electric constant (m/V). By convention the subscript 33 always denotes the direction of the polarization of the crystal. By integrating Eq. (2.34) over the transducer for n layers and an area A it can be shown that:

$$\begin{bmatrix} Q \\ \Delta \end{bmatrix} = \begin{bmatrix} C & nd_{33} \\ nd_{33} & 1/k_a \end{bmatrix} \begin{bmatrix} V \\ f \end{bmatrix},$$ (2.35)

where $Q = nAD$ is the total charge on the electrodes, Δ the total change in length, $f = AT$ the total force and V the applied voltage between the electrodes resulting in an electric field of $E = nV/l$ with l the total length of the actuator. The capacitance without an external load is defined as $C = \varepsilon^T An^2/l$. The stiffness without any applied voltage is described by k_a. These equations assume that the accuracy and precision of the extension of the piezo purely depends on the ability to apply a certain voltage (or current). A schematic representation of a multi layer piezo actuator is shown in Fig. 2.20a.
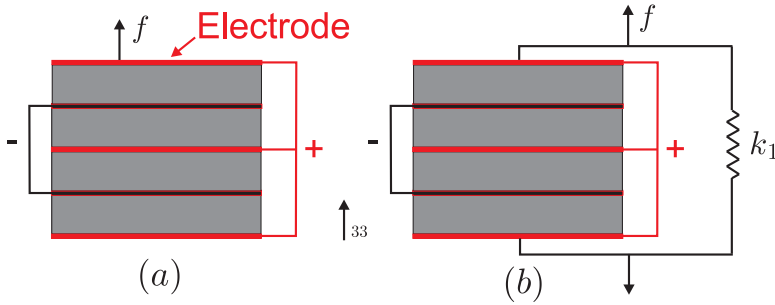
Figure 2.20: *A schematic representation of a $n = 4$ layer piezo actuator (a); Schematic representation of a $n = 4$ layer piezo actuator with pre-stressing spring (b) (adapted from Ref. [37]).*

As piezo actuators are often ceramic crystals, they are much more fragile under tension and moment forces than under compression forces. Therefore often a pre-stress spring is added. A schematic representation of such an actuator is given in Fig. 2.20b. The state equations are then given by:

$$\begin{bmatrix} Q \\ \Delta \end{bmatrix} = \begin{bmatrix} C & nd_{33} \\ nd_{33} & 1/(k_a + k_1) \end{bmatrix} \begin{bmatrix} V \\ f \end{bmatrix},$$ (2.36)

where k_1 represents the stiffness of the pre-stressing spring. A piezo actuator is basically a capacitor and its capacitance between the output terminal of an operational-amplifier and ground forms a first order lag filter [38] as was described in section 2.4.1, see Fig. 2.21.
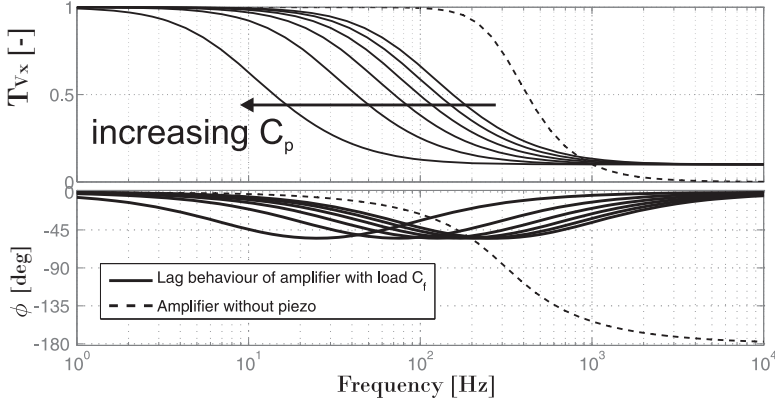
Figure 2.21: *The lag behaviour of an amplifier with infinite slew rate connected to a piezo actuator with capacitance C_p (solid) and the output of an amplifier with a frequency compensating capacitance C_f (dashed) (adapted from Ref. [38]).*

Below this limit, the performance of a well designed and produced piezo actuator mainly depends on the amplifier which supplies the voltage (or charge). A simple amplifier configuration is shown in Fig. 2.22.
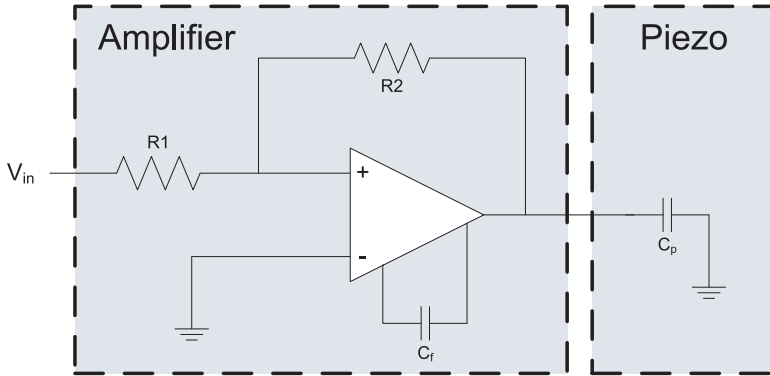
Figure 2.22: *Schematic of a simple amplifier to control a piezo actuator. (adapted from Ref. [38]).*

One of the bandwidth limitations due to the amplifier is called the slew rate. This is the maximum rate at which the output voltage can change for an amplifier when supplying large signal swings and is usually expressed in $\mu s/V$ [38]. The slew rate can be approximated by the ratio of the input current of the first gain stage of the amplifier (I_0) and the frequency compensating capacitance C_f [38]:

$$\text{Slew rate} \simeq \frac{I_0}{C_f}. \tag{2.37}$$

A potential risk exists that combining both the phase drop due to the low pass behaviour and the lag results in a phase drop of more than 180 degrees in the feedback loop. Therefore, these have to be separated and they should be added to the total model of the vibration isolation system in order to simulate the phase drop of the complete system.

2.6 Vibration sensor basics

This section is adapted from Ref. [39] and will give an overview of the working principle of several vibration sensors, special attention is paid to the noise levels and sensor bandwidths.

2.6.1 Sensor Definitions

The **sensitivity** S of a sensor is defined as the factor between the physical quantity U which is the subject of the measurement and the output voltage V_0 of the sensor:

$$S = \frac{V_0}{U}.$$ (2.38)

The **noise** N of the sensor is defined as the part of V_0 that does not correspond to U.

The **resolution** R of a sensor is the smallest quantity that a sensor is able to measure. It is given by:

$$R = \frac{N}{S}.$$ (2.39)

The **dynamic range** DR of a sensor is the ratio between the maximum output voltage V_0^{max} and the minimum output which corresponds to the root mean square (RMS) of the noise N_{RMS} or:

$$DR = \frac{V_0^{max}}{N_{RMS}},$$ (2.40)

or by eliminating the sensitivity from both numerator and denominator:

$$DR = \frac{U_{max}}{R_{RMS}},$$ (2.41)

where U_{max} is the maximum measurable physical quantity. In order to have a good sensor, S and DR have to be large and R and N have to be small.

2.6.2 Absolute vibration measurement

An absolute measurement of a quantity (displacement, velocity or acceleration) is a measurement with respect to the inertial reference frame. Inertial sensors,

as shown in Fig. 2.23, are capable of measuring those absolute quantities in a limited frequency range. An inertial sensor consists of a mass m connected to the degree of freedom that needs to be measured through a spring with stiffness k and a dashpot with damping constant c.
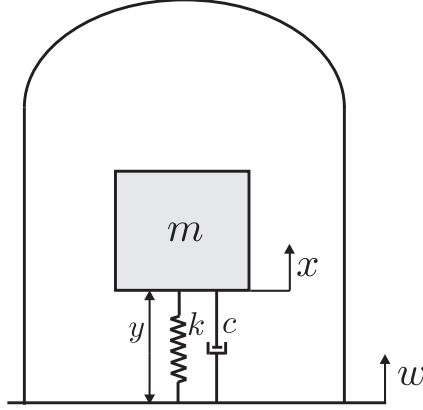
Figure 2.23: *Working principle of an inertial sensor.*

The equation of motion of the sensor is given by:

$$m\ddot{x} + c(\dot{x} - \dot{w}) + k(x - w) = 0. \tag{2.42}$$

The actual output voltage of the sensor is given by the relative measurement y between the mass position x and the ground w. Rewriting the equation of motion in function of y and applying the Laplace transform gives:

$$ms^2Y + csY + kY = -ms^2W \tag{2.43}$$

From Eq. (2.43), the transmissibility $T_{wy}(s)$ between the displacement of the attachment point $W(s)$ and the relative displacement $Y(s)$ is given by:

$$T_{wy}(s) = \frac{Y(s)}{W(s)} = \frac{-ms^2}{ms^2 + cs + k} \tag{2.44}$$

This transfer function (obtained for $s = j\omega$) is shown in Fig. 2.24 (dotted curve).

Above the resonance frequency of the oscillator $\omega_0 = \sqrt{k/m}$, the measurement of the relative displacement $Y(s)$ is an estimator of the absolute displacement $W(s)$, because of the flat transfer function (dotted curve). Similarly if the relative velocity $\dot{Y}(s) = sY(s)$ is used, it is an estimator of the speed $\dot{W}(s)$ above ω_0 (dashed curve). This is the working principle of a geophone. Fig. 2.24 also shows the transmissibility $T_{\ddot{w}y}$ between the acceleration $\ddot{W}(s) = s^2W(s)$ and $Y(s)$. Following the same reasoning, below ω_0, $Y(s)$ is a perfect estimator of the
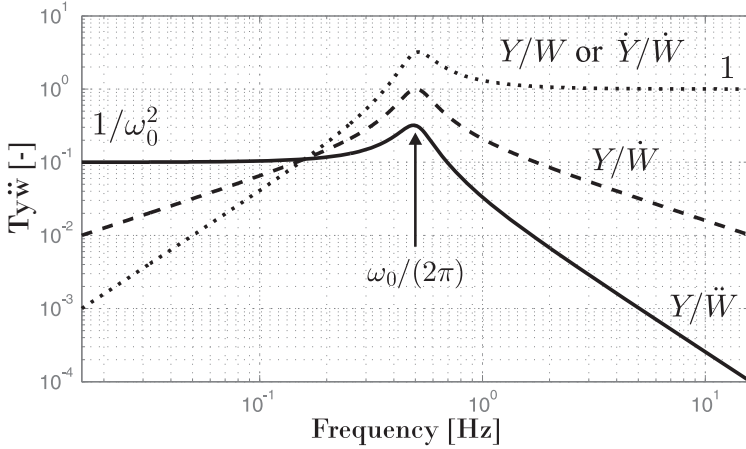
Figure 2.24: *Transmissibilities of the sensor described in Fig. 2.23 for $\omega_0 = 2\pi 0.5$ rad/s.*

acceleration $\ddot{W}(s)$ (solid curve). This is the working principle of accelerometers. However, it has to be noted that the amplitude of the transmitted motion is scaled by $1/\omega_0^2$. In other words, the sensitivity of the accelerometer is increased when ω_0 is decreased.

Given the above discussed alternatives, now it is a question of how to measure $Y(s)$ the best.

Geophone

The principle of a geophone is explained in Fig. 2.25 [40]. The seismic mass m is moving in a coil with n turns and radius r. The coil is loaded by resistance R.

The ground w generates a relative motion $w - x$ between m and the coil. The relative motion creates a current i which flows through the load resistance R_l and the coil resistance R_c. These are combined in $R = R_l + R_c$ for the following calculations. The equations of the system are:

$$m\ddot{x} + c(\dot{x} - \dot{w}) + k(x - w) + Ti = 0 \tag{2.45}$$

for the mechanical part and

$$L\dot{i} - T(\dot{x} - \dot{w}) + Ri = 0 \tag{2.46}$$

for the electrical part. Variable i represents the current, L is the inductance of the coil and $T = 2\pi nrB$ is the constant of the coil, expressed in Tm or V/(m/s). Defining $y = x - w$ and performing a transformation to the Laplace domain results in:

$$ms^2Y + csY + kY + TI = -ms^2W, \tag{2.47}$$
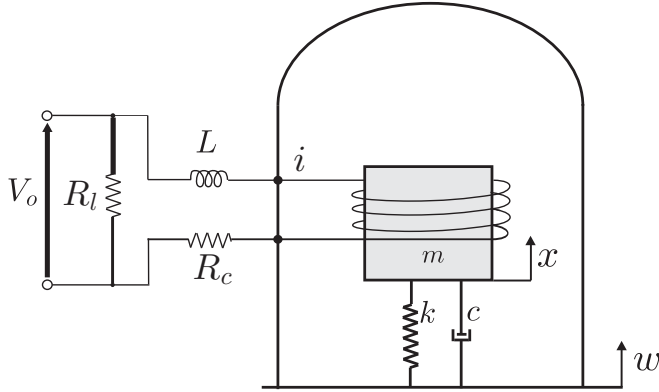
Figure 2.25: *Schematic of the working principle of a geophone.*

$$LsI - TsY + RI = 0. \tag{2.48}$$

The output of the sensor is the voltage V_0 across the resistance R, $V_0 = RI$. Then we find:

$$\frac{V_0}{sW} = \frac{RT}{Ls + R} \frac{-ms^2}{ms^2 + sc + k + \frac{T^2 s}{Ls+R}}. \tag{2.49}$$

If R is large, Eq. (2.49) is reduced to:

$$\frac{V_o}{sW} = \frac{-mTs^2}{ms^2 + sc + k} = \frac{-Ts^2}{s^2 + 2\xi_g\omega_g s + \omega_g^2} \tag{2.50}$$

which is the typical expression of a high pass filter. Actually, a geophone can measure the velocity of the support, typically from a few Hertz to a few hundred Hertz. At high frequency, the performance is limited by the higher order modes of the mechanical system, called spurious resonances. At low frequency, the performance is limited by the fundamental resonance of the inertial mass.

To some extent, the corner frequency can be decreased, either passively by adding a capacitor in series with the resistance [41], or actively by dividing the coil in two parts, and by using the signal from one part to control the other one with a PI controller [37]. The properties of a few commercial geophones are compared in Table 2.1.

2.6.3   Seismometer

For even lower frequencies, Force Balanced Accelerometers (FBA) are used, or broad band seismometers.

For a seismometer, as for a geophone, a mass is mounted on a compliant element, represented in Fig. 2.26 by k and c.

Type	Refs.	Range [Hz]	Freq. res. [Hz]	Sensit. [V/(m/s)]	Susp. mass [g]	Size [mm]
GS1	[42][43]	1-∞	1	40	700	160x75
GS11D	[42][44]	4,5-∞	4.5	23	23	33.5x31.8
JF-20DX	[45]	8	10	28	11	25x34
L4C	[42][46]	1-∞	1	276	1000	76x130
SM-4 UB8	[47]	8-160	8	28.8	11	25.4x32
SM-6(UB 8)	[48]	8-150	8	28.8	11.1	25.4x36

Table 2.1: *Characteristics of commercial geophones.*
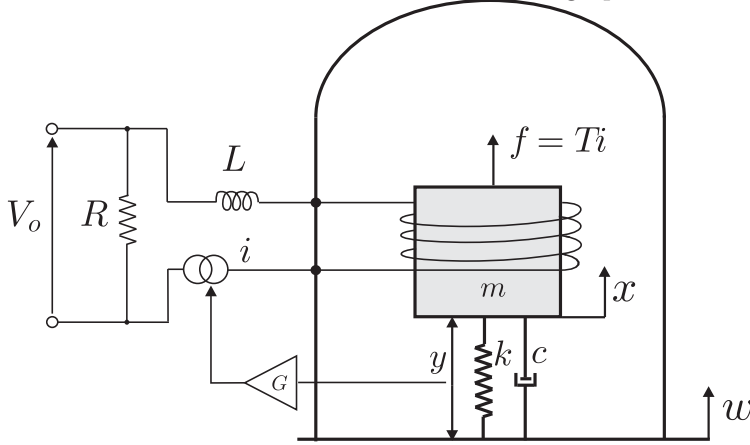
Figure 2.26: *Working principle of a broadband seismometer.*

The relative displacement $y = x - w$ is measured by a relative displacement sensor with sensitivity $G(s)$. The output voltage is then given by:

$$V_0(s) = G(s)Y(s). \tag{2.51}$$

The output signal is used through a compensator $H(s)$ to generate a current

$$I(s) = H(s)V_0(s) = H(s)G(s)Y(s), \tag{2.52}$$

which is sent into the coil of the seismometer creating a force given by:

$$f(s) = -TI(s) = -TH(s)G(s)Y(s), \tag{2.53}$$

with T again the coil constant. This force is trying to compensate the movement of the seismic mass. It is known as the *Force Balancing principle*. When this force is added to the equations of motion, the new transfer function between the output voltage V_0 and the ground w is given by:

$$\frac{V_0}{W} = \frac{-ms^2}{(ms^2 + cs + k)/G(s) + TH(s)}. \tag{2.54}$$

For a broad band seismometer the controller will consist of a Proportional Integral Derivative (PID) controller:

$$H(s) = g_p + \frac{g_i}{s} + sg_d. \tag{2.55}$$

The proportional gain g_p ensures a stronger force generated by the coil. Additionally, as seen in the beginning of this section, a proportional feedback adds virtual stiffness to the system which increases the natural frequency from $\omega_0 = \sqrt{\frac{k}{m}}$ to $\omega_0 = \sqrt{\frac{k+GTg_p}{m}}$. In this way, the bandwidth is extended. In the useful bandwidth the sensitivity is however reduced to:

$$\frac{V_0}{W} = \frac{ms^2}{Tg_p}. \tag{2.56}$$

The integral gain removes the drift at low frequencies and the derivative gain damps the resonance of the system. The derivative gain g_d is used to add virtual mass to the system, lowering the natural frequency of the system and extending the bandwidth. This changes the sensitivity in the useful bandwidth (if $g_i \ll g_d$) to:

$$\frac{V_0}{sW} = \frac{m}{Tg_d}. \tag{2.57}$$

The effect of the different gains on the sensitivity function of a seismometer with a velocity measurement is shown in Fig. 2.27. A capacitive gauge with
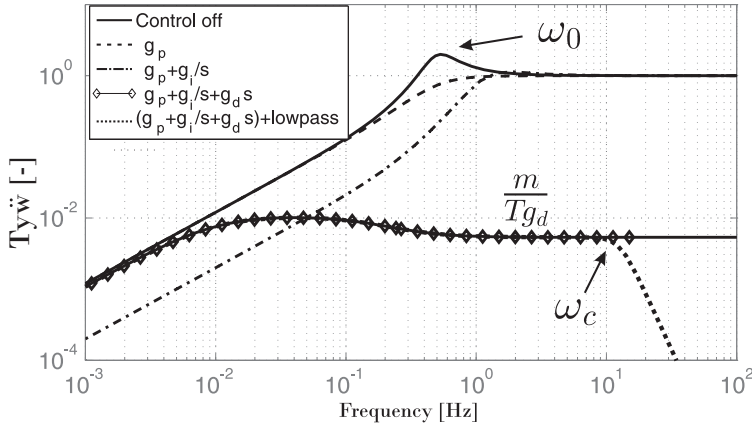
Figure 2.27: *The effect of the different gains on the sensitivity function of a seismometer.*

integrated feedback can be added in order to eliminate drift at low frequencies. Some seismometers are limited at higher frequencies by low pass filters with cut

off frequencies ω_c (see Fig. 2.27) in order to remove spurious frequencies and to reduce noise at higher frequencies. The sources of this sensor noise are discussed in the next section.

Type	Refs.	Range [Hz]	Nat. freq. [Hz]	Sensit. [V/(m/s)]	Total sensor mass [kg]	Size [mm]
STS-2	[49]	0.008-50	0.0083	1500		230×235
MET4111	[44]	0.016-50	0.016	4000	5,1	140 ×180
CMG-3ESP	[50]	0.03-500	0.03	1000	8	168×258
CMG-6T	[50]	0.03-100	0.03	2000	2.5	154×205
SP500	[51]	0.016-75		2000	0.75	50×100×150

Table 2.2: *Characteristics of commercial seismometers.*

2.6.4   Sensor noise

Ground motion sensors are all based on the measurement of the relative motion of a proof mass with respect to the ground. In such sensors, there basically exist four different sources of noise [29, 52, 53, 54]:

- **Thermo-mechanical noise** or *Brownian noise* of the mechanical system, arises from the Brownian motion of the proof mass [55]. The power spectral density of the mass acceleration above the resonance is:

$$\Phi_B(f) = 16\pi k_B T \frac{\xi f_0}{M} \ [(\text{m/s}^2)^2/\text{Hz}], \qquad (2.58)$$

  where k_B is the Boltzmann's constant, T the temperature, f_0 the resonance frequency of the oscillator, ξ is the percentage of critical damping, and M is the suspended mass. This contribution becomes larger with a decreasing size of the proof-mass.

- **Thermo-electrical noise**, or *Johnson noise*, is generated in the resistive components of the sensor circuit due to random thermal excitation of the charge carriers, generating a white noise voltage of:

$$\Phi_J(f) = 4k_B T R \ [\text{V}^2/\text{Hz}], \qquad (2.59)$$

  where R is the resistance of the component. Typically, it corresponds to an RMS value expressed in V above one Hertz. The dielectric loss in a capacitor C can be modelled by placing a resistance R_C in parallel with the capacitor [56]. The equivalent resistor is:

$$R_C = \frac{1}{\eta \omega C}, \qquad (2.60)$$

  where η is the loss factor of the capacitor.

- **Shot noise** or *Schottky noise* is caused by random movement of electric
  charges across potential barriers, such as p-n junctions [54]. Its power spec-
  tral density $\Phi_{sh}(f)$ can be modelled by:

$$\Phi_{sh}(f) = 2qI_{dc} \ [\text{A}^2/\text{Hz}], \tag{2.61}$$

where I_{dc} is the average current that crosses the barrier. It has the shape
of a white noise current.

- **Flicker noise** or *1/f noise* is mainly due to impurities in the production
  of semiconductor devices. Its main characteristic is that its power spectral
  density is inversely proportional to the frequency, and can be modelled by:

$$\Phi_V(f) = K/f^\alpha \ [\text{V}^{\,2}/\text{Hz}], \tag{2.62}$$

where the exponent is usually $\alpha = 1$. Typical values for sensor amplifier's
noise constants can be found in Ref. [56].

The next section provides a tool to evaluate the magnitude of the overall noise
arising from a set of sensors.

2.6.5   Detection

A computation of the spectral noise of many seismometers can be found in Refs.
[57, 58, 29]. Let us call U the quantity to measure (see Fig. 2.28 a). Place two
sensors of the same type side-by-side, with transfer functions H_1 and H_2 between
the input and the output signals.
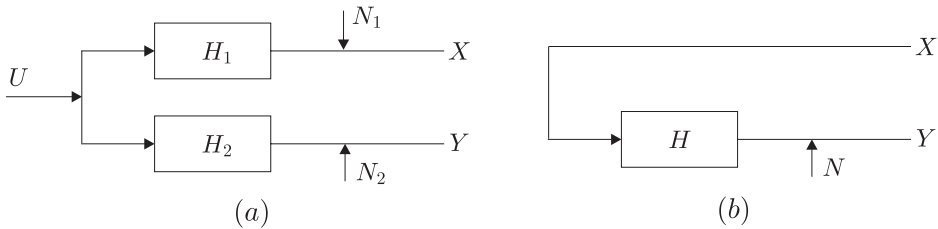
Figure 2.28: *Two sensors measuring the same input vibration [57, 29, 59].*

Assuming that N_1 and N_2 represent the noise of the two sensors, the output
signals in the frequency domain are given by:

$$X(\omega) = H_1(\omega)U(\omega) + N_1(\omega),$$
$$Y(\omega) = H_2(\omega)U(\omega) + N_2(\omega). \tag{2.63}$$

The coherence between the two signals is given by:

$$\gamma(\omega) = \frac{\Phi_{xy}(\omega)}{\sqrt{\Phi_{xx}(\omega)\Phi_{yy}(\omega)}}, \tag{2.64}$$

where $\Phi_{xy}(\omega)$ is the cross-power spectrum and Φ_{xx} and Φ_{yy} the power spectral densities. Solving the first equation in Eq.(2.63) for $U(\omega)$ and inserting the solution into the second gives:

$$Y(\omega) = H(\omega)X(\omega) + N(\omega), \tag{2.65}$$

where $H(\omega) = H_2(\omega)/H_1(\omega)$ and $N(\omega) = N_2(\omega) - H(\omega)N_1(\omega)$. The corresponding scheme is given in Fig. 2.28b, and

$$H(\omega) = \frac{\Phi_{xy}}{\Phi_{xx}}. \tag{2.66}$$

From Eq.(2.65), we find an estimated signal given by:

$$\Phi_{ss} = H^2\Phi_{xx} = \Phi_{xx}\gamma^2(\omega). \tag{2.67}$$

The PSD of the noise can then be calculated through subtracting the coherent signal part:

$$\Phi_{nn} = \Phi_{yy} - \gamma^2\Phi_{xx}. \tag{2.68}$$

By dividing the estimated signal Φ_{yy} through the PSD of the noise Φ_{nn}, the signal to noise ratio is calculated:

$$\beta(\omega) = \frac{\Phi_{ss}}{\Phi_{nn}} = \frac{\Phi_{xx}H^2}{\Phi_{nn}} = \frac{\gamma^2}{1-\gamma^2}. \tag{2.69}$$

The RMS value of the noise and signal are given respectively by:

$$\sigma_n(\omega) = [\int_\omega^\infty \Phi_{nn}(\nu)d\nu]^{1/2} \tag{2.70}$$

and

$$\sigma_s(\omega) = [\int_\omega^\infty \Phi_{ss}(\nu)d\nu]^{1/2}. \tag{2.71}$$

These last two equations provide a tool to evaluate the capacity of a sensor to detect a signal $u(t)$ in the frequency range of interest.

Fig. 2.29 compares the noise floor of several commercial inertial sensors, geophone L4C [46], seismometer CMG 6T [50] and a Wilcoxon 731A accelerometer. Additionaly, it includes the noise curves of possible relative displacement sensors which could be used to make a new vibration sensor: a PI capacitive sensor [60], an interferometric sensor [61, 62]. At low frequency, the sensor noise is dominated by the $1/f$ noise, inherent to the electronic circuitry. Around 1 Hz, a
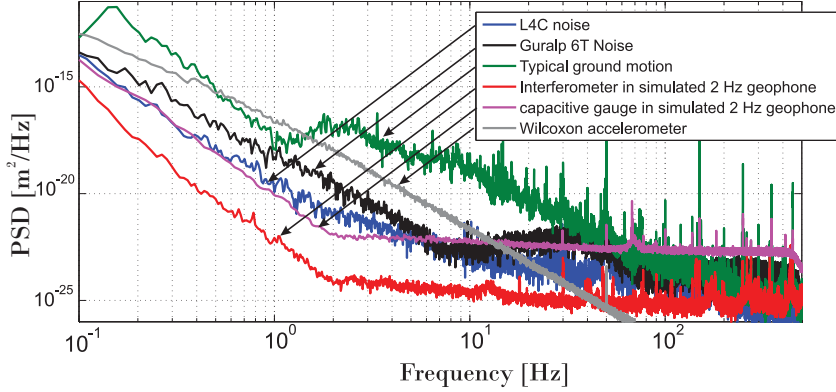
Figure 2.29: *Comparison of sensor noise floor.*

theoretical vibration sensor, using this particular capacitive sensor, would have a resolution 10 times better than the existing sensors. The interferometric sensor further improves the resolution by a factor 10. For signals above 50 Hz, the accelerometer is the preferred choice. In our application, most of the vibrations have frequencies below 50 Hz, therefore an accelerometer will not be practical for our application. The design of a new sensor is foreseen as a future project and for now the seismometer and L4C geophone will be used in further tests.

An interferometer would be the ideal choice but is expensive for these levels of noise (50 kChf) and thus not practical for a series of 4000 magnets. Both the seismometer and the geophone have an RMS noise level of around 0.2 nm at 1 Hz and would be practical sensors. In the next chapter the possibilities of implementing these sensors is investigated.

Chapter 3

Simplified modelling

The vibration isolation system for the different types of quadrupole magnets will not be positioned on the ground but on an alignment system as is shown in Fig. 3.1. Further, additional resonances can be caused by the length of the quadrupole and the connected vacuum tube.
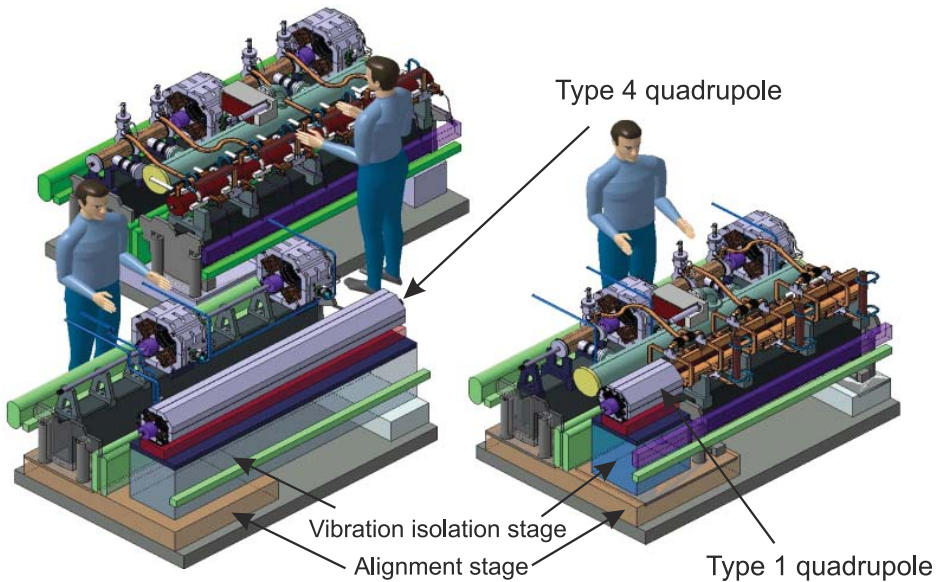
Figure 3.1: *Computer aided design model of three types of main beam accelerating modules. A fully accelerating structure on the top, a module including a Type 4 quadrupole on the bottom left and a Type 1 quadrupole on the bottom right (adapted from Ref. [5]).*

In order to understand the full effect of all the complexities of the vibration isolation and positioning system, the system is built up in steps from a single

degree of freedom to multiple degree of freedom. All the cases reviewed are shown in Fig. 3.2
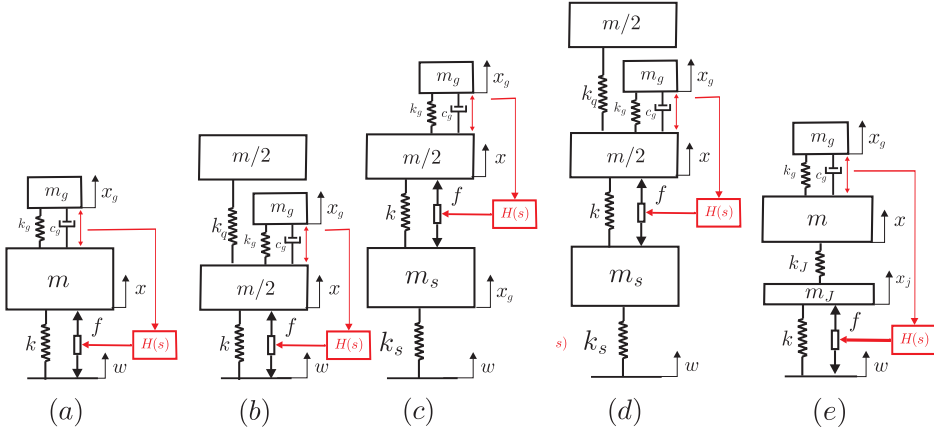
Figure 3.2: *Model of a single degree of freedom isolator with a reference mass (a), with a flexible appendage (b), with the alignment system (c), with both the alignment system and the flexible appendage (d), and with a flexible joint (e).*

3.1   Controller design for single degree of freedom

3.1.1   Description of the model

Fig. 3.2a shows the model of a single degree of freedom vibration isolator with a piezo actuator and a reference mass with a relative measurement as was described in the previous chapters.

The equations of motion for the model, assuming a perfect sensor, are given by:

$$(ms^2 + k)x = k\delta + kw + F, \tag{3.1}$$

where $f = k\delta$ and $\delta = -gH(s)x$.

In Chapter 2 it was demonstrated that the transmissibility below the natural frequency is reduced by position feedback. This type of feedback has a limited phase margin near the resonance of the system as the roots of the poles are close to the imaginary axis for low damping values as is the case for a ceramic piezo-actuator. The effect is displayed in Fig. 2.9. Small phase drops due to the electronics or delays can easily render the system unstable. The next sections will compare two ways of increasing the phase margin and the effect of the sensor on the stability of the feedback system.

3.1.2 Proportional plus derivative

The first way to increase the phase margin near the resonance is to add a derivative gain in the control system starting from $\omega_c = 1/(2\pi T)$. The derivative gain adds a +90 degree phase shift to the controller increasing the phase margin. The elongation of the actuator is then given by:

$$\delta = H(s)x = -g(Ts+1)x. \tag{3.2}$$

Eq. (3.1) then becomes:

$$(ms^2 + k)x = -kg(Ts+1)x + kw + F, \tag{3.3}$$

or

$$x(s) = \frac{\omega_0^2}{s^2 + \omega_0^2 gTs + \omega_0^2(1+g)}w + \frac{1}{s^2 + \omega_0^2 gTs + \omega_0^2(1+g)}F, \tag{3.4}$$

where $\omega_0^2 = k/m$. At low frequency ($s \longrightarrow 0$), (Eq. 3.4) becomes:

$$x = \frac{1}{1+g}w + \frac{1}{\omega_0^2(1+g)}F, \tag{3.5}$$

which means that a gain of $g = 9$ will result in a reduction of 20 dB of both x/w and x/F.

Parameter T is a design parameter. It fixes the position of the zero causing the velocity feedback, on the real axis. It has to be chosen in such a way that, for the chosen value of the gain, the poles are close to the real axis (critical damping). Hence the value for T, can be found by solving the imaginary part of the solution for the poles, for T. For a fixed value of gain g, critical damping $c_{cr} = 2\sqrt{km}$ of the poles is achieved for T given by:

$$T = \frac{2\sqrt{(1+g)}}{\omega_0 g}, \tag{3.6}$$

corresponding to $T = 4.65 \times 10^{-4}$ s for a system with a piezo stiffness $k = 114$ N/μm a mass $m = 50$ kg and 1% damping. The root-locus shows the unconditional stability in Fig. 3.3 (left panel). The Nichols diagram, displayed in Fig. 3.3 (right panel), shows a phase margin of 80 degrees. The initial phase increase at low frequency is due the differentiator increasing the phase at frequencies lower than the resonance frequency. The isolation effect on the closed loop transfer function between the ground w and x is shown in Fig. 3.3 (bottom panel).
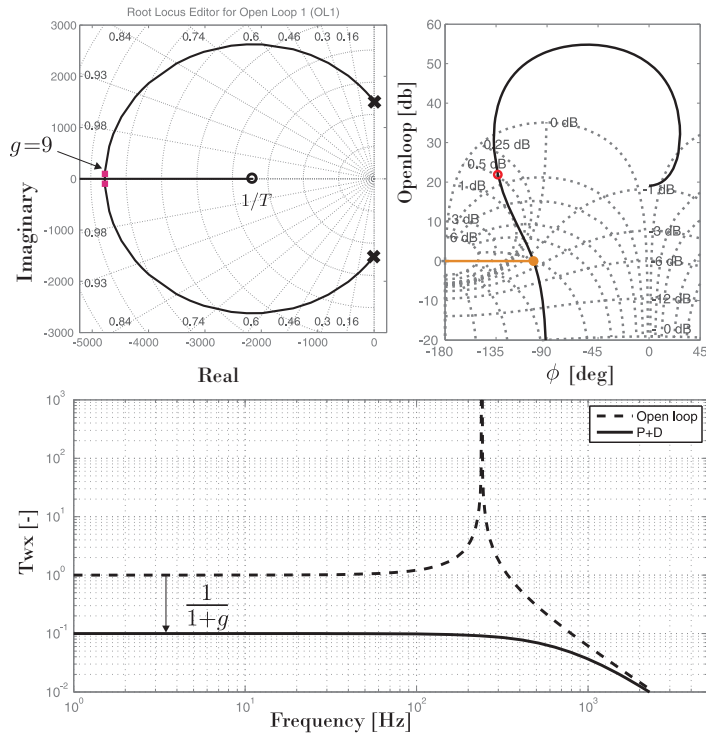
Figure 3.3: *The root-locus for a PD controller (left panel); The Nichols diagram for a PD controller (right panel); The effect on the closed loop transmissibility between the ground w and x (bottom panel).*

3.1.3   Lead compensator control

A second method to increase the phase margin at higher frequency is a lead compensator in the controller. A lead compensator increases the phase only locally due to the adding of an extra pole which limits the bandwidth of the derivation. A lead compensator is given in the Laplace domain by:

$$H_{lead}(s) = g_l \frac{Ts+1}{aTs+1}. \tag{3.7}$$

Taking the same zero position and mechanical system as for the PD controller and an $a = 0.04$ results in the rootlocus for the lead compensator configuration shown in Fig. 3.4 (left panel) The system is still unconditionally stable as the path of the root-locus is limited to the negative real part. The additional pole limiting the differentiator at higher frequencies is also displayed.
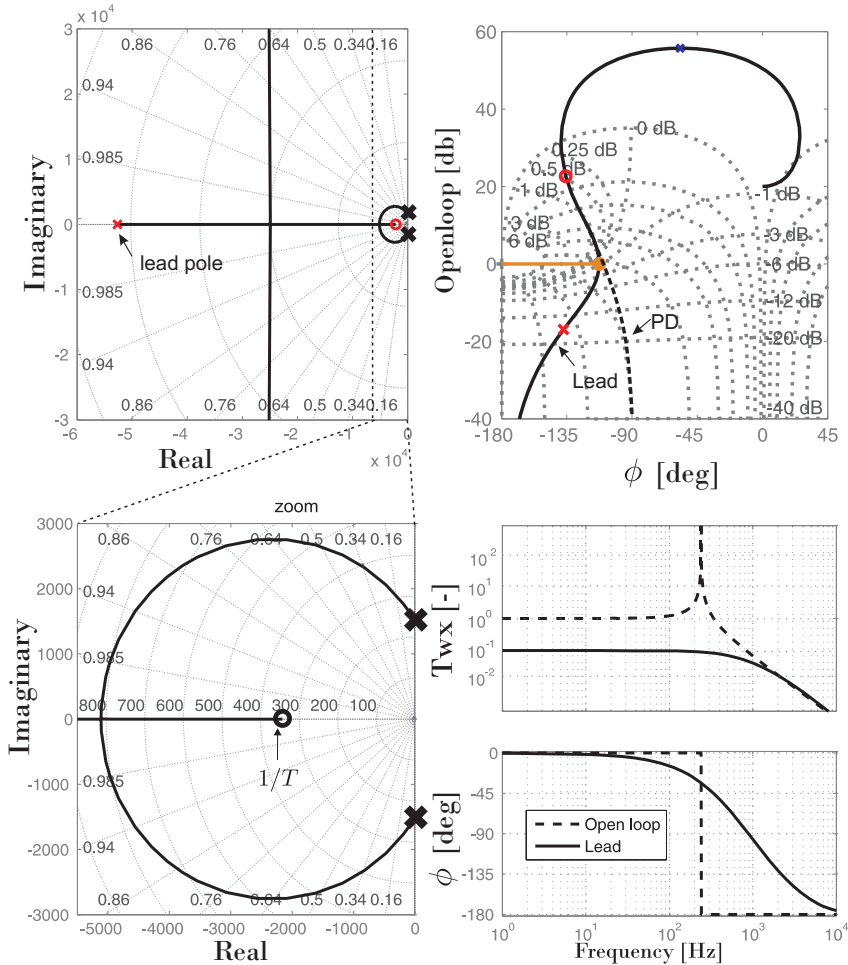
Figure 3.4: *Performance of a lead compensator controller with the root-locus (left panel); the Nichols diagram of a lead compensator controlled vibration isolation system (right panel). The effect on the closed loop transmissibility between the ground w and the top x for a lead compensator controlled vibration isolation system (right panel).*

The maximum phase lead compensator is located at the point $\omega = \frac{1}{\sqrt{aT}}$. Even with the limited derivator the phase margin remains near 80 degrees as is demonstrated in the Nichols diagram, displayed in Fig. 3.4 (top right panel).

The isolation effect on the closed loop transfer function between the ground w and x is shown in Fig. 3.4 (bottom panel). The performance remains unchanged while the gain at higher frequencies is greatly diminished (see Nichols diagram top right panel) reducing the amplification of noise sources at those frequencies. The lead compensator is therefore the better choice.
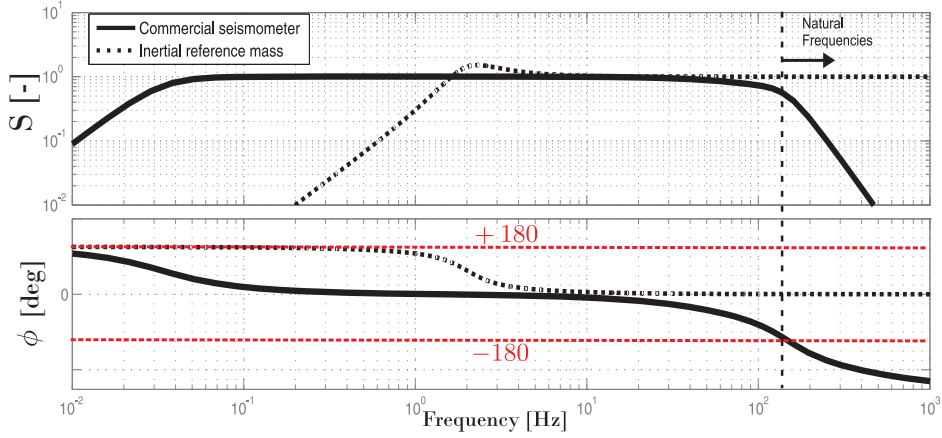
Figure 3.5: *The sensitivity curves of a geophone, acting as a perfect inertial mass, and a commercial seismometer.*

3.1.4   Effect of the sensor

As was seen in section 2.6, vibration sensors are limited to a certain bandwidth. For our analysis a system composed of an inertial reference mass, in this case a geophone, is compared with a more complex seismometer. The sensitivity curves of the two sensors are compared in Fig. 3.5.

The sensitivity curve of the geophone was chosen to have a cut off frequency at 2 Hz in order to limit the bandwidth of the cross-over system in the region that is necessary. The sensitivity of the seismometer is the sensitivity of the Guralp T6 seismometer.

Geophone

An inertial reference mass, introduces two poles at low frequency and two zeros at zero as can be seen from the geophone transfer function:

$$H_{geo}(s) = 1 - \frac{c_g s + k_g}{m_g s^2 + c_g s + kg} = \frac{m_g s^2}{m_g s^2 + c_g s + k_g}. \tag{3.8}$$

The zeros reduce the stability margin at low frequencies due to an additional +180 degree phase shift as is displayed in Fig. 3.5. A lag filter is added at low frequency, which uses its local drop in phase to increase the phase margin (see Fig. 3.6).
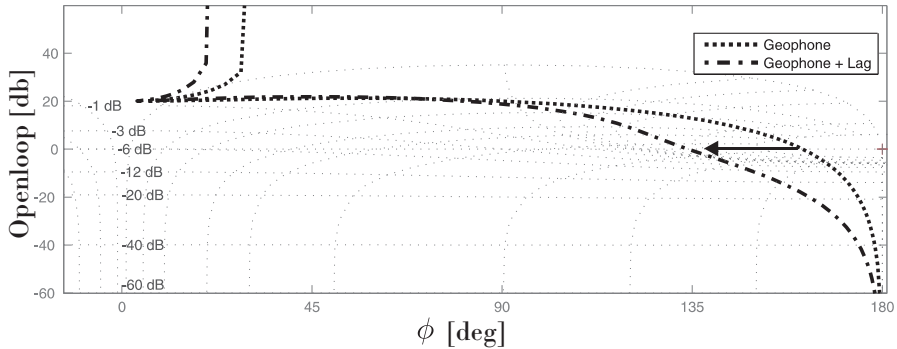
Figure 3.6: *Nichols plot showing the stability limits at low frequency for the system represented in Fig. 3.2 a, with a geophone and a geophone with a lag compensator.*

The same effect is demonstrated in Fig. 3.7. Here the root-locus for the system in Fig. 3.2a is represented and a zoomed view near the origin is shown. This is done for both a system with a geophone and a geophone with a lag compensator. The pole zero combination of the lag compensator pulls the poles of the geophone away from the right half plane, thus increasing stability.
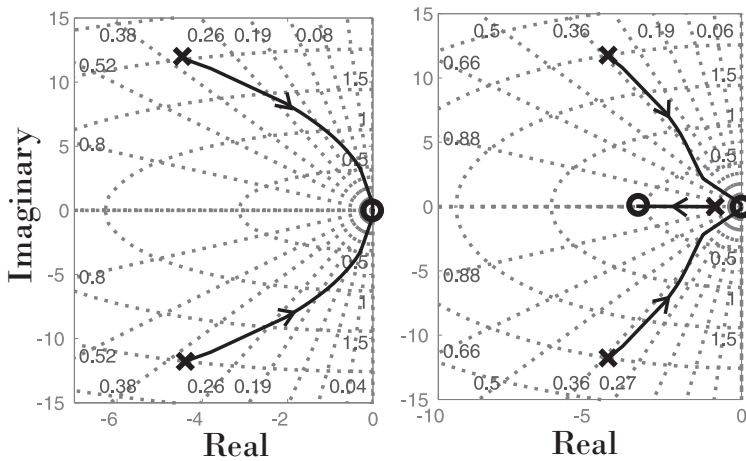
Figure 3.7: *Effect of the geophone on the root-locus zoomed near the origin (left panel); Effect of the geophone, lead and lag compensator on the root locus zoomed near the origin (right panel).*

The resulting closed loop transmissibility between the ground w and the quadrupole is displayed in Fig. 3.10.

Seismometer control

As an alternative, a seismometer can be used as a sensor. The sensitivity curve
of a Guralp T6 seismometer is shown in Fig. 3.5. Due to the poles at 60 Hz, used
to limit the bandwidth of the sensor, there is an additional phase drop in the
control loop making the system only conditionally stable. One way to increase
the gain margin (GM), the range in gain where the system is still stable, is to use
a double lag compensator. This pushes the phase drop due to the resonance out
of the bandwidth of the controller. The transfer function of the lag compensator
is the same as for the lead compensator given in Eq. (3.7). However, for a lead
compensator $a < 1$ and for a lag compensator $a > 1$. To find the optimal location
of the lag compensator, a mapping of both the gain margin and the simulated
integrated RMS @ 1 Hz, to be able to compare to the requirement RMS value,
was performed (see Fig. 3.8). They are set out against the lag compensator
corner frequency $f_l = 1/(2\pi T)$ and a for a gain $g = 9$.
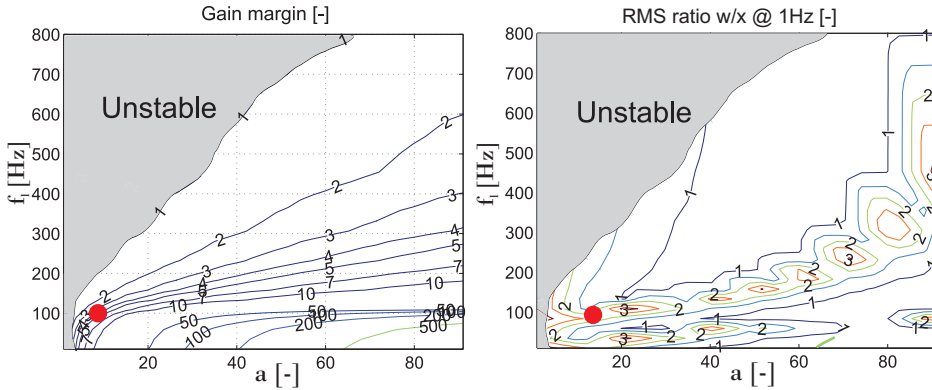
Figure 3.8: *The gain margin of the controller with a seismometer, set out
against the lag corner frequency f_l and the lag parameter a. The dot indicates
the parameters chosen in relation to performance and robustness.*

From these simulations it was chosen to have the lag compensator corner
frequency $f_l = 100$ Hz and $a = 10$. This reduces the integrated RMS displacement
of the payload at 1 Hz by a factor of 3, while the control forces and bandwidth
stay small. The resulting Nichols graph for a controller with the sensitivity curve
of the seismometer H_{geo}, a gain $g = 9$ and the double lag compensator is displayed
in Fig. 3.9 (left). The reduction in integrated RMS ground motion simulated from
a measured ground motion spectrum, shown in Fig. 1.6 is given on the right.
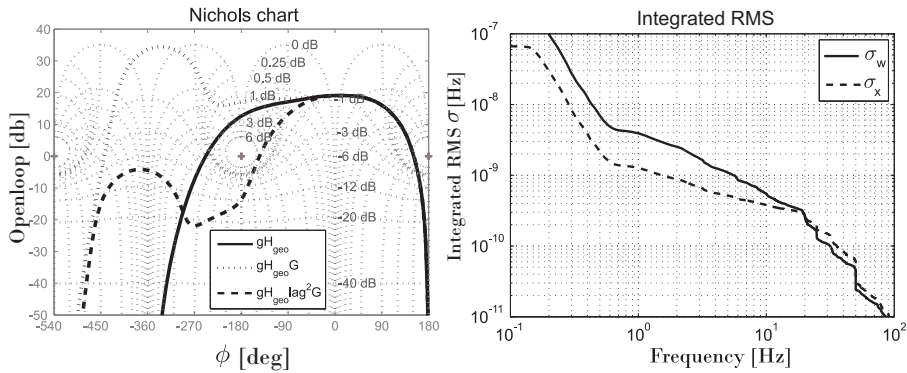
Figure 3.9: *Nichols diagram for the chosen lag compensator controller (left) and the integrated RMS composed of a measured ground excitation and the simulated reduction(right).*

The resulting closed loop transmissibility between the ground w and the quadrupole is shown in Fig. 3.10.
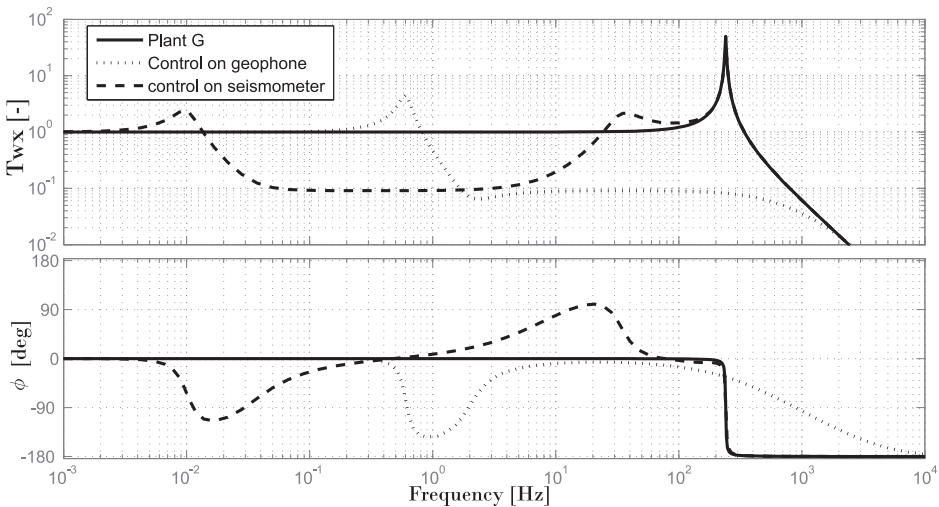
Figure 3.10: *The transmissibility between the ground w and the quadrupole x for the system with the controller off also referred to as plant G, a feedback system with a geophone and a lead compensator, and a feedback system composed of a seismometer and a double lag compensator.*

Comparison

The closed loop transfer function for both the geophone and the seismometer is given in Fig. 3.10. The difference at low frequency is due to the different sensitivity curves of the sensor. These can be changed by changing the mechanics

or the filtering within the sensor and are not a big concern. At high frequencies, the difference lies in the inclusion or exclusion of the resonance of the system in the bandwidth. By excluding it, as was done in case of the seismometer, the system is limited by the stability of the control loop due to the sensor and filters and thus has no effect on the resonance of the system. By including it, and other foreseen resonances, the system might be much less robust to unexpected resonances. This will be investigated in the next sections.

Now remembering Eq. (2.6), it was demonstrated that the closed loop error due to a change of the input signal R is given by:

$$E_{clR} = \frac{1}{1 + GD} R = SR, \tag{3.9}$$

and that the closed loop error due to sensor noise is represented by:

$$E_{clN1} = \frac{GD}{1 + GD} N_1 = \Im N_1. \tag{3.10}$$

The resulting sensitivity S and complementary sensitivity $\Im$ for both with a seismometer and a geophone are displayed in Fig. 3.11.
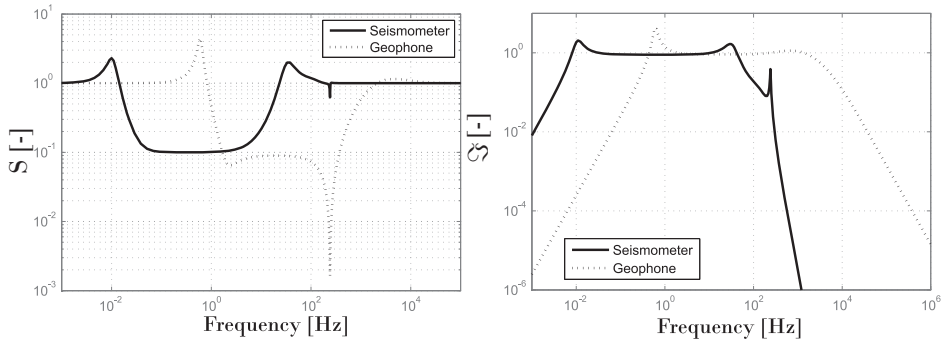
Figure 3.11: *The sensitivity S (left) and the complementary sensitivity $\Im$ (right) for both systems composed of a seismometer and a geophone.*

Preferably both S and $\Im$ are as small as possible. As they are each others complement, this is not possible. The geophone clearly has the best tracking capability as S is smallest in the largest bandwidth but this is penalized by a much higher sensitivity to noise at higher frequencies as $\Im$ stays 1 until 1000 Hz. This can be partially mitigated by using an anti-aliasing filter. The effect of a second order low pass anti-alias filter on the stability is shown in Fig. 3.12.
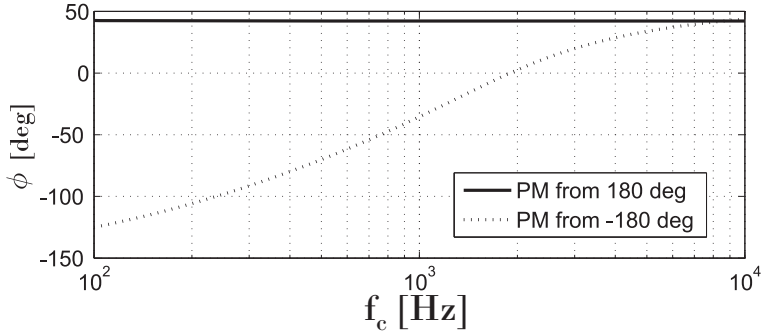
Figure 3.12: *The phase margin from both + and - 180 degree limits for the geophone feedback system with a second order anti-aliasing filter with changing cut off frequency f_c.*

In order to have sufficient phase margin, an anti-aliasing filter of 3 kHz is used.

The seismometer is capable of better tracking at lower frequencies but is more sensitive to noise at those frequencies as well.

Both sensors perform well in the reduction of vibrations in the most interesting region between 1 and 20 Hz. The geophone performs better at higher frequencies but has the risk of becoming unstable at unexpected resonances. This will be investigated in the next section.

3.2 Effect of a flexible stage

One of the additional resonances that can be expected in the system comes from the flexibility of the quadrupole. This can be modelled as a flexible appendage as is shown in Fig. 3.2b.

3.2.1 Geophone

First the influence of the flexibility of the quadrupole on the control loop using the geophone is calculated.

The equations of motion of this system are given by:

$$
\begin{aligned}
&m/2\ddot{x} + k(x - w - \delta) + k_q(x - x_q) + k_g(x - x_g) + c_g(\dot{x} - \dot{x}_g) = 0, \\
&m/2\ddot{x}_q + k_q(x_q - x) = 0, \\
&m_g\ddot{x}_g + k_g(x_g - x) + c_g(\dot{x}_g - \dot{x}) = 0.
\end{aligned}
\tag{3.11}
$$

The controller uses the lead compensator, to damp the resonance, and a lag compensator, to increase the phase margin, at low frequency as was demonstrated in the previous section.

In order to show the influence of the quadrupole stiffness k_q on the stability, the phase margins at the corresponding cross-over points are plotted against the ratio k_q/k in Fig. 3.13.
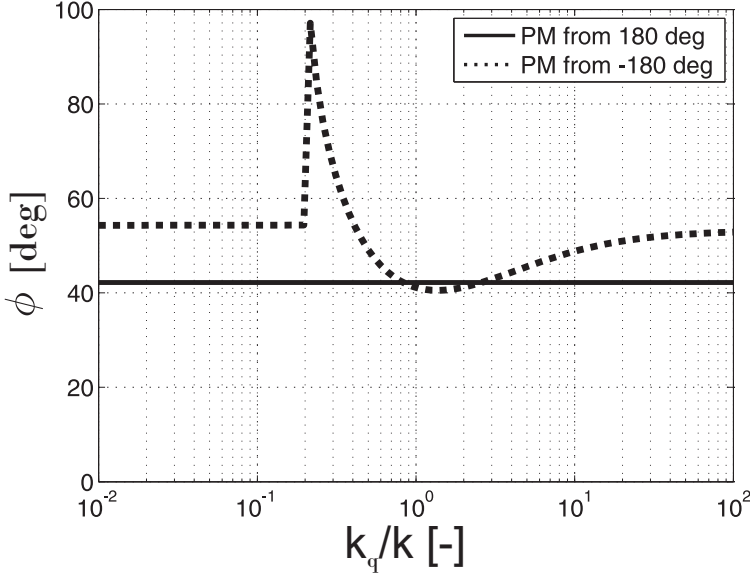
Figure 3.13: *The phase margins from 180 and -180 degrees, at their corresponding cross-over points, against the ratio k_q/k.*

There is no visible effect in the selected range of stiffness on the phase margin from 180 degrees, as it is caused by the inertial reference mass. For the stability margin to the -180 degree limit, the phase margin is always higher than 40 degrees, showing that it is always stable. This is actually normal as the sensor and the actuator work on the same degree of freedom making it collocated. A collocated system is always stable for a perfect sensor actuator pair. In this case, the geophone transmissibility does not render it unstable. The sharp turn is caused by a jump of the cross-over point from before to after the resonance.

An example showing the root-locus (top left panel) and the Nichols graph (top right panel) for the case where $k_q = k/10$ is displayed in Fig. 3.14. It clearly shows the lead compensator pulling the poles related to the highest mode away from the imaginary axis to almost critically damped values for a gain $g = 9$.

Figure 3.14: *The root-locus and Nichols graph for $k_q = k/10$ with a geophone as sensor and with a lead and a lag filter stage.*

Zooming in on the root-locus in Fig. 3.14 (bottom left panel), the poles of the lower mode are shown to go to a corresponding zero. The root-locus is pulled again away by the lead compensator from the imaginary axis. This is confirmed by looking at the closed loop transfer function in Fig. 3.15 where the lower mode

also displays a limited amount of damping.
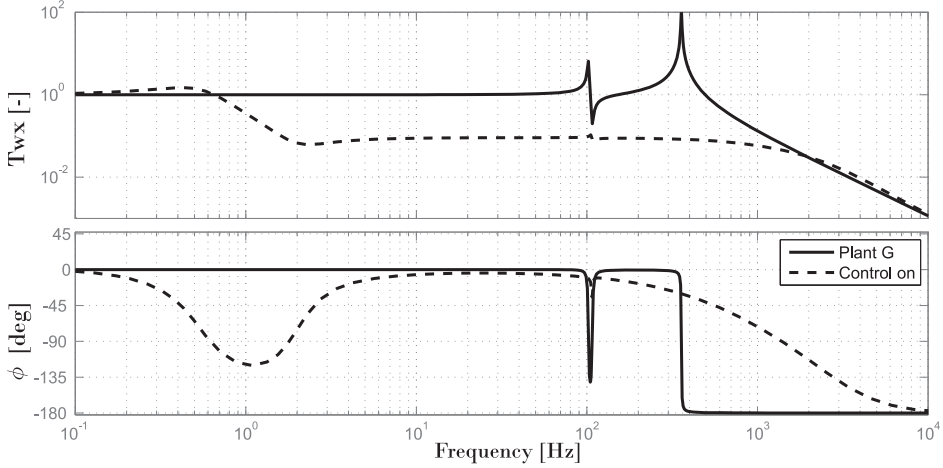
Figure 3.15: *The closed loop transmissibility between the ground and the quadrupole, for $k_q = k/10$ with a geophone as sensor and with a lead and a lag filter stage.*

Zooming even further into the root-locus in Fig. 3.14 (bottom right panel), the poles of the geophone are shown. The lag compensator is again pulling these poles away from the imaginary axis, thus increasing stability. The flexibility of the magnet will not be a problem in this set up.

3.2.2   Seismometer

To investigate the effect of the extra mode on the controller with the seismometer, the geophone was replaced by the seismometer resulting in equations of motion equal to:

$$m/2\ddot{x} + k(x - w - \delta) + k_q(x - x_q) = 0,$$
$$m/2\ddot{x}_q + k_q(x_q - x) = 0. \tag{3.12}$$

The piezo elongation is again calculated as presented in section 3.1.4. The resulting gain margin of the controller plotted as a function of the ratio of the stiffness of the piezo actuator (k) and the magnet (k_q) is given in Fig. 3.16.
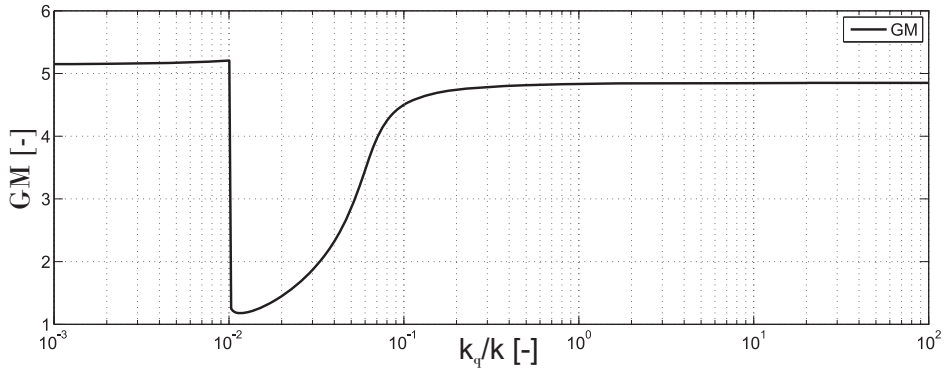
Figure 3.16: *Gain margin for the seismometer controller by using a double lag compensator with a flexible appendage representing the flexible quadrupole, for different stiffness ratio between the quadrupole (k_q) and the actuator (k).*

In order to get a better understanding of what is happening, two Nichols plots with different stiffness ratio were simulated. These are shown in Fig. 3.17 with $k_q/k = 0.02$ (left panel) and $k_q/k = 0.1$ (right panel).
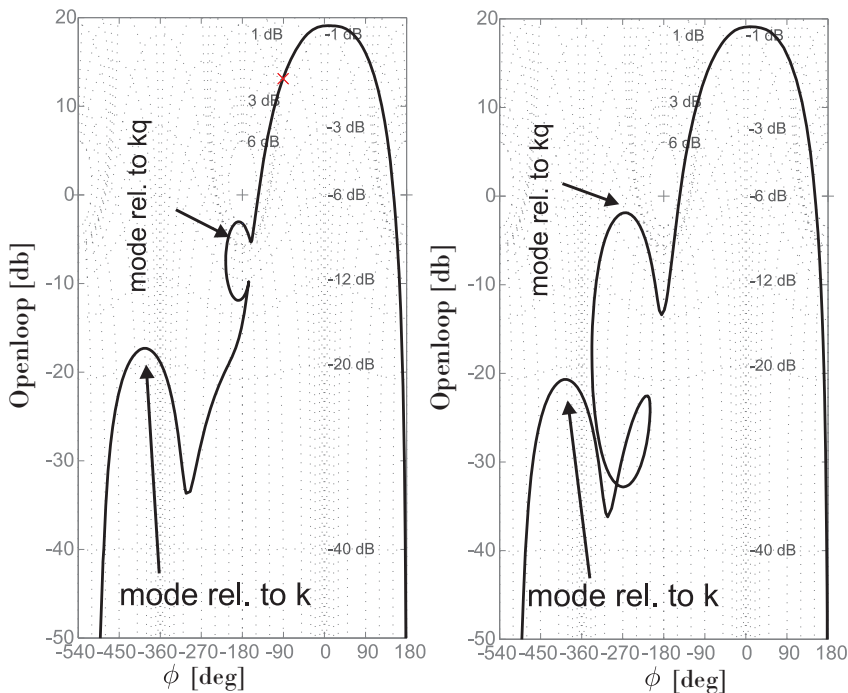
Figure 3.17: *Nichols plot for the seismometer control where $k_q/k = 0.02$ (left panel) and $k_q/k = 0.1$ (right panel).*

These two figures show that the decrease in gain margin at $k_q/k = 0.02$ is related to the first mode, influenced mainly by k_q, is near the -180 degree cross-over point. The higher k_q, the further it moves away and the higher the gain margin until it stabilizes. For $k_q/k < 0.01$, the effect of the related mode reduces and the gain margin jumps once the phase drop, caused by the anti resonance, passes the 180 degree mark. The increase in gain margin in comparison with the simple 1 d.o.f. is related to the reduction of the mass to only $m/2$ as it is assumed that the rest of the mass is carried by a secondary pair of legs.

The combination of the flexibility stage with the seismometer controller poses no problem although the gain margins become low when the resonance related to k_q magnet is close to the -180 degree cross-over point and this situation should be avoided.

3.3   Effect of the flexibility of the alignment stage

A second additional resonance is caused by adding the alignment stage under the cross-over system as is displayed in Figs. 3.1 and 3.2c. This stage consists of rotating eccentric cam-movers and is used to align the magnets into the micrometre range when there is no beam. When the accelerator is active, the alignment stage will be locked in place.

3.3.1   Geophone

The equations of motion of the system with a geophone are given by:

$$
\begin{aligned}
&m\ddot{x} + k(x - x_s - \delta) + k_g(x - x_g) + c_g(\dot{x} - \dot{x}_g) = 0, \\
&m_s\ddot{x}_s + k_s(x_s - w) + k(x_s - x + \delta) = 0, \\
&m_g\ddot{x}_g + k_g(x_g - x) + c_g(\dot{x}_g - \dot{x}) = 0.
\end{aligned}
\tag{3.13}
$$

For this first study $m_s = m = 50/2$ kg. To show the influence of the stiffness k_s on the stability, the phase margin to 180 degrees and -180 degrees at their corresponding cross-over points is plotted against the ratio k_s/k in Fig. 3.18.
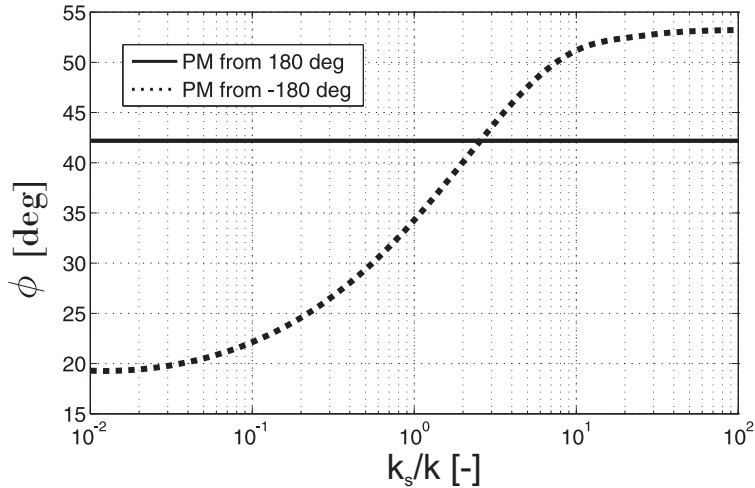
Figure 3.18: *The phase margin to 180 degrees and -180 degrees at their corresponding cross-over points against the ratio k_s/k .*

The phase margin to 180 degrees coming from the inertial reference mass is again stable at 42 degrees. The phase margin towards -180 degrees drops however below 42 degrees when $k_s < 2.5 \times k$. This can be as low as 20 degrees and is due to the fact that the poles of the mode are going away from the lead compensator and results in an increase in phase margin. However, the alignment system under the cross-over system does not have a destabilizing effect on the feedback controller and the feedback controller is still unconditionally stable as sensor and actuator are still collocated.
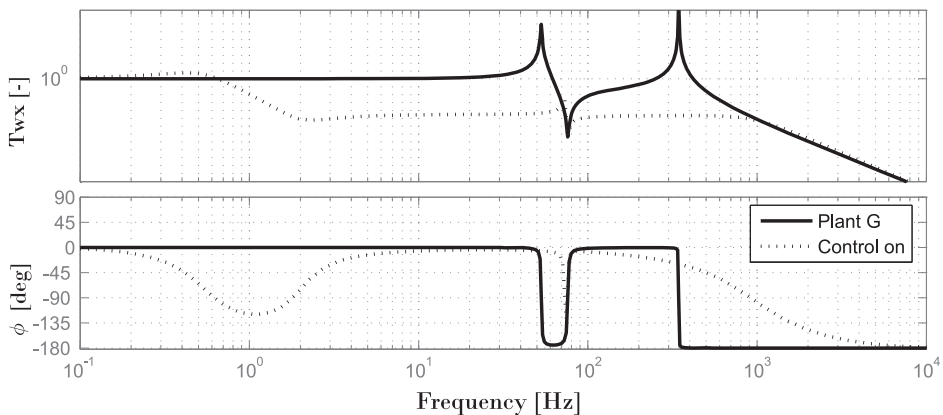
Figure 3.19: *The closed loop transmissibility between the ground and the quadrupole, for $k_s = k/10$ with a geophone as sensor and with a lead and a lag filter stage..*
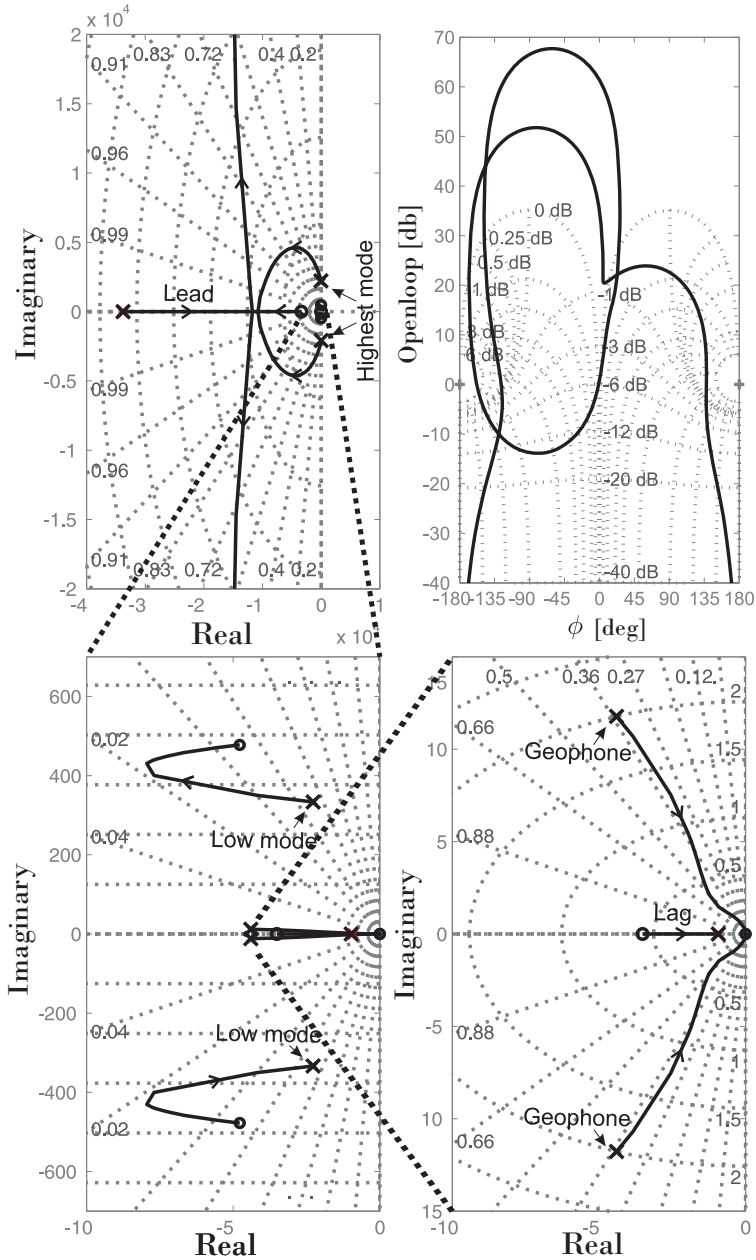
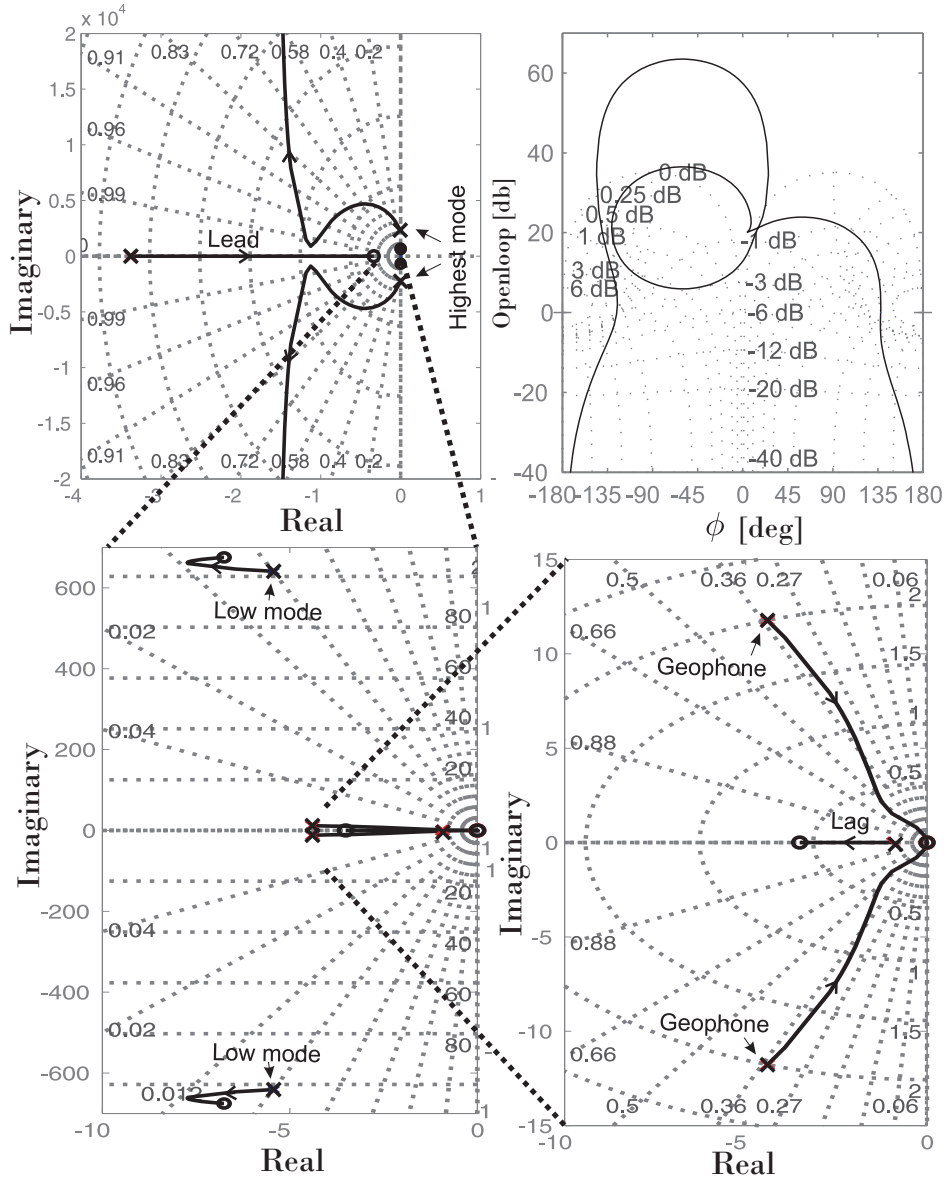**Figure 3.20:** *The root-locus and Nichols graph for $k_s = k/10$ with a geophone as sensor and with a lead and a lag filter stage..*

The root-locus (top right panel) and Nichols diagram for $k/k_s = 10$ are shown in Fig. 3.20. A zoom towards the origin of the root-locus is displayed in the

bottom left panel and bottom right panel. They show the effect of the lead compensator on the lowest mode and the lag compensator on the geophone poles. The closed loop transmissibility between the ground w and the quadrupole x is displayed in Fig. 3.19. As long as the actuator and the sensor stay collocated, the system will remain stable.

In order to understand the evolution of the gain margin, three Nichols graphs are shown in Fig. 3.21.
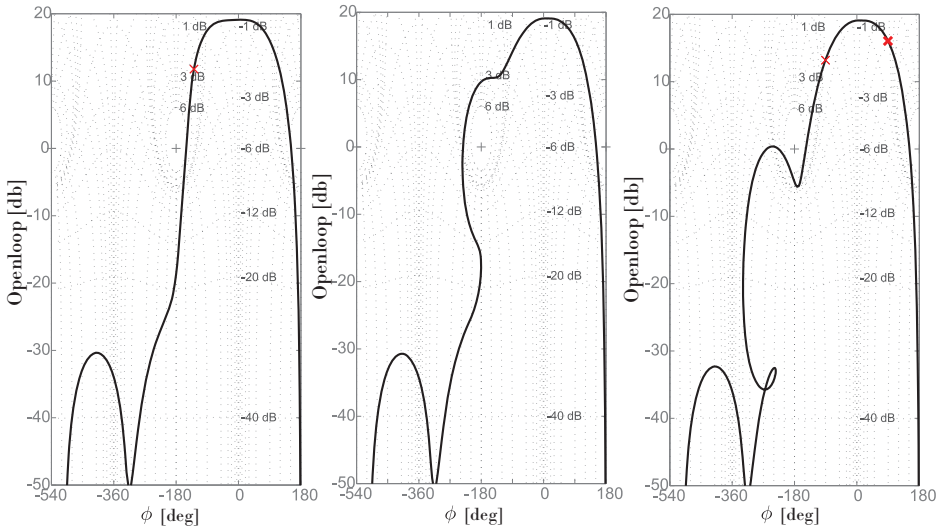
Figure 3.21: *Nichols graphs for a system with $k_s/k = 0.001$ (left panel), $k_s/k = 0.01$ (middle panel) and $k_s/k = 0.1$ (right panel).*

For a stiffness ratio between $0.003 < k_s/k < 0.1$ the system is unstable. This is roughly when the mode related to k_s passes the poles of the seismometer until the mode passes under the 0 dB line at around 75 Hz. This area will have to be avoided at all costs by the alignment system. This is not a large problem as the requirements were defined as no modes below 100 Hz.

3.4 Effect of a flexible quadrupole and alignment stage

Both the alignment stage, the cross-over stage and the flexural mode will exist simultaneously in the Type 4 magnet as is shown in Fig. 3.2d.

3.4.1   Geophone

The equations of motion of the masses are represented through:

$$m/2\ddot{x} + k(x - x_s - \delta) + k_q(x - x_q) + k_g(x - x_g) + c_g(\dot{x} - \dot{x}_g) = 0,$$
$$m/2\ddot{x}_q + k_q(x_q - x) = 0,$$
$$m_s\ddot{x}_s + k_s(x_s - w) + k(x_s - x + \delta) = 0,$$
$$m_g\ddot{x}_g + k_g(x_g - x) + c_g(\dot{x}_g - \dot{x}) = 0. \tag{3.14}$$

Two surface plots for the phase margin to -180 and 180 degrees at their corresponding cross-over points were simulated and are shown in Fig. 3.22 for a range of k_s and k_q values.
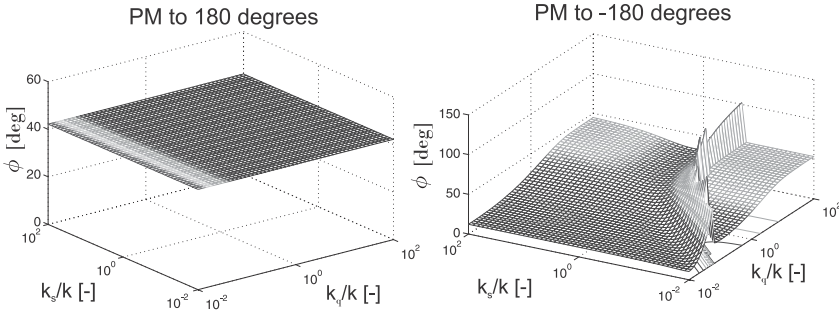
Figure 3.22: *The phase margin to -180 degrees at its corresponding cross-over point (left panel); The phase margin to 180 degrees at its corresponding cross-over point (right panel).*

Fig. 3.22 (left panel) confirms again that the phase margin at the cross-over point towards 180 degrees, due to the inertial sensor, is nearly constant in the given stiffness range. The higher stability limit towards -180 degrees (see Fig. 3.22 (right panel)) becomes too low (15 degrees) as the modes are less influenced by the lead compensator at lower values of the mode. The system will however continue to be unconditionally stable as long as the sensor and actuator are collocated.

3.4.2   Seismometer

The same analysis was done for the seismometer controller represented in section 3.1.4. Both k_s and k_q were changed and the gain margin for the controller was calculated. The results are shown in Fig. 3.23.
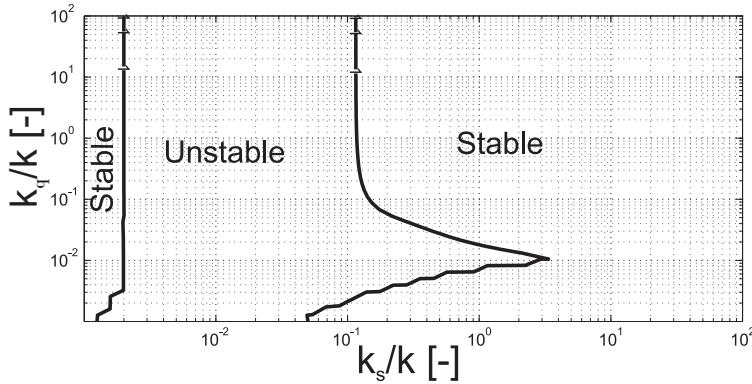
Figure 3.23: *The gain margin for a system represented in Fig 3.2d by using a seismometer for vibration isolation represented in section 3.1.4.*

The results largely show the same unstable region as was found in the systems represented in Fig. 3.2b and c. The area around the cross-over point should be avoided with all modes due to the filter of the seismometer. Therefore, all modes should be above 100 Hz to be safe.

3.5 Flexible joint

Due to the movements required, a flexible joint is needed to protect the brittle piezo actuator from shear, moment and tension forces. Due to this flexible element, the sensor actuator pair will not work on the same degree of freedom as is displayed in Fig. 3.2e.

3.5.1 Geophone

The equations of motion of the masses are calculated through the differential equations:

$$m\ddot{x} + k_j(x - x_j) + k_g(x - x_g) + c_g(\dot{x} - \dot{x}_g) = 0,$$
$$m_g\ddot{x}_g + k_g(x_g - x) + c_g(\dot{x}_g - \dot{x}) = 0,$$
$$m_j\ddot{x}_j + k(x_j - w - \delta) + k_j(x_j - x) = 0, \tag{3.15}$$

or in matrix format:

$$M\ddot{X} + C\dot{X} + KX = B\delta + Ew, \tag{3.16}$$

with M, C and K the respective mass, damping and stiffness matrix of the system. Vector X includes the different position parameters. Matrix E represents

the input matrix for the ground motion w and B the input matrix for the actuator
displacement which is given by $\delta = H(s)(x - x_g)$. The controller $H(s)$ includes the
lag and a lead compensator, to increase phase margins and damp the resonances
presented in section 3.1.4 and 3.1.3 respectively. The resulting root-locus plot is
compared in Fig. 3.24 to the root-locus of the single degree of freedom system
presented in section 3.1.1. The joint stiffness for this example is $k_j = 10k$.
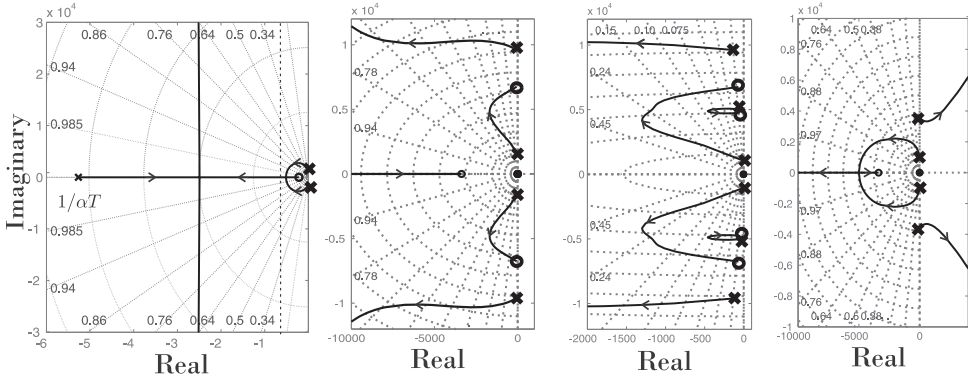
Figure 3.24: *Root-locus related to the system of Fig. 3.2 (a), representing
the single degree of freedom system (left panel); Root-locus of Fig. 3.2 (b),
representing a system including the alignment stage (middle left panel); Root-
locus of Fig. 3.2 (d), representing a system with both a flexible magnet and an
alignment system (middle right panel); Root-locus of Fig. 3.2 (e), representing a
system with a flexible joint between the actuator and the payload (right panel).*

For collocation, the sensor and the actuator need to work on the same degree
of freedom x and the sensor-actuator pair needs to be dual. They are dual when a
translation sensor (displacement, velocity, acceleration) is associated with a force
actuator or an angular sensor with a torque actuator [25]. The system with a
flexible joint shown in Fig. 3.2e is not collocated as the actuator works on x_j and
the sensor measures x disrupting the alternating pole zero pattern. Mechanical
poles that are not compensated by a zero will go to an asymptote. The angle of
these asymptotes is given by the excess number of poles (n) with respect to zeros
(m) by [19]:

$$\phi_l = \frac{180° + 360°(l-1)}{n-m},\tag{3.17}$$

where $l = 1, 2, ..., n - m$. For the configuration given in Fig. 3.2a, 3.2b, 3.2c
and 3.2d there are two poles more than zeros resulting in two asymptotes going
to ± 90 degrees. The position of these asymptotes on the real axis is given by:

$$a = \frac{\sum p_i - \sum z_i}{n - m}. \tag{3.18}$$

Since the poles and zeros always appear as complex conjugate pairs, the imaginary parts add to zero. As the pole of the lead compensator is located much further in the left half plane than the combination of the zeros, the two asymptotes will always be located in the left half plane. For the system with a joint there are eight poles and five zeros resulting in three asymptotes. One has an angle of 180 degrees with a pole going to $-\infty$ and two with an angle of ± 60 degrees. The last two poles cause the system to be only conditionally stable as their poles will quickly wander into the right half plane.

The stability can be increased by adding damping and/or increasing the stiffness of the flexible joint, in this way moving the pole further into the left half plane. Alternatively, the sensor and actuator can be made collocated again by relocating the reference mass on to m_j and measuring the relative displacement between x_j and the reference mass x_g removing the problem. Measuring on top of the magnet with a geophone while including the resonances of the system is dangerous when the actuator and sensor are not collocated.

3.5.2 Seismometer

The equations of motion of the system represented in Fig. 3.2e, with a seismometer are given by:

$$m\ddot{x} + k_j(x - x_j) = 0,$$
$$m_j\ddot{x}_j + k(x_j - w - \delta) + k_j(x_j - x) = 0. \tag{3.19}$$

The controller has remained the same as in section 3.1.4. The same actuator is used while $m = 50$ kg and $m_j = m/100$. The stiffness of the joint (k_j) is changed gradually to investigate the effects of the mode on the controller. The resulting gain margin is shown in Fig. 3.25.

In order to understand the evolution of the gain margin, three Nichols graphs are shown in Fig. 3.26.
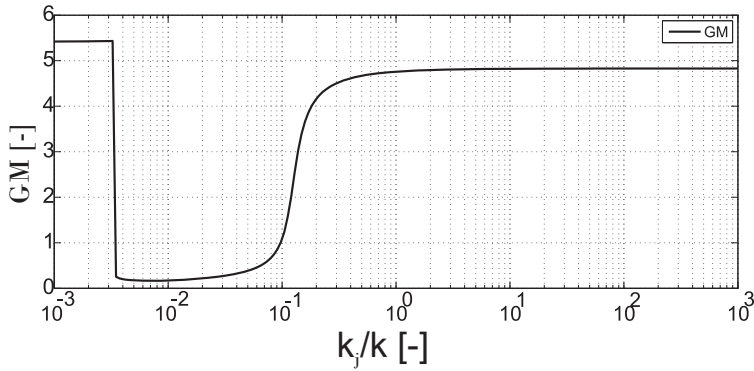
Figure 3.25: *Gain margin for the system shown in Fig. 3.2 (e) using the seismometer controller of section 3.1.4.*
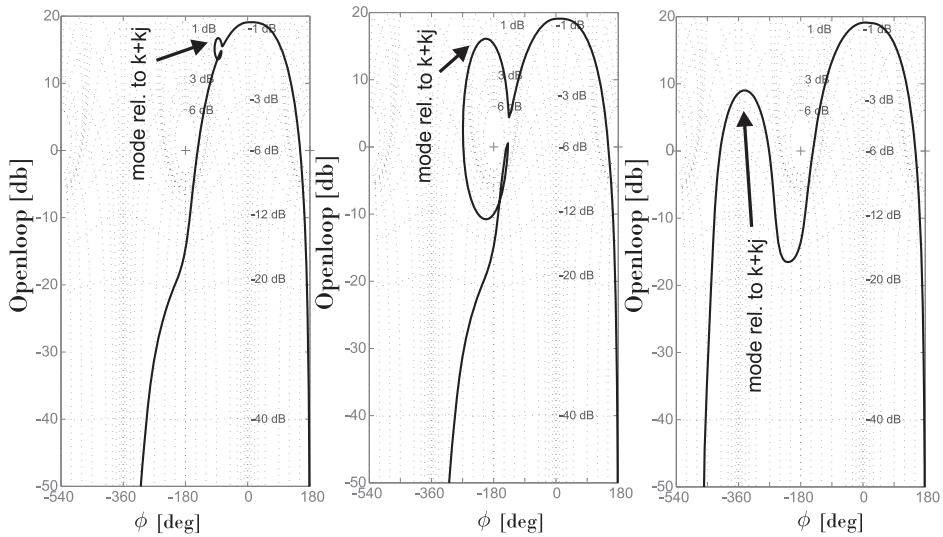
Figure 3.26: *Nichols graphs for a system with $k_j/k = 0.001$ (left panel), $k_j/k = 0.01$ (middle panel) and $k_j/k = 1$ (right panel).*

Instead of two modes we now have only a single mode visible. This is the combined mode of the system. When the stiffness ratio $0.0035 < k_j/k < 0.095$ the system is unstable as the combined mode approaches the -180 degree crossover point. Once the mode is under the 0 dB line the system is stable again. A second mode related to m_j is located near -100 dB but does not influence stability. The first combined mode of the system thus should avoid the cross-over point.

3.6 Summary

In this chapter it was demonstrated that the transmissibility between the ground w and the payload x can be reduced and resonances can be damped with a PD controller where the position x is applied as a feedback for a single degree of freedom system. A pole can be used to limit the bandwidth of the derivative part.

By introducing a geophone as a sensor, the phase margin at low frequency is reduced. This drop in phase margin can be counter-acted by employing a lag compensator at low frequency.

If a seismometer is used, then the main stability issues come from the low pass filters at high frequencies combined with the phase drop caused by the resonance. By adding a double lag compensator the resonance and the majority of the phase drop due to the seismometer is removed from the bandwidth. This allows for a transmissibility reduction of a factor 3 in the bandwidth required and an RMS reduction of 3 for a measured ground vibration spectrum. Additional resonances are not a problem as long as they are well outside the bandwidth of the sensor.

The geophone can provide a wider bandwidth for vibration reduction but will be more susceptible for disturbing resonances and effects as delay and additional lags coming from the actuator. The flexibility of the magnet and the flexibility of the alignment system were proven not to cause instabilities of the feedback system when a geophone and actuator stay collocated and dual. However, when a flexible joint is introduced between the actuator and the quadrupole on which the sensor measures the motion, this can lead to instability. The stability can be improved by increasing the stiffness and damping of the joint or by making the actuator sensor pair collocated again and measuring the actuator motion. A summary is given in Table 3.1.

	Geophone	Seismometer
Bandwidth	++	+
Sensitivity to resonances collocated	++	+ (when out of bandwidth)
Sensitivity to resonances non-collocated	−	- (when out of bandwidth)

Table 3.1: *Summary table geophone and seismometer sensitivities.*

The geophone has thus better performance but will need to be collocated with the actuator in order to avoid instability issues. Due to the size, sensitivity and implementation requirements for a collocated sensor, a new sensor/sensor case will have to be developed but this is beyond the scope of the present thesis.

Chapter 4
Multiple degree of Freedom stabilisation

This chapter will propose several mechanical concepts to stabilize the magnets, shown in Fig. 4.1 in multiple degrees of freedom. A first study is done in 2D and a 3D concept is proposed. These concepts have also been presented in Refs. [63] and [64].
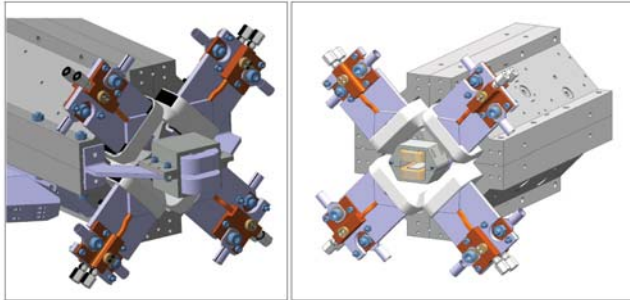
Figure 4.1: *The type 1 and Type 4 magnets to be stabilized by the control system. Figure adapted from Ref. [5].*

4.1   Mechanical Design concepts 2D

In this section the influence of the attachment and angle of the legs is studied in 2D. The concepts will be judged by their modes as they are the main sources of instabilities. Due to the beam based orbit feedback and the shape of the ground motion in the frequency domain (see chapter 1), a mode under 50 Hz will be unacceptable, a mode between 50 and 100 Hz will require active damping and above 100 Hz is preferred. The actuators that are considered for these concepts are PI 225.1S piezo actuators with a stiffness of $k_a = 480$ N/μm. They have a push capacity $F_{psh} = 12500$ N but only a pull capacity of $F_{pull} = 2000$ N. Further they have a shear force limit of $F_{sh} = 255$ N, a bending limit $M_B = 2$ Nm and

a torque limit $M_T = 1.5$ Nm. This means that shear forces and torque moments should be limited. This is done by using a double jointed flexural hinge as is shown in Fig. 4.2.

Figure 4.2: *The flexural hinge designed by K. Artoos (left) and the flexural hinges combined with a PI piezo actuator (right).*

The flexural stiffness of the hinge along the two flexural axis is $k_e = 223$ Nm/rad. The longitudinal stiffness of the hinge is $k_j = 300$ N/μm. Combining the stiffness of the joint with the actuator results in the stiffness of the leg calculated with:

$$k = \frac{1}{\frac{1}{k_a} + \frac{1}{k_j} + \frac{1}{k_j}} = 114\text{N}/\mu\text{m}. \tag{4.1}$$

Further it was decided that the longitudinal degree of freedom of the magnet should be blocked and the rotation of the magnet should be limited. The concepts will also be judged on transportability, as the modules with the magnets will be transported completely integrated in the tunnel, and feasibility.

4.1.1   Leg position and angle

First a general equation of motion for arbitrary leg attachment and angles is derived for a magnet in a 2D plane as is represented in Fig. 4.3. Then an optimization is done to determine the best leg configuration.

Fig. 4.4 shows the movement of the attachment point of the leg in the frame X_1, Y_1 and its corresponding movement in the reference frame of the leg (α_1, q_1). The angle β_1 is the initial angle of the leg and L_1 is the initial length of the leg.
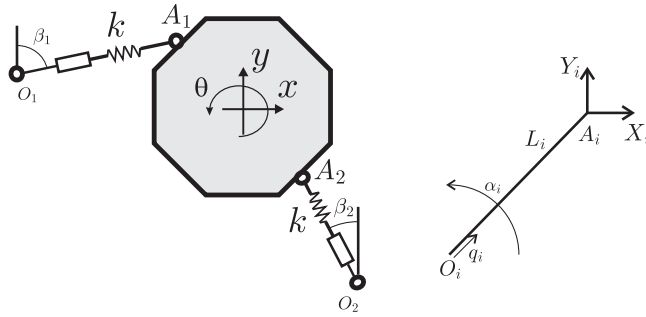
Figure 4.3: *A schematic view of a magnet with two legs positioned arbitrarily on the magnet (left panel) and the reference frame of the leg $(O_i = (q_i, \alpha_i))$ connected to the reference frame of the attachment point $(A_i = (X_i, Y_i))$.*
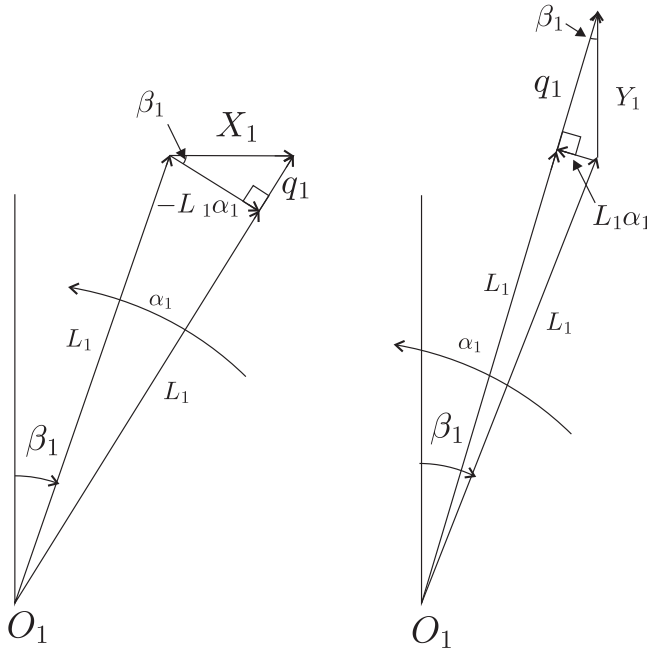
Figure 4.4: *The effect of a motion in the X_i direction in the leg coordinate system (left panel) and the effect of a motion in the Y_i direction in the leg coordinate system (right panel).*

This results in a transfer matrix between the reference frame of the attachment point (X_1, Y_1) and the leg (α_1, q_1) given by:

$$\begin{bmatrix} q_i \\ \alpha_i \end{bmatrix} = \begin{bmatrix} \sin(\beta_i) & \cos(\beta_i) \\ \frac{-\cos(\beta_i)}{L_i} & \frac{\sin(\beta_i)}{Li} \end{bmatrix} \begin{bmatrix} X_i \\ Y_i \end{bmatrix}. \tag{4.2}$$

In order to go from the reference frame of the attachment point of the leg, which has 2 degrees of freedom, to the 3 degrees of freedom system of the whole magnet, a constraint is applied. The constraint is the location of attachment point $A_i = (d_{xi}, d_{yi})$ locking the position of the reference frame X_i, Y_i resulting in the transfer matrix between the two reference frames:

$$\begin{bmatrix} X_i \\ Y_i \end{bmatrix} = \begin{bmatrix} 1 & 0 & -d_{yi} \\ 0 & 1 & d_{xi} \end{bmatrix} \begin{bmatrix} x \\ y \\ \theta \end{bmatrix}. \tag{4.3}$$

Combining the transformation matrices in Eqs. (4.2) and (4.3) results in a transfer matrix between the leg and the magnet reference frame:

$$\begin{bmatrix} q_i \\ \alpha_i \end{bmatrix} = \begin{bmatrix} \sin(\beta_i) & \cos(\beta_i) & -d_{yi}\sin(\beta_i) + d_{xi}\cos(\beta_i) \\ \frac{-\cos(\beta_i)}{L_i} & \frac{\sin(\beta_i)}{Li} & d_{yi}\frac{\cos(\beta_i)}{L_i} + d_{xi}\frac{\sin(\beta_i)}{L_i} \end{bmatrix} \begin{bmatrix} x \\ y \\ \theta \end{bmatrix}. \tag{4.4}$$

The equations of motion will be calculated through the Lagrangian L with the kinetic T and potential V energy of the system:

$$L = T - V. \tag{4.5}$$

The kinetic energy of the mass is given by:

$$T = \frac{1}{2}m\dot{x}^2 + \frac{1}{2}m\dot{y}^2 + \frac{1}{2}I\dot{\theta}^2, \tag{4.6}$$

where m is the mass of the magnet and I its mass moment of inertia. The potential energy for N legs is given by:

$$V = \sum_{i=1}^{N} \frac{1}{2}kq_i^2 + \frac{1}{2}k_{ei}\alpha_i^2 + \frac{1}{2}k_{ei}(\alpha_i - \theta)^2. \tag{4.7}$$

Implementing the transfer matrix in the potential energy and using it to calculate the Lagrangian allows to calculate the equations of motion through:

$$\frac{d}{dt}\left(\frac{\delta L}{\delta \dot{s}}\right) - \frac{\delta L}{\delta s} = 0, \tag{4.8}$$

with $s = x, y, \theta$. This results in the equation of the recognizable matrix form:

$$M\ddot{X} + KX = 0, \tag{4.9}$$

with $X = [x, y, \theta]^T$. Since the solution of these differential equations should be:

$$s(t) = s_0 e^{-i\lambda t}, \qquad (4.10)$$

and thus

$$\ddot{s} = -\lambda^2 s. \qquad (4.11)$$

the poles or modes of the mechanical system are given by the solution of:

$$-\Lambda^2 M + K = 0. \qquad (4.12)$$

All the proposed systems will be judged on all the modes of the system and its influence on the stability of the feedback loop.

4.1.2 Quadrupole stabilisation with 3 legs

The easiest solution to control 3 degrees of freedom is to use three legs. An example of a three legged configuration is given in Fig. 4.5 (left panel). For this configuration $\beta_1 = \beta_2 = 0$ degrees, $\beta_3 = -90$ degrees, $d_{x1} = -0.1$ m, $d_{x2} = d_{x3} = 0.1$ m and $d_{y1} = d_{y2} = d_{y3} = 0$ m.
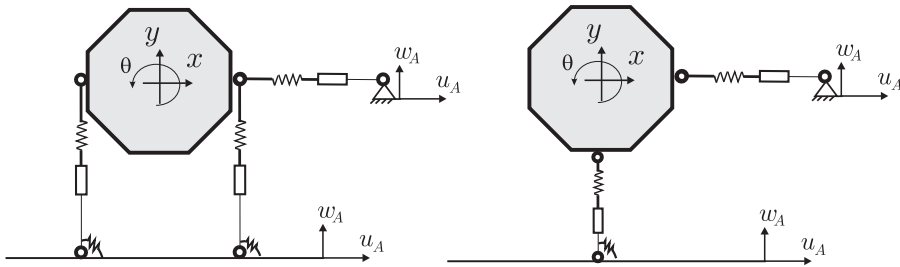
Figure 4.5: *A schematic representation of a quadrupole stabilisation with three legs (left panel) and two legs (right panel).*

The resulting modes are given in Table 4.1.

	f_1	f_2	f_3
[Hz]	276	390	499
x	1	0	0
y	0	1	0
θ	0	0	1

Table 4.1: *The three modes and their eigenvectors of the system with 3 legs attached at $d_{x1} = -0.1$ m, $d_{x2} = d_{x3} = 0.1$ m, $d_{y1,2,3} = 0$ m for $\beta_1 = \beta_2 = 0$ degrees and $\beta_3 = -90$ degrees.*

Using three legs results in modes within the required range. However each active leg uses an amplifier and a control system which drives up the cost significantly. Further only two degrees of freedom are necessary in the requirements (x,y). So only two active legs should be necessary, and this approach will be investigated in the next section.

4.1.3   Quadrupole stabilisation with 2 legs

Removing one leg and making the remaining legs cross the centre of gravity results in Fig. 4.5 (right panel). In this configuration, the x and y-direction are controllable but not the roll θ. There is also an effect on the modes of the system as can be seen in Table 4.2.

	f_1	f_2	f_3
[Hz]	276	276	14
x	1	0	0
y	0	1	0
θ	0	0	1

Table 4.2: *The three modes and their eigenvectors of the system with 2 legs attached at $d_{x1} = 0$ m, $d_{x2} = 0.1$ m, $d_{y1} = -0.1$ and $d_{y1} = 0$ m for $\beta_1 = 0$ and $\beta_2 = -90$ degrees.*

The mode in the y-direction is lower, as one of the supporting legs is eliminated, but still acceptable. The mode in the roll direction is only 14 Hz and thus unacceptable. Additionally there is no protection for the piezo actuators to tension forces. One way to improve the protection against tensile forces is to use the mass of the magnet to provide a pre-compression force. In order to investigate the possibilities, two legs were attached at $d_{x1} = -0.1$ m, $d_{x2} = 0.1$ m, $d_{y1,2} = 0$ m for different values of $\beta = \beta_1 = -\beta_2$ as is shown in Fig. 4.6 (left panel).
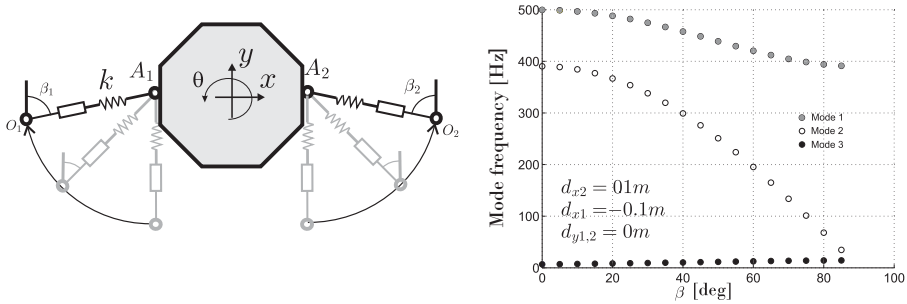
Figure 4.6: *The attachment of two legs with varying angle (left panel). The three modes of the system with 2 legs attached at $d_{x1} = -0.1$ m, $d_{x2} = 0.1$ m, $d_{y1,2} = 0$ m for different values of $\beta = \beta_1 = -\beta_2$ (right panel).*

Fig. 4.6 (right panel) represents the evolution of the different modes for $\beta = \beta_1 = -\beta_2$. It shows clearly that the angle of the legs does not have a large effect on the lowest and the highest mode. However the middle mode is clearly affected. In order to understand this evolution the eigenvectors are represented in Table 4.3.

$\beta=20$	f_1	f_2	f_3	$\beta=45$	f_1	f_2	f_3	$\beta=80$	f_1	f_2	f_3
[Hz]	8.3	366	488		10.9	276	448		394	14	68
x	0.96	0	0.27		0.78	0	0.61		0.97	0.22	0
y	0	1	0		0	1	0		0	0	1
θ	0.27	0	0.96		0.68	0	0.78		0.22	0.97	0

Table 4.3: *The three modes and their eigenvectors of the system with 2 legs attached at $d_{x1} = -0.1$ m, $d_{x2} = 0.1$ m, $d_{y1,2} = 0$ m for different values of $\beta = \beta_1 = -\beta_2$.*

For $\beta = 20$ degrees, there is a mode composed of the x direction and θ direction which is low. This is due to the legs being barely inclined. The y and rotational modes are however high as the legs are almost vertical and are tangent to a circle around the rotation point. For $\beta = 80$ degrees, the mode in x-direction is high and the other two are low. Since the y-direction is of much more importance than the x-direction, for the stabilisation requirements (1 nm vs 5 nm), an angle of 20 degrees is chosen. In order to find the best attachment points, the attachment points are changed on a circle with radius r around the rotation point as is shown in Fig. 4.7
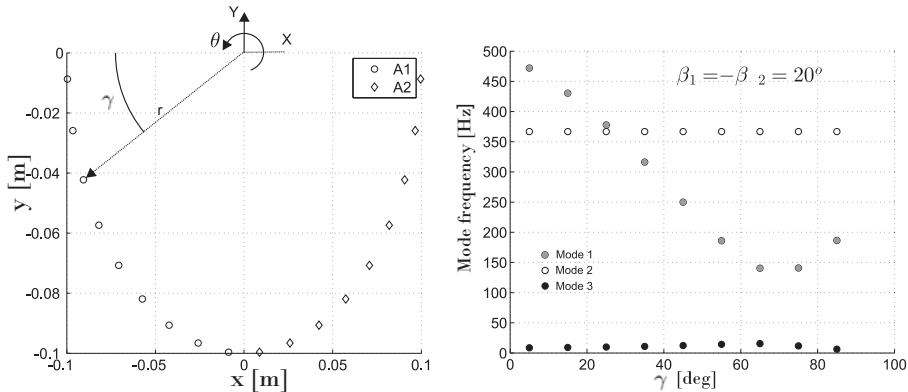
Figure 4.7: *The symmetric evolution of the two attachment points of the two legs (A_1, A_2) on a circle with $r = 0.1$ m and changing γ resulting in $d_{x1} = -r\cos(\gamma)$ m, $d_{x2} = r\cos(\gamma)$ m, $d_{y1,2} = -r\sin(\gamma)$ (left panel) and the three modes of the system with changing γ for $\beta = \beta_1 = 20$ degrees (right panel).*

Fig. 4.7 (right panel) shows that having the attachment point at small values of γ or in other words on or near the x-axis is preferred. This is due to the larger circle around the rotation point to which the legs are tangent to, applying a larger moment force to block the rotation. There is however one mode which stays low. In order to investigate this mode, several solutions for γ are represented in Table 4.4.

$\gamma=20$	f_1	f_2	f_3	$\gamma=45$	f_1	f_2	f_3	$\gamma=80$	f_1	f_2	f_3
[Hz]	9.5	366	405		12	249	366		159	8.7	366
x	0.94	0	0.32		0.84	0.53	0		0.83	0.54	0
y	0	1	0		0	0	1		0	0	1
θ	0.32	0	0.94		0.53	0.84	0		0.54	0.83	0

Table 4.4: *The three modes and their eigenvectors of the system with 2 legs with changing attachment point symmetrically changing according to $d_{x1} = -r\cos(\gamma)$ m, $d_{x2} = r\cos(\gamma)$ m, $d_{y1,2} = -r\sin(\gamma)$ m for $\beta = \beta_1 = 20^o$.*

For $\gamma = 20$ degrees, the low mode consists of a combination of a movement in x-direction and a movement around θ as is displayed in Fig. 4.8 (left panel). This mode is also called the '4-bar' mode as it moves as a 4 bar linkage system. In the next section a solution to increase the frequency of this mode is researched.

4.1.4   4-bar mode and solutions

There are two possible solutions proposed for the '4-bar' mode. A 'bellows' can be inserted in the rotation point of the mode as is displayed in Fig. 4.8 (middle panel). This is an element which is stiff in rotation but flexible in the x and y direction in order to keep the reaction forces small when the magnet moves. A second solution is to put shear pins far away from the rotation point. This is represented in Fig. 4.8 (right panel). By putting pins with a reasonably low stiffness, far away from the rotation point of the '4-bar' mode, they give a moment force increasing this mode without inducing too much reaction forces in the x and y direction. Additionally they give a high stiffness in the longitudinal direction of the magnet, blocking that direction with high stiffness springs.

Both solutions are investigated in the next two sections.

A. Bellows

The relation between the bellow reference frame (X_b, Y_b, θ_b) and the magnet reference frame (X, Y, θ) is given by:

$$\begin{bmatrix} X_B \\ Y_B \\ \theta_B \end{bmatrix} = \begin{bmatrix} 1 & 0 & -d_b \\ 0 & 1 & 0 \\ 0 & 0 & 1 \end{bmatrix} \begin{bmatrix} X \\ Y \\ \theta \end{bmatrix}, \tag{4.13}$$
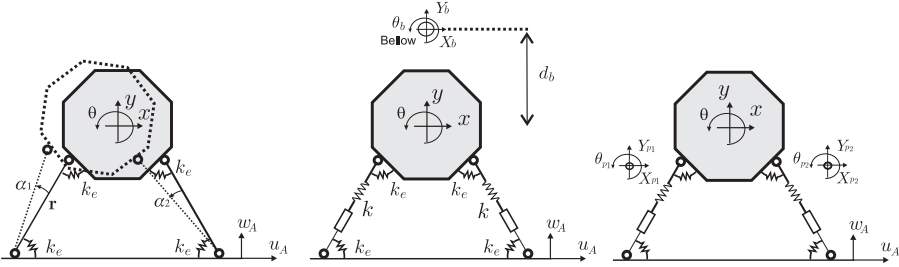
Figure 4.8: *The 4-bar mode consists of a displacement in the x-direction and a rotation in the θ-direction (left panel). One of the solutions is to use a bellows which is stiff in rotation but flexible in the x and y-direction (middle panel). Another solution is to use shear pins far away from the rotation point of the mode (right panel).*

where d_b is the distance of the center point of the bellow to the origin of the magnet. The potential energy equation, given in Eq. (4.7), is extended to:

$$V_b = V + \frac{1}{2}k_{bx}(x - d_b\theta)^2 + \frac{1}{2}k_{by}(y)^2 + \frac{1}{2}k_{br}\theta^2. \qquad (4.14)$$

Fig. 4.9 represents simulation results for the three modes of the system with 2 legs attached at $d_{x1} = -0.1$ m, $d_{x2} = 0.1$ m, $d_{y1,2} = 0$, $\beta_1 = -\beta_2 = 20^o$, for changing values of k_{br} and $d_b = 0.4$ m (left panel) and for changing values of d_b with $k_{br} = 500$ KNm/rad (right panel). A high rotation stiffness bellow was chosen based on the R+W Type BK1 [65]. The stiffness in x and y-direction was fixed to $k_{bx} = k_{by} = 900$ N/m.
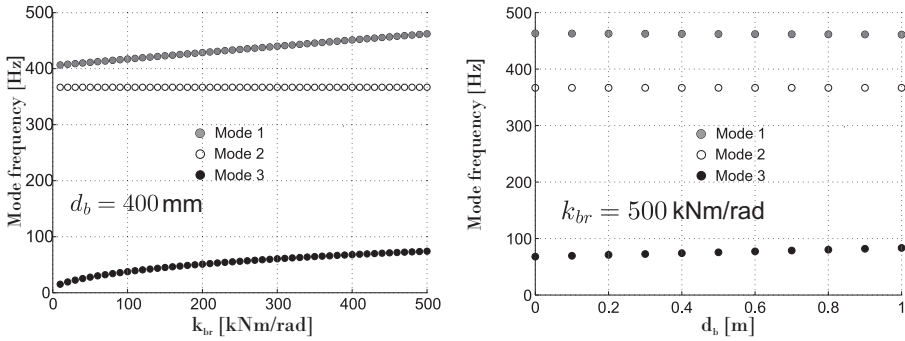
Figure 4.9: *The three modes of the system with 2 legs attached at $d_{x1} = -0.1$ m, $d_{x2} = 0.1$ m, $d_{y1,2} = 0$, $\beta_1 = -\beta_2 = 20^o$, for changing values of k_{br} and $d_b = 0.4$ m (left panel) and for changing values of d_b with $k_{br} = 500$ kNm/rad (right panel).*

Even with an almost unrealistic rotational stiffness of 500 kNm/rad, the '4-

bar' mode does not go higher than 80 Hz. Therefore the bellows does not provide a good solution.

B. Shear pins

To evaluate the possibilities of the shear pins (see Fig. 4.8 (right panel)), two pins will be used which are distributed symmetrically around the y-axis. The transfer matrix between the reference frame of pin i $(X_{pi}, Y_{pi}, \theta_{pi})$ and the magnet reference frame is given by:

$$\begin{bmatrix} X_{pi} \\ Y_{pi} \\ \theta_{pi} \end{bmatrix} = \begin{bmatrix} 1 & 0 & -d_{pyi} \\ 0 & 1 & d_{pxi} \\ 0 & 0 & 1 \end{bmatrix} \begin{bmatrix} X \\ Y \\ \theta \end{bmatrix}. \tag{4.15}$$

The variables d_{pxi} and d_{pyi} represent the distance of pin i to the center of the magnet in x and y direction respectively. The potential energy of the pins is then added to the potential energy of the system with the two legs given in Eq. (4.7):

$$V_p = V + \sum_{i=1}^{N} \frac{1}{2} k_{pxi}(x - d_{yi}\theta)^2 + \frac{1}{2} k_{pyi}(y + d_{xi}\theta)^2 + \frac{1}{2} k_{pri}\theta^2. \tag{4.16}$$

Simulation results of the change of the first mode in relation to $d_{px1} = -d_{px2}$ and $d_{py1} = d_{py2}$ are displayed in Fig. 4.10. A surface plot is shown in the left panel and its contour plot on the right. The origin of the plot coincides with the centre of the magnet.
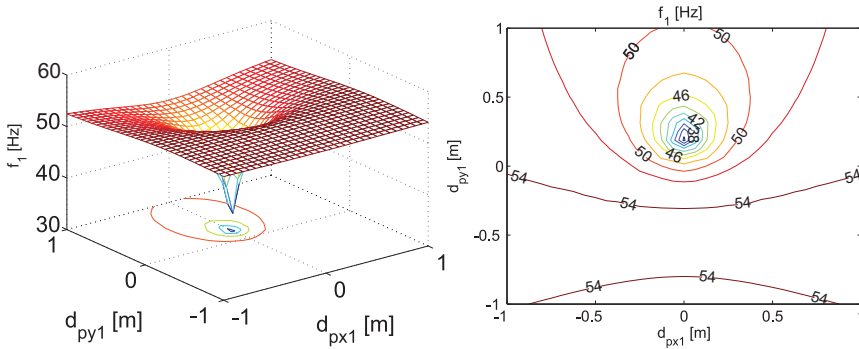
Figure 4.10: *A 3D representation of the location of the first mode for $d_{px1} = -d_{px2}$ and $d_{py1} = d_{py2}$ (left) and its contour plot (right).*

The rotation point of the mode is clearly visible. If the pins are located in this point, then the first mode drops dramatically due to the limited rotational stiffness of the pins. Further, the farther away the pins the higher the mode

becomes until they surpass the legs at which point the mode shape changes and the mode is lowered again. Additionally the location of the pins will be limited by the space available in the accelerator design.

Additionally there will be a roll component when a movement in the x direction is made as they are kinematically coupled. From simulations it was determined that the roll will be 5.15 μrad/μm of movement [66]. Beam simulations have been performed and it was found that the roll of the main beam quadrupole should not be more than 100 μrad. The maximum roll will thus never be reached within the 5 μm range. A test is discussed in section 6.2.4 to confirm the limited parasitic roll.

4.1.5 Summary

In this chapter several solutions to the 2D movement of the magnet were researched. From the number of legs to solutions for the low '4-bar' mode.
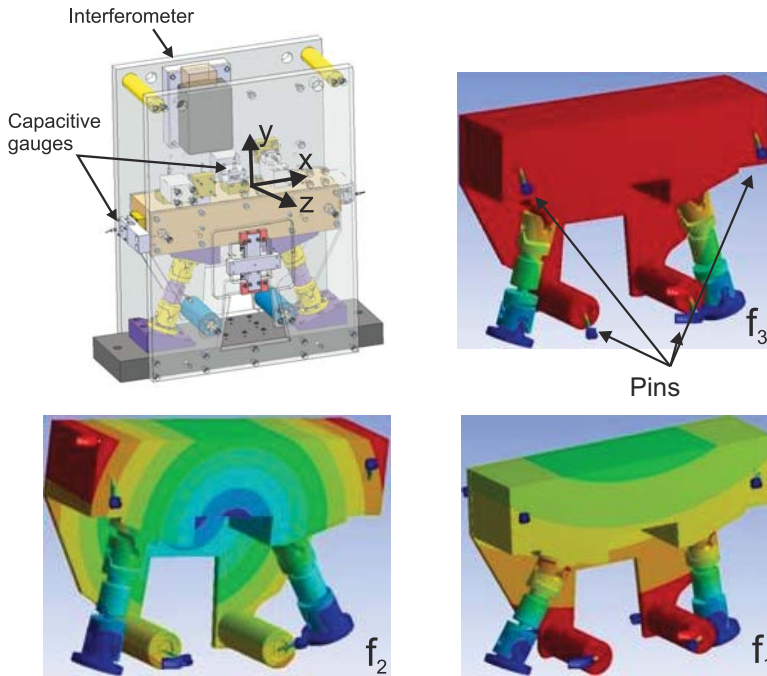
Figure 4.11: *The design of the proposed xy-guide prototype (top left panel) and the mode shapes for the three frequencies found by ANSYS Workbench.*

A summary is given in Table 4.5.

It was concluded that the best option is 2 inclined legs with pins. A prototype for the xy-guide with 8 pins was built (see Fig. 4.11 (top left panel)).

| | 2 legs hor.vert. | 3 legs hor.vert. | 2 legs 70 deg | |
			bellow	pins
Modes	- -	++	-	+
Actuator safety	- -	- -	+	+
Longitudinal compliance	-	-	-	+

Table 4.5: *Summary of the concepts against the requirements (-) negative (+) positive.*

The different variables for the xy-guide are given in Table 4.6.

Variable	Value	Variable	Value
k_{px}	3.22 N/μ m	b1	20°
k_{py}	3.22 N/μ m	b2	-20°
k_{pr}	80 Nm/rad	$L_{1,2}$	0.115 m
I	0.735 kgm^2	M	50.5 kg
k_e	223 N/m	k	114.29 N/μm
d_{px1}	0.19 m	d_{py3}	-0.225 m
d_{px2}	-0.19 m	d_{py4}	-0.225 m
d_{px3}	0.085 m	d_{x1}	-0.122 m
d_{px4}	-0.085 m	d_{x2}	0.122 m
d_{py1}	0 m	d_{y1}	0.1 m
d_{py2}	0 m	d_{y2}	0.1 m

Table 4.6: *Overview of the variables used for the concept design of the mechanical system with shear pins.*

The resulting modes for the xy-guide calculated with the equations derived in this chapter and in ANSYS Workbench are given in Table 4.7.

	Mode ANSYS [Hz]	Mode analytical [Hz]
f_1	145	153
f_2	303	310
f_3	336	339

Table 4.7: *The different modes found in ANSYS work bench and in an analytical way. The mode shapes are shown in Fig. 4.11.*

Results from both ANSYS and analytical calculations are in good agreement and there is no mode in the bandwidth under 100 Hz. The mode shapes are shown in Fig. 4.11.

The next section will give a concept of how the model will function in 3D.

4.2 Mechanical Design concepts 3D

The smallest magnet (Type 1) is 0.40 metre long and has a mass m_{tot} of 100 kg. According to first modal calculations the flexural mode will lie between 100 and 200 Hz. The final concept for the Type 1 magnet has 2 pairs of legs and hence two sets of xy-guides connected with a flexible magnet, as is shown in Fig. 4.12.
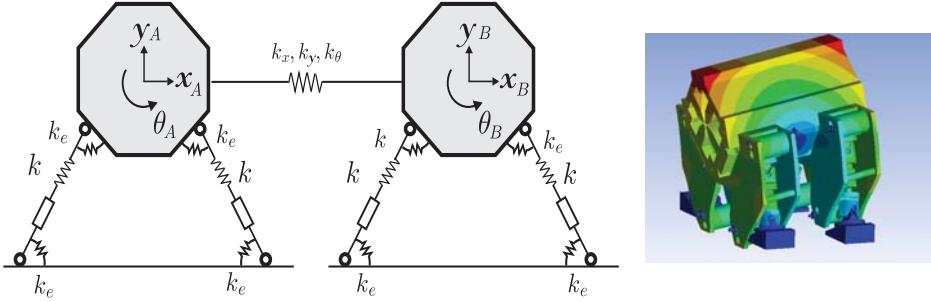
Figure 4.12: *Lumped mass model of a slender electromagnet on the four legged stabilisation system.*

The equation of motions can be written as:

$$M\ddot{\mathbf{x}} + C\dot{\mathbf{x}} + K\mathbf{x} = \mathbf{F},\qquad(4.17)$$

with

$$\mathbf{x} = \begin{bmatrix} x_A \\ y_A \\ \theta_A \\ x_B \\ y_B \\ \theta_B \end{bmatrix},\qquad(4.18)$$

and the mass matrix:

$$M = \begin{bmatrix} m & 0 & 0 & 0 & 0 & 0 \\ 0 & m & 0 & 0 & 0 & 0 \\ 0 & 0 & I_n & 0 & 0 & 0 \\ 0 & 0 & 0 & m & 0 & 0 \\ 0 & 0 & 0 & 0 & m & 0 \\ 0 & 0 & 0 & 0 & 0 & I_n \end{bmatrix}.\qquad(4.19)$$

The mass $m = 50$ kg and I_n is the moment of inertia around the longitudinal axis of the magnet used in the 2D section.

The stiffness matrix of each section is calculated as was done in section 4.1.4. Two of these stiffness matrices are added into the overall stiffness matrix of the

system $K_l = \mathrm{diag}(K, K)$. The flexibility of the magnet itself is modelled by adding a stiffness in x and y-direction $k_x = k_y = k_b$ and a torsional stiffness k_t in the connection points between the three sections. The flexural stiffness matrix K_f then becomes:

$$K_f = \begin{bmatrix} k_b & 0 & 0 & -k_b & 0 & 0 \\ 0 & k_b & 0 & 0 & -k_b & 0 \\ 0 & 0 & k_t & 0 & 0 & -k_t \\ -k_b & 0 & 0 & k_b & 0 & 0 \\ 0 & -k_b & 0 & 0 & k_b & 0 \\ 0 & 0 & -k_t & 0 & 0 & k_t \end{bmatrix}. \tag{4.20}$$

The total stiffness matrix and damping matrix can then be calculated with $K = K_l + K_f$ and C was calculated through modal damping in order to give all modes a damping ratio of 1%. The state space approach of the system is then given by:

$$\dot{\mathbf{x}} = A\mathbf{x} + B\mathbf{u} + E\mathbf{w},$$
$$\mathbf{y} = C_s\mathbf{x} + D\mathbf{u} + G\mathbf{w}, \tag{4.21}$$

with

$$A = \begin{bmatrix} Z_{6\times6} & I_{6\times6}, \\ -K/M & -C/M \end{bmatrix}$$

, where $I_{6\times6}$ is the identity matrix of dimension 6 and $Z_{6\times6}$ it the null matrix of dimension 6.

The matrix B recalculates the forces in the direction of the legs f^T to the forces and torsion of the to be controlled mass $[F^T]$. According to Ref. [18]:

$$f\delta q = f J \delta X = F \delta X, \tag{4.22}$$

where δq represents the elongations of the legs, δX the movement of the mass and J the Jacobian relating the reference frames. Since the displacements and forces work in the same respective reference frames it follows that:

$$F = J^T f. \tag{4.23}$$

Therefore:

$$B = k \begin{bmatrix} J^T & Z_{3\times2} \\ Z_{3\times2} & J^T \end{bmatrix}, \tag{4.24}$$

and $\mathbf{u} = [q_{A1} q_{A2} q_{B1} q_{B2}]^T$. For the disturbances $\mathbf{w}$ things are slightly more complicated. The movement of the ground first has to be related to displacement
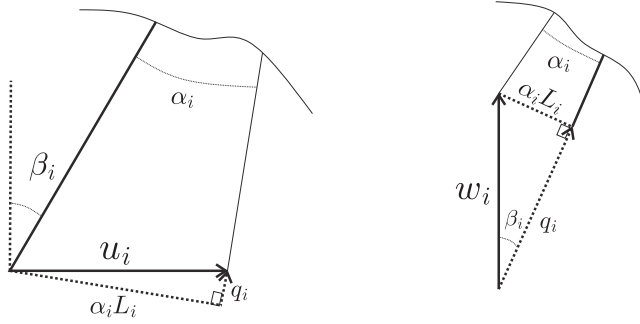
Figure 4.13: *The geometric relations between the ground motion and the leg reference frame for a horizontal motion (left panel) and vertical motion (right panel).*

in the legs and then recalculated to a force in the mass. The geometrical relations between a vertical (y) and horizontal (x) movement of the legs and the vertical and horizontal ground motion (w) and (u) are shown in Fig. 4.13.

This results in the relation:

$$\begin{bmatrix} q_i \\ \alpha_i \end{bmatrix} = \begin{bmatrix} \sin(\beta_i) & \cos(\beta_i) \\ \frac{-\cos(\beta_i)}{L_i} & \frac{\sin(\beta_i)}{Li} \end{bmatrix} \begin{bmatrix} u_i \\ w_i \end{bmatrix}, \tag{4.25}$$

or $q_i = J_{gi}w_i$. As these forces need to be recalculated to the force reference frame of the magnet, the resulting G matrix is given by:

$$G = \begin{bmatrix} BJ_{g1} & BJ_{g2} & Z_{3\times2} & Z_{3\times2} \\ Z_{3\times2} & Z_{3\times2} & BJ_{g1} & BJ_{g2} \end{bmatrix}. \tag{4.26}$$

The measured x and y positions for each section ($\mathbf{X}$) are given by the output matrices C and $D = [0]$.

All input signals signals are then calculated through $\mathbf{Q} = H\mathbf{X}$ with:

$$H = \begin{bmatrix} J_rH_c & Z_{2\times2} \\ Z_{2\times2} & J_rH_c \end{bmatrix}. \tag{4.27}$$

Where H_c is the controller set up including both vertical and lateral direction for seismometer control or geophone control and J_r is a subsection of the Jacobian matrix to recalculate the required forces from the reference frame of the magnet to the reference frame of the legs.

The resulting open (solid) and closed loop (dashed) transmissibilities for the geophone are given in Fig. 4.14.

All the transmissibilities show a stable transmission with the expected reductions. One thing to note is that the frequency of the internal joint mode was

Figure 4.14: *The transmissibility between vertical ground motion w of one foot to the magnet y for both sections (left two plots) and lateral ground motion u of one foot to the magnet x (right two panels) for when the geophone control is off (solid curve) and the control is on (dashed curve).*

assumed high (above 100 Hz) and not included in the model. The sensor and actuator were assumed collocated.

The same transmissibilities were calculated for the seismometer control and are shown in Fig. 4.15. Again a stable closed loop was achieved for all directions. This chapter has shown the step by step conception of the multi d.o.f. vibration isolation system. It has shown that two legs at an angle of 70 degrees with the ground is the safest option and that shear pins can be used to increase the lowest '4-bar' mode while adding longitudinal stiffness. The concept was further extrapolated and a full 3D design for a Type 1 magnet was simulated with both a geophone and seismometer control loop. The next step is to investigate the practicality of the control system as it will be used along a 48 km linear accelerator with a control room far away, and in an environment with hostile radiation, magnetic fields, *etc.*

The cross coupling between x_a and q_{B1}, q_{B2} is almost a factor 100 smaller, in the controlled bandwidth, than the coupling between x_a and q_{A1}, q_{A2}, showing that there is limited interference between the directions. To add additional ro-
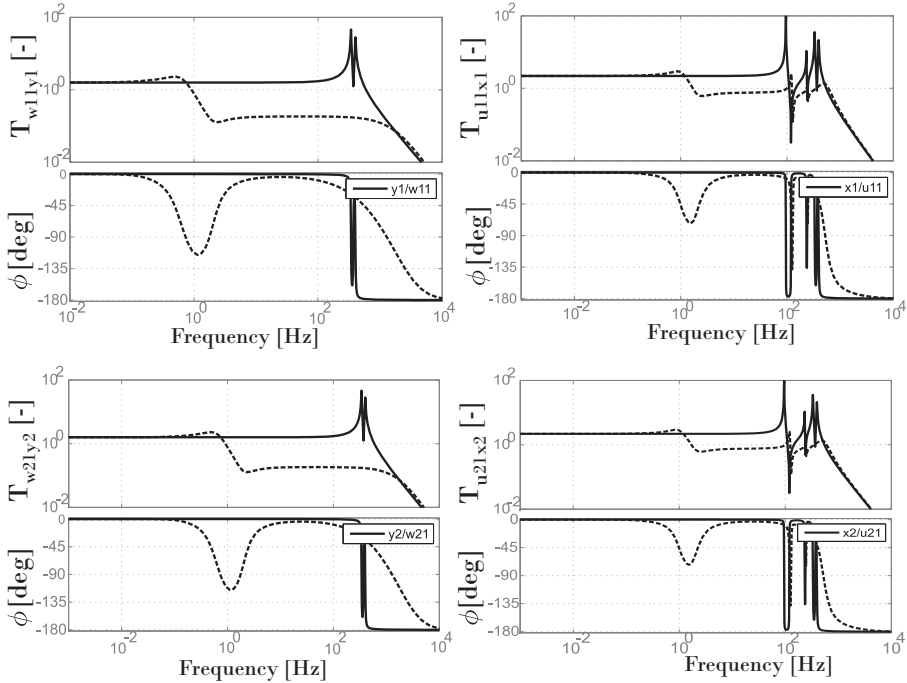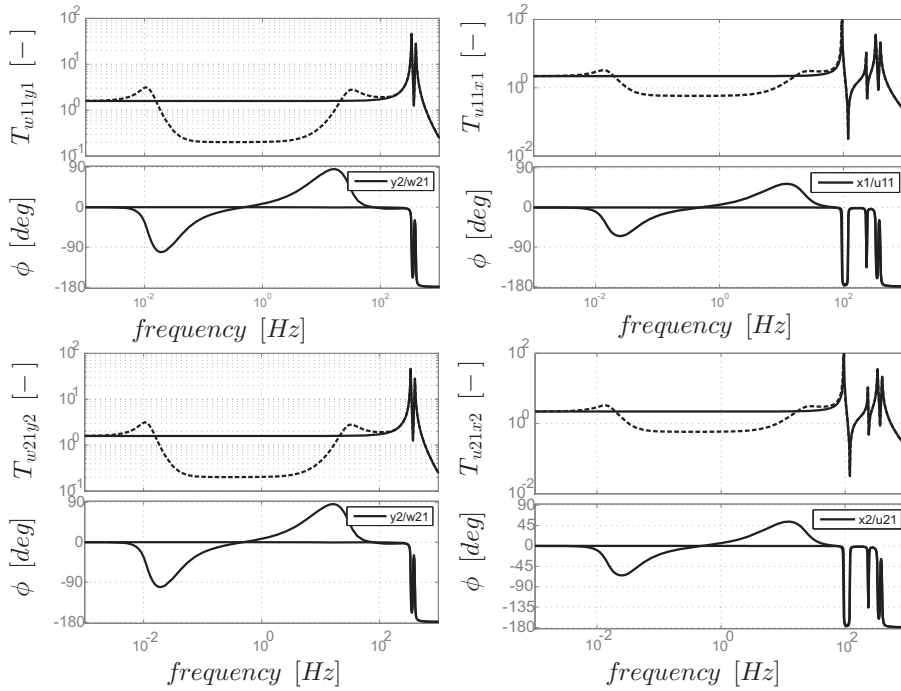
Figure 4.15: *The transmissibility between vertical ground motion w of one foot to the magnet y for both sections (left two plots) and lateral ground motion u of one foot to the magnet x (right two panels) for when the seismometer control is off (solid curve) and the control is on (dashed curve).*

bustness, the tests performed on the type 1 magnet will be performed with the vibration sensor in the middle of the Type 1 magnet, creating a global controller.

Chapter 5

Practical implementation of the controller

The control system for the stabilisation and positioning will have to be implemented in the systems of the full 48 km long CLIC accelerator. To understand the consequences of the location of the controller, a study is made on the effect of the delay on the control loops. Further there will be effects due to the implementation type of the filters. Therefore an analogue implementation is weighed against a digital implementation.

5.1 The location of the controller

For large scale accelerator projects, measurement data are often sent through an optical fibre cable. This cable causes a delay of 5 μs/km [67]. This delay is modelled in the Laplace domain by [19]:

$$H_d(s) = e^{-T_d s}. \tag{5.1}$$

The delay induces an increasing phase drop with increasing frequency. As the natural frequency of the vibration isolation system is quite high (≈ 240 Hz), small delays can already be problematic.

Adding the exponential transfer function to the simulations for the control loop does not allow to calculate the poles easily. Therefore a second order approximation, called the Pade approximation, is used to calculate the root locus [19]:

$$H_d(s) = e^{-T_d s} \cong \frac{1 - T_d s/2 + (T_d s)^2/12}{1 + T_d s/2 + (T_d s)^2/12}. \tag{5.2}$$

Fig. 5.1 compares the transfer function of the real delay with the approximation.

The phase drop of the real delay and of the approximation are very similar up to a phase drop of 135 degrees. The root locus of the approximation for
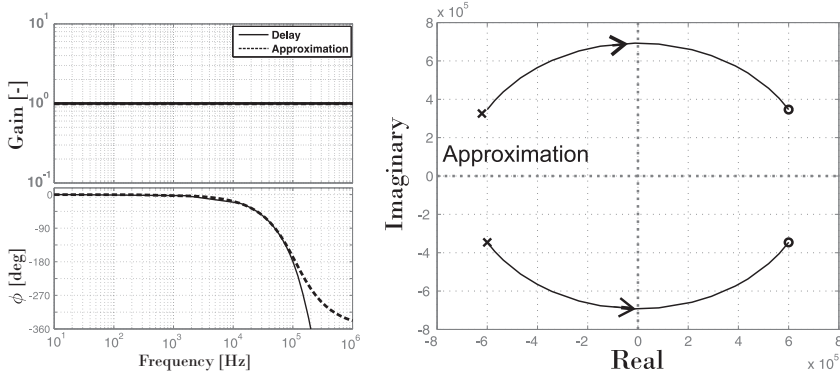
Figure 5.1: *Comparison of a delay of 5 μs with its second order approximation given by Ref. [19] (left panel). The root locus of the approximation for given value of T_d (right panel).*

changing values of T_d is displayed in Fig. 5.1 (right panel). The poles of the delay approximation are given by:

$$p_{1,2} = \frac{-3 \pm \sqrt{3}i}{T_d},\tag{5.3}$$

and the zeros are given by:

$$z_{1,2} = \frac{3 \pm \sqrt{3}i}{T_d}.\tag{5.4}$$

Both zeros are in the right half plane. This causes the system to become unstable, for some value of the gain, unless counter measures are taken.

The gain margin is set out against the delay time for the seismometer vibration control in Fig. 5.2 (left panel).

The controller will become unstable with a delay greater than 1 ms. However, Fig. 5.2 (right panel) shows that the performance of the stabilisation system decreases well before that, specifically near the cross-over point at higher frequency as the gain margin decreases dramatically.

The geophone configuration will have even greater problems with delay as the bandwidth of the control loop is much larger than the one of the seismometer (1 kHz vs 100 Hz). This is shown in Fig. 5.3.

The controller already becomes unstable with a delay as low as 0.13 ms.

This proves that for both controllers, the distance of the control infrastructure should be kept to the order of metres. Not kilometres as it would be if all control would be done with a single far-away control centre.
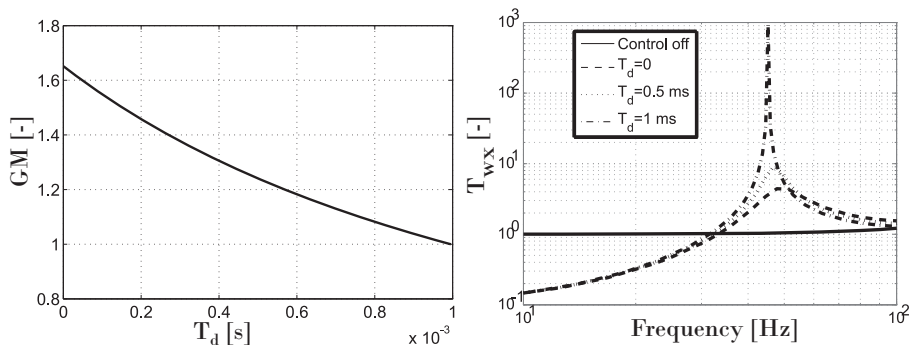
Figure 5.2: *The gain margin of the controller with the seismometer against delay time (left panel). The effect on the transmissibility between the ground w and the quadrupole x, (T_{wx}) (right panel).*
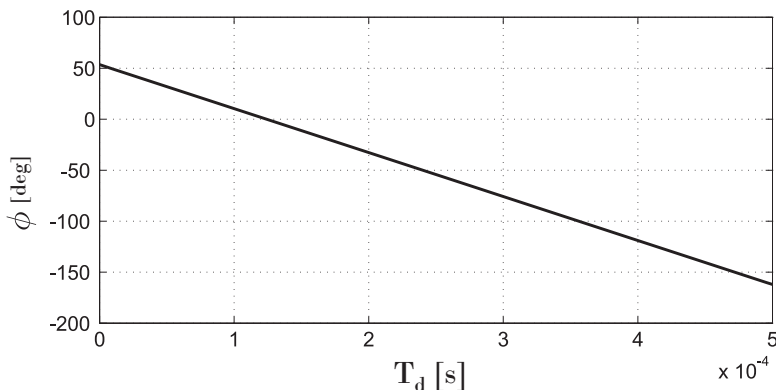
Figure 5.3: *The phase margin, towards the -180 degree limit, of the controller with the geophone against delay time (T_d).*

5.2 Digital vs Analogue

The local controller can be both analogue or digital. An analogue system has a very small delay but almost no flexibility in terms of composition of the control filters and gains. A digital discrete system is very flexible but adds additional stability limitations. For comparison, a discrete digital system was chosen that uses the zero-order hold method as sampling method. This method holds the same value of the sample until the next sample is taken. It multiplies the original system (contained in $G(s)$ and $H(s)$) with the transfer function of the zero-order hold method [68]:

$$G_0(s) = \frac{1 - e^{-sT}}{s}, \tag{5.5}$$

where T is the sampling period. Then this newly found transfer function

$(G^*(s),\ H^*(s))$ is transformed to the z-domain [68]:

$$G(z) = Z\{G^*(s)\}. \tag{5.6}$$

Due to the sampling of the system, aliasing can occur. To avoid this, the bandwidth of the controller should be lower than the Nyquist frequency which is half of the sampling frequency $f_s = 1/T$. From tests with a real time National Instruments PXI crate with a 24 bit card, it was found that a realistic sampling frequency of such a real time system is around 8,000 Hz, using the control loops designed in the previous sections. Additionally there will be a phase drop due to the delay caused by the zero order hold method. The resulting discrete root-locus diagrams (for more information see Ref. [19]) and Nichols plots are displayed in Fig. 5.4 for the geophone controller and in Fig. 5.5 for the seismometer controller.

Figure 5.4: *The discrete root-locus plot for the geophone solution with a discrete controller with a sampling frequency of 8 kHz (left panel); the Nichols diagram for the geophone solution with a discrete controller with a sampling time of 8 kHz (right panel).*

Since the bandwidth of the geophone solution is very large (around 1 kHz), the controller is rendered unstable. This can be seen in Fig. 5.4 (left panel) as the poles leave the unity circle of the discrete root-locus, rendering the control loop unstable. This is confirmed by the Nichols plot in Fig. 5.4 (right panel) as the curve passes above the cross-over point (-180,0). The bandwidth of the seismometer solution is much smaller and the effect on the stability is more limited (as is shown in Fig. 5.5 (left panel)). However the phase margin is very small for this control configuration as is proven in the Nichols plot represented in Fig. 5.5 (right panel).
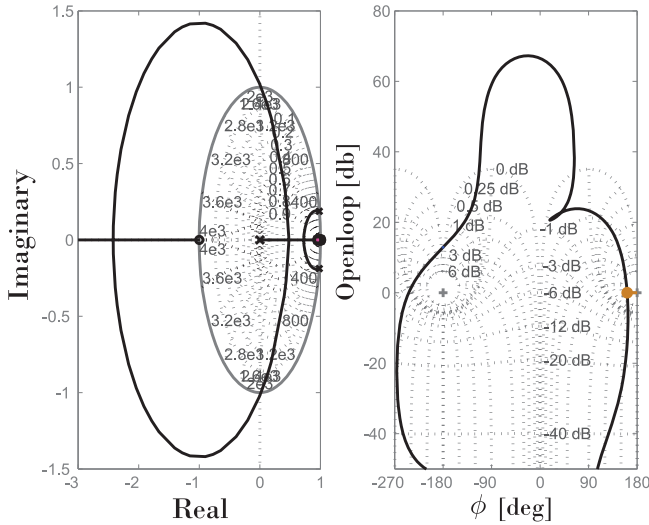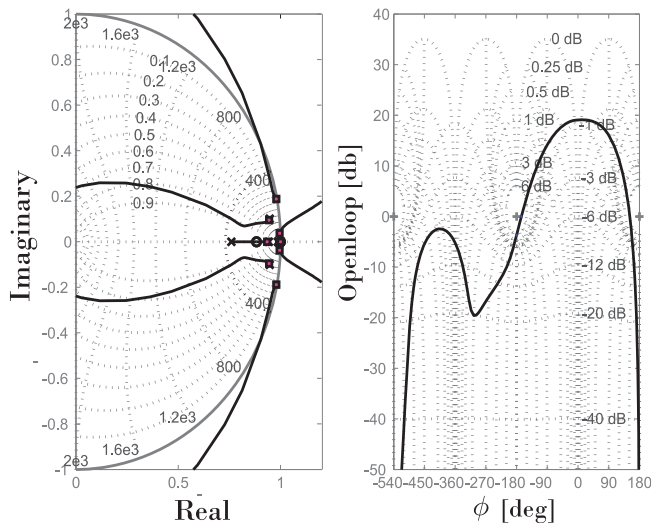
Figure 5.5: *The discrete root-locus plot for the seismometer solution with a discrete controller with a sampling frequency of 8 kHz(left panel); The Nichols diagram for the seismometer solution with a discrete controller with a sampling time of 8 kHz (right panel).*

An analogue approach does not have this phase drop as there is no digitization process. Additionally, the components of an analogue circuit are much less sensitive to radiation in terms of single event upsets [67]. However a purely analogue circuit does not allow for any flexibility of the controller to adapt to new circumstances. Therefore it was decided to put small digital chips in order to control several components on the electronics board. This allows to control certain parameters (gain, pole and zero positions) while keeping the cross section, and thus the chance for single event upsets small. More information about the hybrid analogue/digital board can be found in Refs. [67, 69, 70].

5.3 Practical approach to analogue controller with digital potentiometers

To describe the full design of the hybrid control board designed by P. Fernandez Carmona would go too far for the present thesis. For further details on the type of amplifiers, configuration, *etc.*, please read Refs. [69, 70]. Only the three major components will be described.

5.3.1   The integrator

A seismometer and geophone measure absolute velocity. However the controller
uses a position feedback. Therefore an integrator is needed. A perfect analogue
integrator does not exist in reality. A low pass filter is used as an integrator above
its cut off frequency. The low pass filter consists of an operational amplifier with
a capacitance C and a resistance R_2 in the loop and an input resistance R_1 as is
displayed in Fig. 5.6 (left panel). The cut off frequency of the filter is given by:

$$\omega_c = \frac{1}{R_2 C},$$
(5.7)

in which R_2 is the resistance and C is the capacitance of the capacitor. Above
this frequency the transfer function has a drop off of:

$$d = \frac{1}{R_1 C},$$
(5.8)

as is shown in the schematic representation of the transfer function in Fig. 5.6
(right panel).
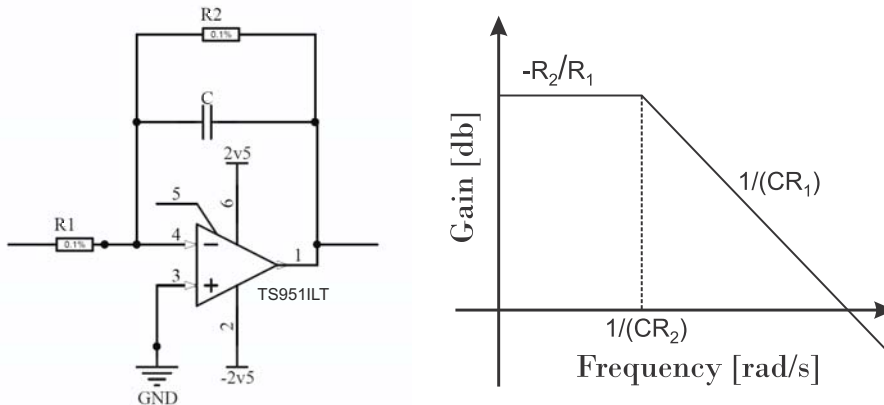
Figure 5.6: *A schematic representation of a low pass filter circuit (left panel)
and its corresponding transmissibility curve between the output and the input of
the circuit (right panel) .*

The value of $R2$ is made controllable through the use of digital potentiome-
ters in order to change corner frequency. The gain offset due to this will be
compensated by the control of the gain of the main gain amplifier.

5.3.2   The lead and lag components

The two other important control components are the lead and the lag filters. The
seismometer uses a lag compensator at high frequency to reduce the bandwidth of

the controller. The geophone uses a lag compensator at low frequency to increase the phase margin and a lead compensator near the resonance to increase the phase margin and to add localized damping. A simplified schematic for a lead and a lag compensator in an analogue circuit is shown in Fig. 5.7.
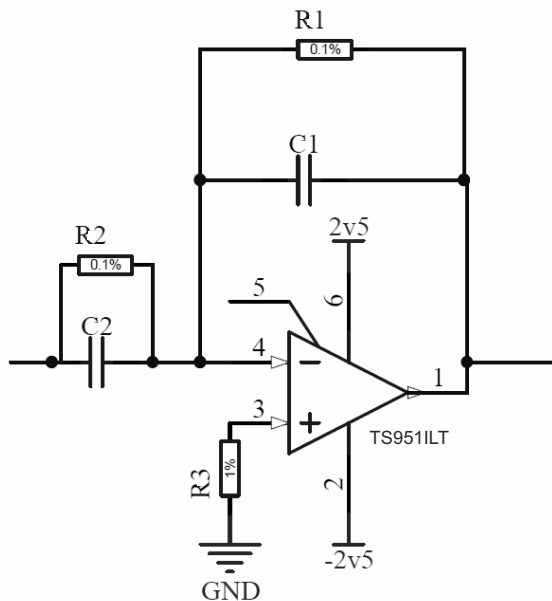
Figure 5.7: *A simplified schematic of a lead/lag circuit.*

The transfer function of this circuit in the Laplace domain is described by:

$$H_l = -\frac{\frac{1}{R_2} + sC_2}{\frac{1}{R_1} + sC_1}. \tag{5.9}$$

The circuit behaves as a lag filter if the location of the pole $\omega_1 = \frac{1}{R_1C_1}$ is lower than the location of the zero at $\omega_2 = \frac{1}{R_2C_2}$. If this is inverted, the circuit acts as a lead compensator. Digital potentiometers (AD5204BRZ10) are used for R_1 and R_2 to provide control over the position of the poles and zeros.

The next chapter will describe tests performed on various test benches using this circuit board.

Chapter 6

Experimental validation

This chapter presents experimental validations of the vibration isolation and nano positioning strategy presented in the previous chapters. Two test benches are considered. The first is a single degree of freedom, collocated, scaled test bench, dedicated to study the feasibility of low frequency vibration isolation. The second experimental set up is a two degrees of freedom compact mass, designed to address the additional difficulties of a heavy load and of combining the above mentioned tasks in both the vertical and horizontal directions.

6.1 Single degree of freedom scaled test bench

The single degree of freedom test bench was developed to have a simple collocated platform to perform basic vibration isolation and nano positioning tests and determine the feasibility. First the test bench will be described and then the experimental results are presented.

6.1.1 Description of the test bench

The single degree of freedom experimental set-up consists of a guided piezoelectric stack with stiffness $k_a = 24$ N/μm, clamped in a double membrane like structure with low stiffness in the vertical direction ($k = 0.714$ N/μm) to allow only a vertical motion. The model is shown in Fig. 6.1 (left panel). Two seismometers (Guralp T6) are used to measure the vibrations of the ground and on top of the test bench. The aim of the experiment is to stabilize a small mass laying on the top of the membrane, *i.e.* the seismometer ($M = 2.5$ kg) itself. A picture of the test bench is shown in Fig. 6.1 (right panel).

The governing equation of the system is:

$$M\ddot{x} + c(\dot{x} - \dot{w}) + k(x - w) + k_a(x - w) = -F + f, \qquad (6.1)$$
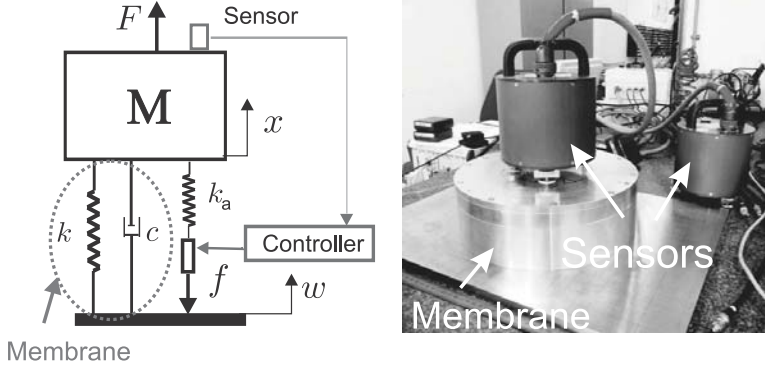
Figure 6.1: *A schematic representation (left panel) and a picture of the single d.o.f scaled test set-up (right panel).*

with $f = k_a\delta$ and $\delta = g_p H x = n d_{33} V$. The gain g_p is a proportional gain and the sensitivity of the seismometer is given by H and is shown in Fig. 3.5 (solid curve). The variable k_a is the stiffness of the piezoelectric stack actuator, V is the voltage applied to impose the deformation δ, and with n and d_{33} piezo-actuator parameters as was discussed in section 2.5. Neglecting the membrane stiffness k, Eq. 6.1 can be rewritten as:

$$\frac{X}{W} = \frac{G}{1 + g_p GH}, \tag{6.2}$$

with

$$G = \frac{k_a + cs}{Ms^2 + cs + k_a}. \tag{6.3}$$

The actuator is a PI P-753.21C piezo actuator with a maximum push capacity of 100 N and a stiffness $k_a = 24 N/\mu m$ [60]. The Guralp T6 seismometer, which is both the sensor and the payload mass of 2.5 kg, has six poles and no zeros.

A lag compensator is used to reduce the gain at high frequency without affecting the gain at low frequency as was suggested in section 3.1.4. This allows for the reduction in the cross-over frequency and increases the phase margin.

Fig. 6.2 shows the theoretical transmissibility T_{wx} when using the position feedback strategy. A Butterworth high pass filter at 0.5 Hz is introduced in the controller to remove the drift in the signals, and a lag at 30 Hz to improve the stability.
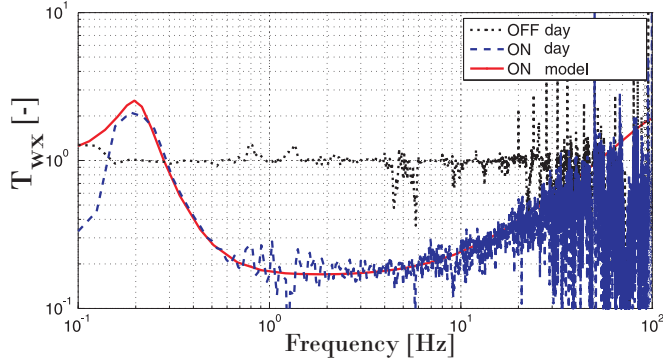
Figure 6.2: *Transfer function T_{wx} calculated (solid curve), and measured during the day when the controller is OFF (dotted curve) and ON (dashed curve) [63].*

The small overshoot at low frequency is due to the addition of the filter pushing the control loop closer to the stability margin.

6.1.2 Experimental results for seismometer feedback control

The membrane was put in a tunnel where the amplitude of the ground motion is similar to the values expected in the CLIC tunnel.

The theoretical transfer function T_{wx} is compared to the measured transfer function in Fig. 6.2, calculated from:

$$T_{wx}(f) = \frac{\Phi_{xw}(f)}{\Phi_{ww}(f)}, \qquad (6.4)$$

with Φ_{xw} the cross power spectrum between the ground and the membrane and Φ_{ww} the power spectral density of the ground. The transfer function measured when the controller is OFF is also shown.

Fig. 6.3 displays the corresponding integrated RMS displacement of the top geophone for two experiments, one performed during the day and one performed during the night. During the day, one sees that the feedback control has reduced σ_x from 4.7 nm to 1.4 nm at 1 Hz, *i.e.* a reduction by a factor 3.5. During the night, when the ground motion is even lower, σ_x is reduced from 1.8 nm to 1 nm at 1 Hz.
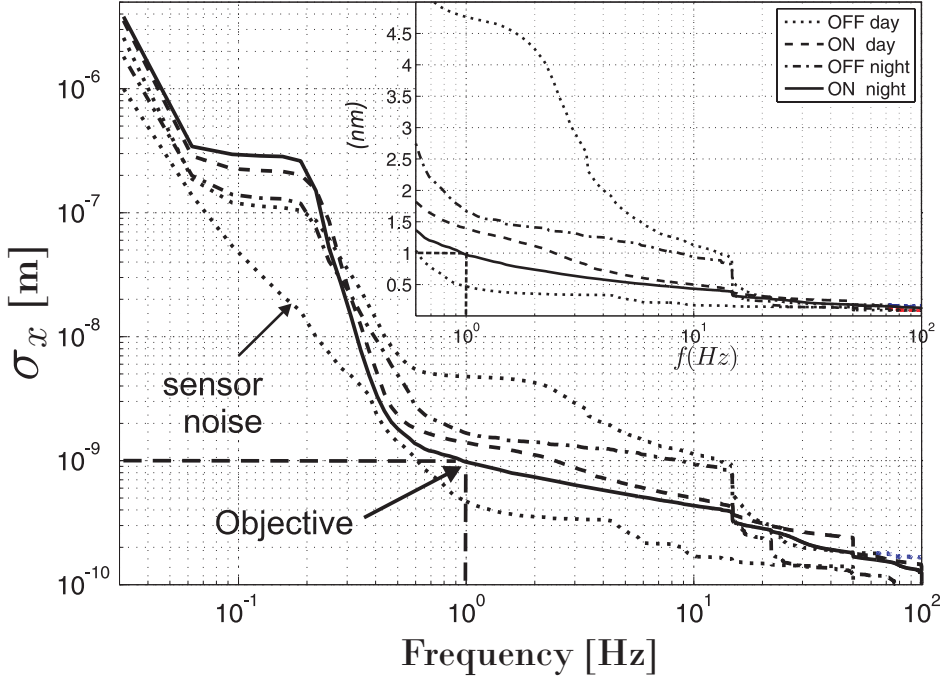
Figure 6.3: *Comparison of integrated RMS of the top displacement $\sigma_x(f)$ when the controller is ON and OFF, during the day and during the night.*

This test proves that it is possible to stabilize until the required 1.5 nm integrated RMS at 1 Hz, from a low vibration background.

6.1.3   Additional feed-forward control

As was shown in section 3.1.4, the feedback controller for the seismometer is limited by the stability of the control loop and not by sensor noise. The objectives have been achieved in terms of RMS value however the starting ground vibration has to be low. In order to improve the performance, a feed-forward controller is superimposed on the feedback controller.

A schematical block diagram of the combined feed-forward and feedback controller is presented in Fig. 6.4.

The transmissibility between the position of the quadrupole x and the ground w for the feed-forward can be written in the Laplace domain as:

$$T_{FF}(s) = G(s)(1 - F(s)), \tag{6.5}$$

where G(s)=$\frac{k}{Ms^2+k}$ and $F(s)$ includes a high pass filter at 0.5 Hz, a low pass filter at 100 Hz, the integrator and the frequency response of the Guralp seismometer.
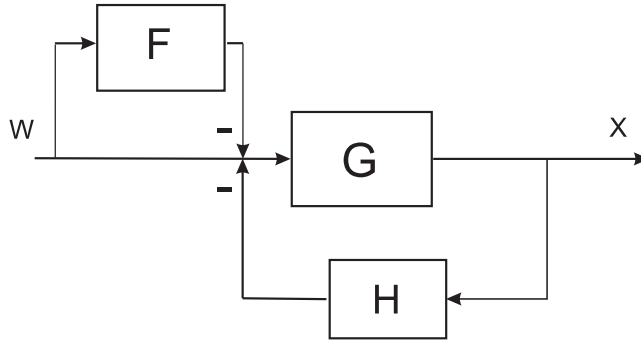
Figure 6.4: *Schematic block diagram of a one degree of freedom system (G) with a feedback loop (H) and a feed-forward controller (F).*

As was shown in chapter 2, the transmissibility between the ground w and the payload x for the feedback system can be written as:

$$T_{FB} = \frac{G(s)}{1 + G(s)H(s)},$$ (6.6)

with H including an integrator, a double lag at 30 Hz and a high pass filter at 0.5 Hz as was shown in previous simulations. Adding feed-forward and feedback together results in a transmissibility function between the ground and the membrane equal to:

$$T_{wx} = \frac{G(1 - F)}{1 + GH}.$$ (6.7)

The theoretical transfer fucntions, for feed-forward, feedback and the combination of the two are shown in Fig. 6.5.

Two types of transfer functions are used to compare the results. The first is the ratio between the cross power spectrum (Φ_{xw}) of the ground signal w and the quadrupole measurement x, and the PSD (Φ_{ww}) of the ground vibration w or

$$T_1 = \frac{\Phi_{xw}}{\Phi_{ww}}.$$ (6.8)

This shows the transfer between the input and the output signal incorporating the coherence drops between the signals, ignoring the measurement noise. To include the measurement noise, the square root of the ratio of the power spectral densities is used:

$$T_2 = \sqrt{\frac{\Phi_{xx}}{\Phi_{ww}}}.$$ (6.9)
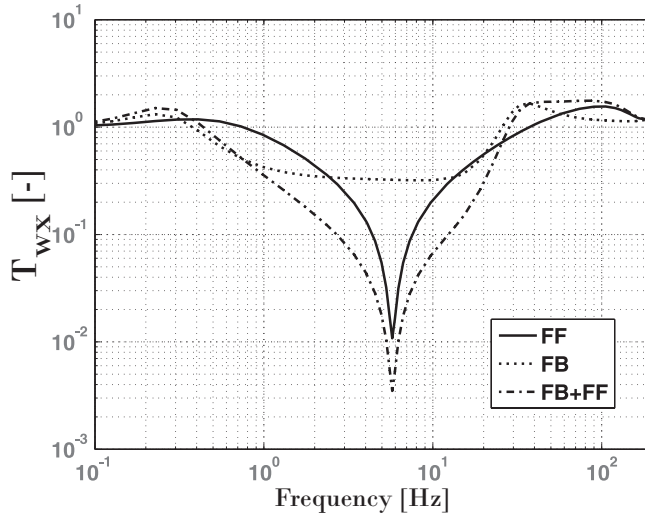
Figure 6.5: *Theoretical transfer functions for feed-forward, feedback and a combination of both.*

Feed-forward and feedback combination test results

The transfer function T_1 for the combined feed-forward and feedback controller is shown in Fig. 6.6.
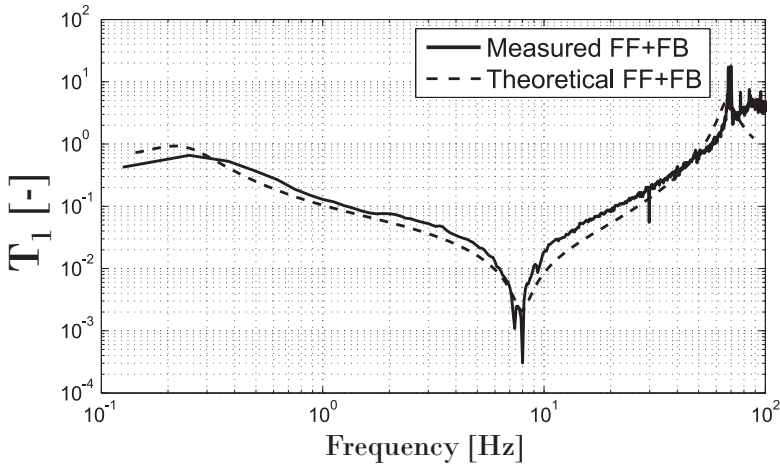
Figure 6.6: *The ratio between the cross power spectrum of the ground signal w and the quadrupole measurement and the autopower spectrum of the ground vibration w for the feed-forward combined with the feedback measurement and simulation.*

Now, the performance is however limited by the noise of the seismometer. Fig. 6.7 shows the PSD of expected ground vibrations, the theoretical achievable PSD calculated through the simulation and the theoretical noise curve of the seismometer.
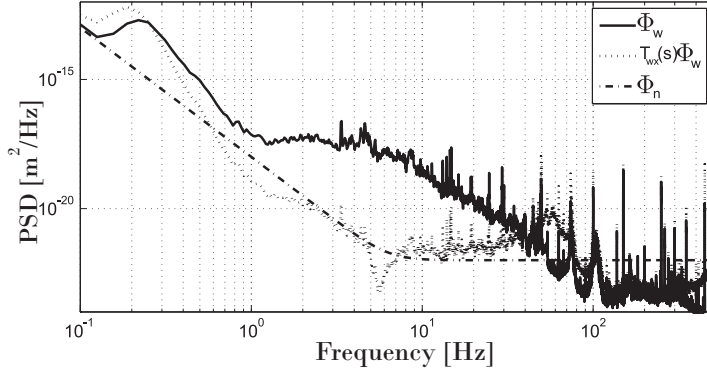
Figure 6.7: *The PSD of expected ground vibrations (Φ_{ww}), the theoretical achievable PSD calculated through the simulation ($\Phi_{xx} = T_{wx}\Phi_{ww}$), and the theoretical noise curve (Φ_{nn}) of the Guralp T6 seismometer for the combination of feed-forward and feedback.*
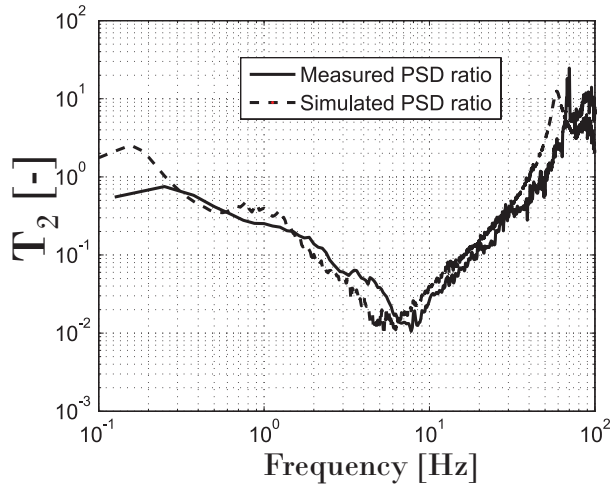
Figure 6.8: *The square root of the ratio of the power spectral densities for the measurement (solid curve) and the simulation of $\Phi_{xx} = T_{wx}\Phi_{ww} + \Phi_{nn}$ (dashed curve).*

The change in performance due to this noise limitation is shown in Fig. 6.8.

The higher the ground vibrations, the more the transfer function will resemble Fig. 6.6 and the better the performance.
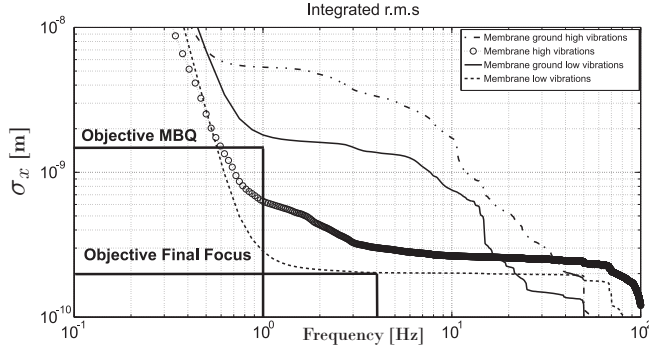
Figure 6.9: *The integrated RMS for vibrations of the ground and on top on the membrane using a feed-forward superimposed on a feedback loop with the seismometer.*

The main limitation for the combination of feed-forward and feedback is the noise of the Guralp seismometer. The performance increases in comparison to just feedback alone and also the overshoot is reduced at low frequency as the gain for the feedback can be relaxed. The performance in terms of integrated RMS is significantly better as can be seen in Fig. 6.9.

Vibrations in a low background of 1.8 nm integrated RMS at 1 Hz are reduced to only 0.2 nm integrated RMS. Vibrations at a higher background are reduced from 6 nm to 0.6 nm integrated RMS at 1 Hz. Adding a feed-forward controller provides a vibration isolation which can handle higher ground vibrations but will not help with vibrations induced on the magnet as was shown in section 2.3.2. These values are a great improvement over the previous attempts for vibration isolation of particle accelerators mentioned in section 2.4.3.

6.1.4   Positioning control

The nano-positioning capability of the membrane was tested with a square signal, using an amplitude of 10 nm and a frequency of 50 Hz equal to the repetition rate of CLIC. Fig. 6.10 shows that the actuator follows the request well as the frequency of the step function was much lower than the natural frequency $(f_n = \frac{1}{2\pi}\sqrt{\frac{k}{M}} = 490$ Hz$)$ of the system. By avoiding the resonance frequency, and using input shaping of the signal, no damping is needed and open loop control is a possibility. Alternatively, a dedicated positioning control loop can be designed, one of the possible future works after this thesis.
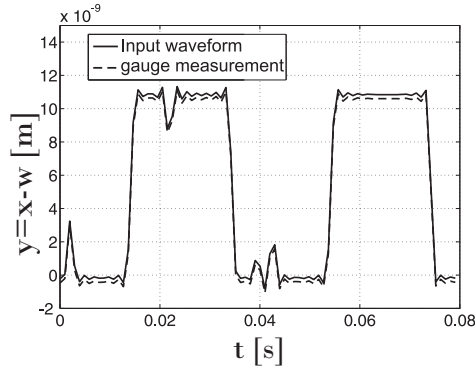
Figure 6.10: *Results of the nano-positioning experiment where the relative position $(y = x - w)$ of the membrane was measured with a capacitive gauge.*

6.2 Two degrees of freedom test bench

The two degrees of freedom test bench, nicknamed the xy-guide, consists of the mechanical concept presented in Fig. 4.11. A 3D drawing is shown in Fig. 6.11. First the vibration isolation tests will be explained.
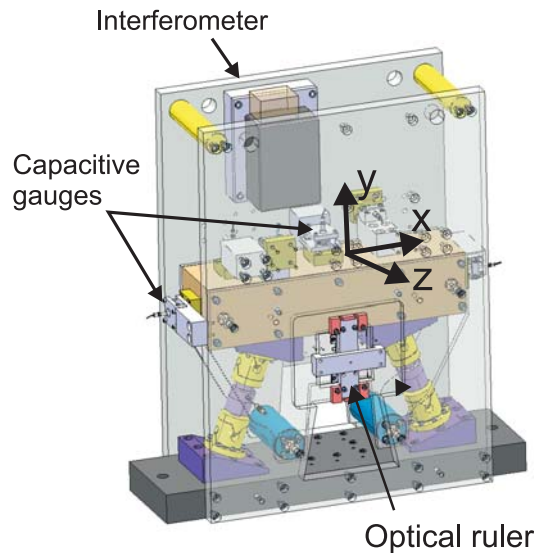
Figure 6.11: *The two degrees of freedom test bench with mounts for relative position measurement.*

In the second part, results of measurements of the precise movement of the test mass will be shown.

6.2.1   Vibration isolation results by using a seismometer

For the vibration isolation tests, a Guralp 6T seismometer was put on top and in the middle of the mass and one on the ground, between the two actuators. The same controller for the vibration isolation was used as for the membrane. This is possible as the ratio of mass to stiffness was chosen to remain the same. The performance between the membrane and the xy-guide is very similar for the seismometer control as is shown in Fig. 6.12, where the ratio of the PSD of the ground and mass is given.
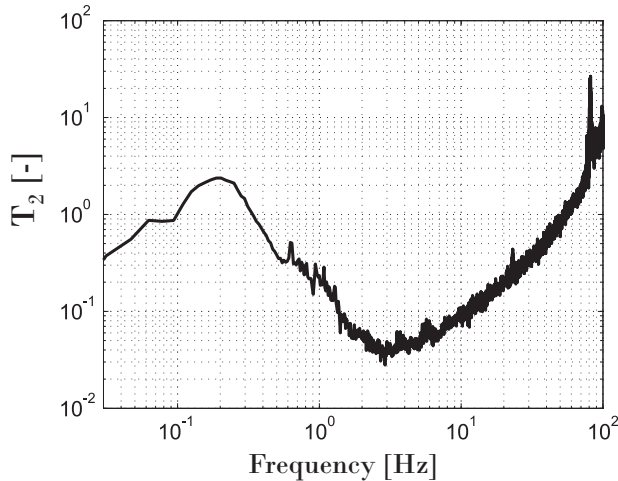
Figure 6.12: *Measured transmissibility between the ground w and the mass x on the xy-guide prototype in vertical direction.*

The result for the integrated RMS are given in Fig. 6.20. The vibrations were reduced from 4.5 nm to 0.5 nm integrated RMS at 1 Hz.

Horizontal vibration isolation was not yet performed with the hybrid board at the time of writing of this thesis. Simulations suggest similar performances for the feed-forward and a lower (maximum gain 5) stability limit for the feedback system well within the reach of the required 5 nm integrated RMS.

6.2.2   Vibration isolation results by using geophone feed-back control

The slew rate of the actuators prevented to perform stabilization tests with a geophone. The transmissibility between the ground and an L4C geophone on the top was measured in order to have the transfer function of the actuators (see Fig. 6.13). This transfer function was modelled and then multiplied by the slew rate of the actuators.
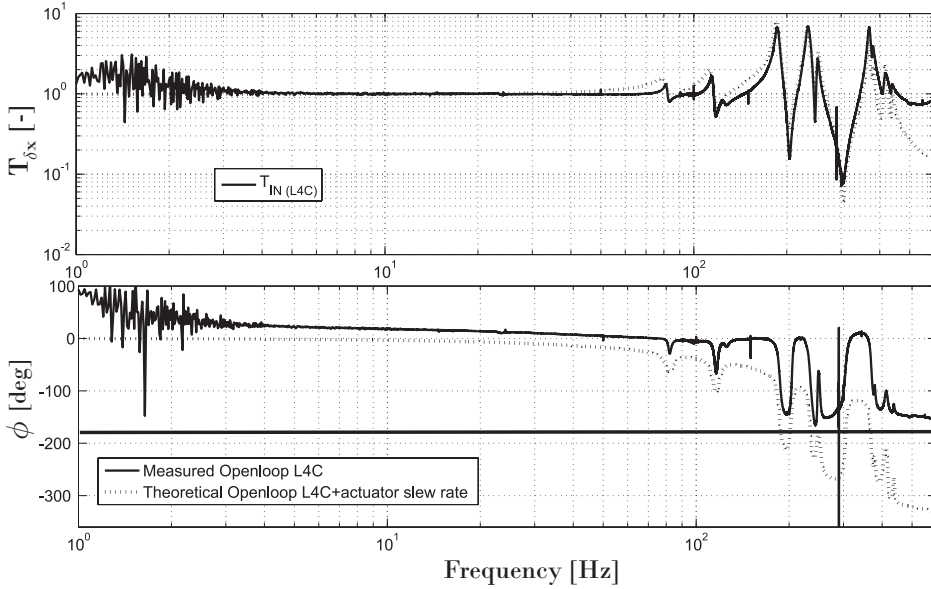
Figure 6.13: *The transfer function between the ground and the L4C geophone on top of the xy-guide and the theoretical approximation multiplied by the slew rate of the actuators.*

The slew rate of the actuators induces a phase drop which in turn causes the phase drop of one of the modes to cross the -180 degree stability line. This phase drop is more than 100 degrees and cannot be compensated by the lead. The geophone control will thus be possible only with an actuator with a high slew rate corner frequency > 5000 Hz.

6.2.3   Positioning results with xy-guide prototype

A. 2D motion of the xy-guide

To estimate the performance of the positioning system, a test was performed with the xy-guide. A position signal, filtered through an input shaping filter, was transmitted to the actuators, requesting a step every 5 ms. The position of the block was measured with capacitive gauges in both the vertical y and the lateral x direction. The temporal result is shown in Fig. 6.14.
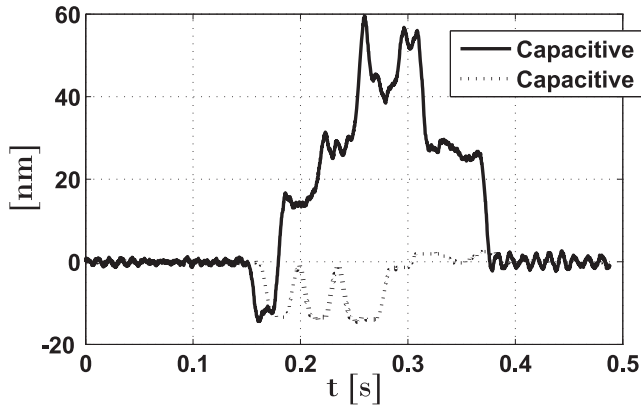
Figure 6.14: *The temporal displacement in x and y direction as measured by the capacitive gauges on the xy-guide mass.*

Combining the two temporal measurement results in an 2D plot of the position of the middle of the mass (see Fig. 6.15).
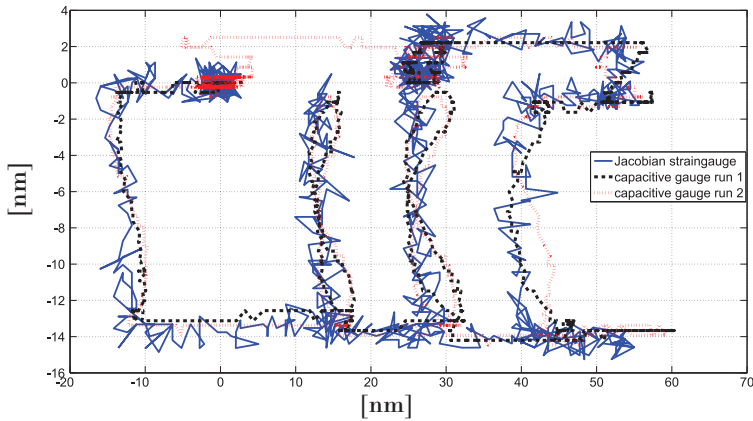
Figure 6.15: *The combined displacement in x and y direction as measured by the capacitive gauges on the block.*

The measurement of strain gauges in the actuator legs was recalculated in the x and y direction for comparison. It has two runs measured with the capacitive gauges superimposed. The signal for both the strain and capacitive gauges is noisy. The two curves overlap quite well but it is hard to say if the positioning requirements are reached. In order to determine if the positioning requirements can be reached, another test was performed. A SIOS 3 beam interferometer was added to the structure to measure the movement of the block in the vertical direction. Additionally a Heidenhain optical ruler was incorporated to compare the measurement results. The temporal position of the block in vertical direction,

for the different measurement devices, is shown in Fig. 6.16. These results were presented in Ref. [66].
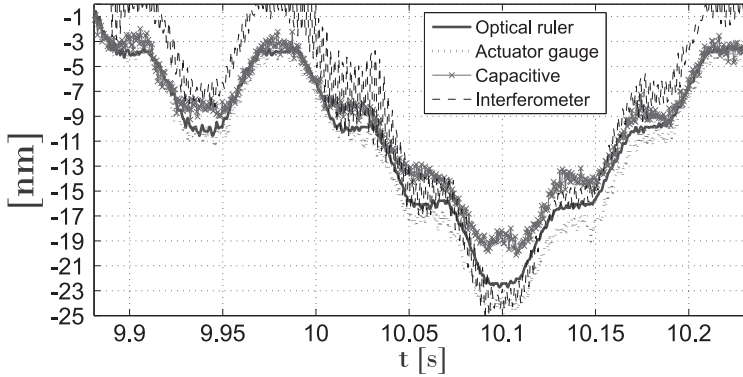
Figure 6.16: *The temporal displacement in y direction as measured by the capacitive gauges, the optical ruler, the actuator strain gauges recalculated in y direction and the SIOS interferometer.*

From this test, it is clear that the optical ruler has the best resolution in this set-up compared to the other sensors. The measurement also shows that the repeatability or precision of the x-y prototype is better than the 1 nm required for the system. The capacitive gauges had a gain problem due to the sensitivity to mounting tolerances. The precision and accuracy of the three-beam interferometer was compromised by drifts due to air-flow. A main drawback for the long-term accuracy are possible drifts of references: voltages for capacitive and actuator gauges and wavelength for the interferometer (periodic re-calibration is imperative). The references used for the optical rulers are edges etched on a glass ruler with small thermal expansion coefficient. However, if the counting of the edges is interrupted during displacements, *e.g.* during a power cut, the absolute position is also lost. This can be solved by using optical encoders that also measure a digital reference position etched on the ruler (hence no problem for reference drift). This and the fact that it is an optical system being capable of moving all electronics away from the magnetic fields, make the optical ruler a prime candidate to be used later in a dedicated positioning system. More information on the working principles of the optical ruler can be found in Ref. [71].

6.2.4 Estimation of the parasitic roll

Since there are only 2 legs for three degrees of freedom (x,y,θ), there will be a roll component when there is a repositioning in the x direction. Simulations predicted the roll to be 5.15 μrad/μm of movement [66]. The three beam interferometer

was used to determine the roll of the block while moving with an amplitude of 1.5 μm in the x direction. The resulting roll of the block is shown in Fig. 6.17.
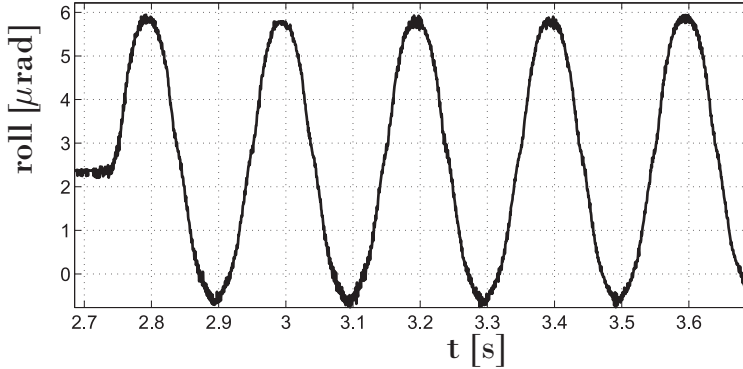
Figure 6.17: *The temporal roll around the z axis of the xy guide as measured by the three beam interferometer while the block is moving 1.5 μm in the x direction.*

For a 1.5 μm amplitude lateral motion, a roll of 3.3 μrad (amplitude) was measured or 2.2 μrad/μm for lateral motion. This is smaller than the calculated values in Ref. [66] and indicates that the limit specified by the beam dynamics (maximum 10 μrad/μm) can be met.

6.3   Measurement with an active Type 1 magnet

The next step is to test if the found solution with the seismometers would work in the magnetic field of a quardupole of 12 T/m and while the water cooling of the magnet is on. A Type 1 magnet was positioned on a passive support on one side and two active inclined legs on the other. The passive support consists of two sharp points, allowing rotation around an axis perpendicular to the beam axis. This way the magnet could move in the vertical direction while being guided in the lateral direction and blocking roll. A picture of the set up is shown in Fig. 6.18. The water flow through the coils was 1 l/min, above nominal.

Even with both the water cooling on and with active magnetic field, the performances stayed very similar to what was found before as is shown in Fig. 6.19.
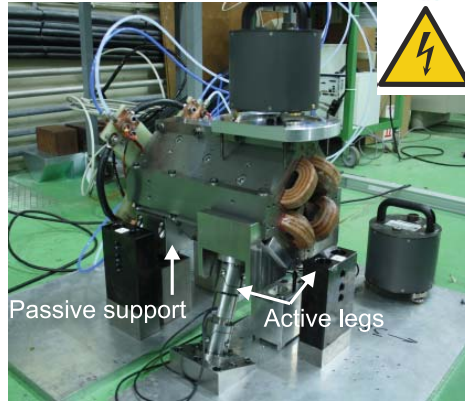
Figure 6.18: *A Type 1 quadrupole magnet for CLIC on two active inclined piezo-electric actuators and a passive support. The water cooling flow is highly turbulent and was flowing at a nominal 1 l/min and the magnet was powered to its nominal value.*
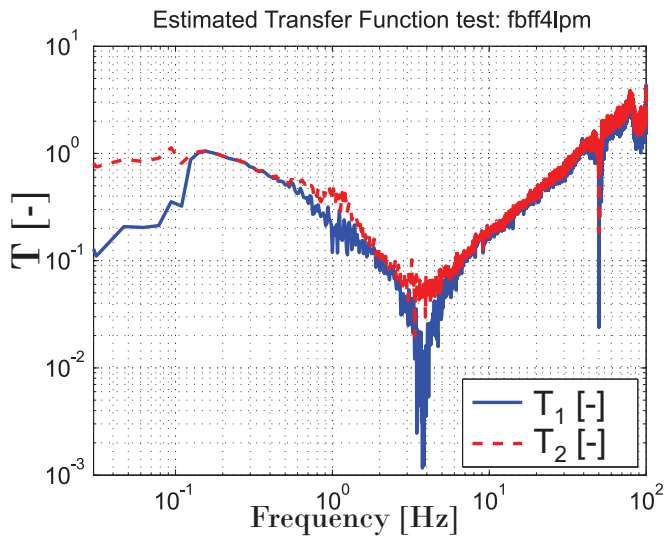
Figure 6.19: *The transmissibility T_1 and T_2 between the ground w and the top of the magnet x during an operational test with water cooling flowing at 1 l/min and a nominal magnetic field.*

The vibration levels were not very different from tests without water cooling due to the stiff actuators. The integrated RMS was reduced from 6 nm to 0.45 nm integrated RMS at 1 Hz.
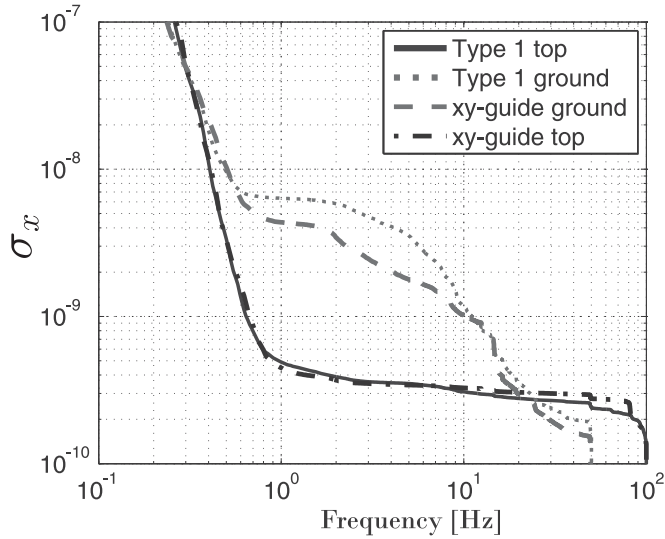
Figure 6.20: *The integrated RMS of the vibrations of the xy-guide and of the Type 1 magnet with water cooling and power on.*

The stray field of the quadrupole is actually small outside center of the magnet $(0.15 \times 10^{-4}$ T at 0 Hz [5]) and very stable. It does not influence the seismometer. The question remains for the kicker magnets which might be attached to the quadrupoles. These have a field between 10^{-3} to 4×10^{-4} T and might have a bigger impact. Tests will be performed when one becomes available.

Chapter 7

Conclusions and Future work

7.1 Conclusion

The goal of this thesis was to conceive and demonstrate the feasibility of a vibration isolation system capable to reduce the motion of a quadrupole magnet, with mass from 100 to 400 kg to 1.5 nm integrated RMS vertically and 5 nm horizontally down to 1 Hz. Furthermore, the quadrupole should be capable of being repositioned every 20 ms with steps of 10 nm with a precision of $\pm$ 1 nm. This in an accelerator environment with stray magnetic fields, radiation, ventilation and water cooling in the magnet.

From literature it was learned that:

- Most vibration isolation is done with soft systems with a natural frequency of 2 to 20 Hz.

- The compliance (resistance to external forces) of the systems found in literature is not high enough to ensure stability of the magnet with all the external forces.

- A stiff system (f_n=200 Hz) was chosen by using piezo actuators in order to reach the required high levels of compliance.

- A position feedback, reducing the transfer function and the compliance in front of the natural frequency was chosen as it allowed for vibration isolation of a stiff system.

Two control loops were considered and compared and weighed against possible issues:

- A commercial seismometer was used in a feedback loop, excluding all natural frequencies out of the bandwidth.

- A feedback loop by using a geophone which included all resonances, but allowing for a wider vibration isolation bandwidth.

- It was shown that the flexural mode of the magnet and the mode from a flexible support under the stabilisation system did not render either control loops unstable.

- It was advised that all resonances should be higher than 100 Hz in order to have enough stability margin and to reduce the amount of integrated RMS ground motion growth due to amplification at the resonances.

- Having a flexible joint, required to protect the actuator from bending forces, removed the property of collocation between the actuator and sensor, rendering it unstable if the corresponding mode was in the bandwidth of the controller.

- This problem can be reduced by increasing the damping of the corresponding mode or by making sensor and actuator collocated again. This would require a redesign of existing sensors and goes beyond the scope of the present work. Therefore the most practical solution for the tests was the seismometer.

The best mechanical configuration was researched:

- First, the number and best position of the actuators on the magnet was calculated with respect to the 2 degrees of freedom required. This resulted in a configuration with two legs under an angle of 70 degrees from the ground. It was a compromise between stiffness, resolution, controllability, protection of the actuators against tensile forces, and the cost of additional legs.

- Shear pins were added to provide guidance in the plane transversal to the beam, increase the '4-bar' mode and provide longitudinal stiffness.

- Parasitic roll, caused by having 2 legs for 3 degrees of freedom was found to be only 5.5 μrad/μm lateral movement. This was well within the specified 100 μrad maximum roll for the main beam quadrupoles for the full 10 μm range of the horizontal motion.

Practical implementation questions were answered:

- Simulations showed that the controller should be located near the magnet instead of kilometres away at the control centre for both the geophone and seismometer controller. The delays would render the control loops unstable.

- A hybrid analogue digital controller was developed in order to limit the delay in the control loop by using analogue components. Digital potentiometers allow the change of certain resistors in order to change the gains, the poles and the zeros of the control loops.

Validation tests were performed.

A single degree of freedom test bench was used to make a first evaluation of the seismometer control loop.

- The feedback control worked as expected and a feed-forward control loop was added to improve performances. This allowed to reduce the vibration level on the set up from 6 nm to 0.6 nm integrated RMS at 1 Hz, well under the requirements.

- Positioning tests showed the capability to perform positioning in the nanometre range.

A prototype mechanical system called the xy-guide was built, representing a section of the vibration isolation system that will be used on the full magnets. Tests were performed.

- The vibrations were reduced from 4.5 nm to 0.5 nm integrated RMS at 1 Hz in the vertical direction.

- Positioning tests showed that a precision of $\pm$ 1 nm can be achieved and the best performing measuring technique was the optical ruler.

- A three beam interferometer was used to test the simulations done earlier for the parasitic roll. The measured roll was equal to 2.2 μrad/μm which is even lower than the predicted 5.5 μrad/μm by the simulations.

Further a test was performed with a Type 1 magnet supported by a passive support on one side and two active legs on the other.

- The controller using the seismometer was tested in an environment with stray magnetic fields of the quadrupole and water cooling vibrations. The performance of the isolation stayed the same with an integrated RMS going from 6 nm on the ground to 0.45 nm integrated RMS on the Type 1 magnet at 1 Hz.

- Further tests will have to be performed to determine the influence of the kicker magnets.

Tests with the geophone were not performed as the slew rate of the actuators rendered the control loop unstable. This may be solved by ordering a new set of actuators and amplifiers in order to have it changed to a higher frequency.

Through this thesis it has been proven that it is possible to perform vibration isolation to the level required while using a stiff support system, unheard of in previous research of vibration isolation for accelerators.

In the short to medium term future, tests using the seismometer control loop are planned on the xy-guide in the horizontal direction and in vertical and horizontal directions on the prototypes of the Type 1 and Type 4 magnet vibration isolation systems. Further, a positioning control loop with a relative measurement will be implemented to avoid drift at low frequencies (< 1 Hz) or to be used as a dedicated position control system for non stabilized magnets. An interface between the control room and the stabilisation controller is being designed for online adjustments and monitoring.

Two Ph.D. students are continuing the work of this thesis through the European particle accelerator components metrology and alignment to the nanometre scale (PACMAN) project at CERN. The first research project is focussed on the possible implementation of long range actuators with high precision to combine the pre-alignment stage with the stabilization stage. This would eliminate additional resonances and would not require interrupting the beam for realignment. A second project is aiming to develop a dedicated sensor in order to reduce the effect of the radiation on the sensor and allow collocated control.

Due to the trend of smaller and smaller beam sizes, this research could have implementations in the accelerator world outside of CLIC. These advances in the control of stiff systems could also have applications in industry, for example in the production of microchips and nano-tubes and for vibration control in large telescopes *etc.*

Bibliography

[1] S. Redaelli, "Stabilization of nanometre-size particle beams in the final fo-
cus system of the Compact LInear Collider (CLIC)," Ph.D. dissertation,
CERN/University of Lausanne (CH), High Energy Physics Institute (IPHE),
2003.

[2] O. Brunig, P. Collier, P. Lebrun, S. Myers, R. Ostojic, J. Poole, and P. Proud-
lock, "LHC Design report vol. I: The LHC main ring," CERN, Tech. Rep.,
2004.

[3] Y. Renier, "Implementation and validation of the linear collider final focus
prototype : ATF2 at KEK (Japan)," Ph.D. dissertation, Université Paris XI
Orsay, 2010.

[4] B. Barish, *Introduction to the ILC: Lecture I2*, Fifth International Accelera-
tor School for Linear Colliders, Villars, France, 2010.

[5] M. Aicheler, P. Burrows, M. Draper, T. Garvey, P. Lebrun, K. Peach,
N. Phinney, H. Schmickler, D. Schulte, and N. Toge, "A multi-TeV linear
collider based on CLIC technology: CLIC Conceptual Design Report,"
CERN, Tech. Rep. CERN-2012-007, October 2012. [Online]. Available:
http://project-clic-cdr.web.cern.ch/project-clic-cdr/CDR_Volume1.pdf

[6] K. Artoos, O. Capatina, M. Guichard, C. Hauviller, and F. Lackner, "En
route vers la nano stabilisation de CLIC: Faisceau principal et focalisation
finale," European Organization for Nuclear Research (CERN), Tech. Rep.,
2008.

[7] D. Schroeder, "Beamstrahlung and QED backgrounds at future linear col-
liders," Ph.D. dissertation, Stanford University, 1990.

[8] S. Baird, *Accelerators for pedestrians*. CERN-PS division, 1997.

[9] D. Schulte, *Dynamic Imperfections*, Fifth International Accelerator School for Linear Colliders, Villars, France, 2010.

[10] J. Pfingstner, "Mitigation of ground motion effects via feedback systems in the Compact LInearnear Collider," Ph.D. dissertation, Vienna University of Technology, 2012.

[11] C. Collette, K. Artoos, A. Kuzmin, M. Sylte, M. Guinchard, and C. Hauviller, "Active control of quadrupole motion for future linear particle colliders," in *Proceedings of the Twelfth IASTED International Conference on Intelligent Systems and Control ISC2009, Cambridge, USA*, 2009.

[12] C. Collette, S. Janssens, and D. Tshilumba, "Control strategies for the final focus of future linear particle collider," *Nuclear instruments and Methods in Physics Research*, vol. 648, pp. 7–17, 2012.

[13] C. Collette, K. Artoos, M. Guinchard, and C. Hauviller, "Seismic response of linear accelerators," *Physical Review Special Topics, Accelerators and Beams*, vol. 13/072801, 2010.

[14] A. Patapenka and Mallows, "Estimation of potential radiation damage to electronic units in the main linac tunnel," CERN, CLIC note 1028, 2014.

[15] S. Mallows and T. Otto, "Update on radiation estimates for the CLIC main and drive beams," in *CLIC Operations and Machine Protection Working Group meeting*, 2010.

[16] D. Schubert, A. Beard, S. Shedd, M. Earles Jr., and A. Von Flotow, "Stiff actuator active vibration isolation system," United States of America Patent 5,823,307, 1997.

[17] D. Schubert, A. Beard, and A. von Flotow, "A practical product implementation of an active/passive vibration isolation," *SPIE*, vol. 2264, pp. 38–49, 1994.

[18] H. Hanieh, "Active isolation and damping of vibrations via Stewart platform," Ph.D. dissertation, University of Brussels, 2004.

[19] G. Franklin, J. Powell, and A. Emami-Naeini, *Feedback Control of Dynamic systems (5th edition)*. Pearson Prentice Hall, 2006.

[20] C. Collette, S. Janssens, and K. Artoos, "Review of active vibration isolation strategies," *Recent Patents on Mechanical Engineering*, vol. 4, pp. 1–8, 2011.

[21] M. Vervoordeldonk and H. Stoutjesdijk, "Recent developments of AIMS, a novel active isolation concept," in *6th Euspen International Conference*, no. 6th. Euspen, May 2006.

[22] M. Vervoordeldonk, T. Ruijl, and R. Rijs, "Development of a novel active isolation concept," in *ASPE 2004 Spring Topical Meeting*, 2004.

[23] A. Kastelijn, T. van den Dool, R. Rufus, and R. Zuljar, "An active vibration isolation system having an inertial reference mass," United States of America Patent WO 2009/084 963 A1, 2009.

[24] K. Kar-Leung Miu, "A low cost, dc-coupled active vibration system," Ph.D. dissertation, Massachusetts Institute of Technology, 2008.

[25] A. Preumont, *Vibration Control of Active Structures An Introduction (2nd edition)*. Kluwer Academic Publishers, 2002.

[26] G. Franklin, J. Powell, and A. Emami-Naeini, *Feedback Control of Dynamic systems (3rd edition)*. Upper Saddle River, New Jersey: Addison-Wesley Publishing Company Inc., 1994.

[27] P. Nelson, "An active vibration isolation system for inertial reference and precision measurement," *Review of Scientific Instruments*, vol. 62-9, pp. 2069–2075, 1991.

[28] P. Saulson, "Vibration isolation for broadband gravitational wave antennas," *Review of Scientific Instruments*, vol. 55-8, pp. 1315–1320, 1984.

[29] C. Montag, "Active stabilization of mechanical quadrupole vibrations in a linear collider test facility," Ph.D. dissertation, Hamburg University, 1996.

[30] "Etude des vibrations et de la stabilisation a l'echelle sous-nanometrique des doublets finaux d'un collisionneur lineaire," Ph.D. dissertation, Universite de Savoie, 2007.

[31] G. Bowden, "Test of stacis for active stabilization at SLAC." [Online]. Available: G:\Workspaces\c\CLICstab\Christophe\documentation\ok_isolation\TMC\BowdenGMtalk.pdf

[32] S. Allison, L. Eriksson, J. Frisch, L. Hendrickson, T. Himel, K. Luchini, and Seryi, "Active vibration suppression r+d for the next linear collider," in *Proceedings of the 2001 Particle Accelerator Conference*, 2001.

[33] J. Frisch, L. Hendrickson, T. Himel, and A. Seryi, "Active vibration suppression R&D for the NLC," in *8th International Conference on Accelerator & Large Experimental Physics Control Systems*, 2005.

[34] R. Amirikas, A. Bertolini, and Bia, "Vibration stability studies of a superconducting accelerating module quadrupole operating at 4.5 k," in *Proceedings of PAC07*, 2007.

[35] R. Amirikas, A. Bertolini, and W. Bialowons, "Vibration stability studies of a superconducting accelerating module at room temperature and at 4.5 K," in *Linear Collider Workshop*, 2007.

[36] A. Stochino, B. Abbot, Y. Aso, M. Barton, A. Bertolini, V. Boschi, D. Coyne, R. DeSalvo, C. Galli, C. Huang, A. Ivanov, S. Marka, D. Ottaway, and V. Sannibale, "The Seismic Attenuation System (SAS) for the Advanced LIGO gravitational wave interferometric detectors," *Nuclear Instruments and Methods in Physics Research Section A: Accelerators, Spectrometers, Detectors and Associated Equipment*, 2009.

[37] A. Preumont, *Mechatronics: Dynamics of Electromechanical and Piezoelectric Systems*. Dordrecht, The Netherlands: Springer, 2006, no. ISBN-10 1-4020-4695-2.

[38] G. Clayton and S. Winder, *Operational amplifiers*. Newnes, 2003.

[39] C. Collette, S. Janssens, P. Fernandez-Carmona, and Artoos, "Inertial sensors for low-frequency seismic vibration measurement," *Bulletin of the Seismological Society of America*, vol. 83 no. 4, pp. 747–749, 2012.

[40] X. Roset, J. del Rio, A. Manuel, and R. Palomera-Garcia, "Contributions to model characterization of geophone sensor," in *Instrumentation and Measurement Technology Confcrence IMTC*, 2004.

[41] A. Pazos, G. Alguacil, and J. M. Davila, "A simple technique to extend the bandwidth of electromagnetic sensors," *Bulletin of the Seismological Society of America*, 2005.

[42] J. Havskov, "Overview of seismic instruments," in *High Quality Seismic Stations and Networks for Small Budgets, Volcan, Panama*, 2004.

[43] "Gs-1 low frequency seismometer," Geospace Technologies, Tech. Rep., February 2012. [Online]. Available: http://www.geospace.com/tag/gs-1-low-frequency-seismometer/

[44] "Gs-11d geophone data sheet," Geospace Technologies, Tech. Rep., February 2012. [Online]. Available: http://www.geospace.com/geophones-gs-11d/

[45] "Analog seismometers: Geophone sensors," Sercel, Tech. Rep., 2012. [Online]. Available: http://www.sercel.com/products/Lists/ProductSpecification/analog-seismic-sensors-specifications-Sercel-Geophone.pdf

[46] Secrel website. [Online]. Available: http://www.sercel.com/en/

[47] "Sm-4 geophone element," Sensor Nederland/ ION, Tech. Rep., 2012. [Online]. Available: http://www.iongeo.com/content/includes/pdfs/SM4_121013.pdf

[48] "Input/output inc., sm-6 geophone," Sensor Nederland, Tech. Rep., 1999. [Online]. Available: http://www.iongeo.com/content/includes/pdfs/SM6_121026.pdf

[49] Kinemetrics Inc. [Online]. Available: http://www.kinemetrics.com/

[50] Guralp catalogue 2010. [Online]. Available: http://www.guralp.com/products

[51] PMD Scientific Inc. [Online]. Available: http://www.eentec.com

[52] C. Adophsen and R. Aiello, "Zeroth-order design report for the next linear collider," SLAC report 474, Tech. Rep., 2006.

[53] A. Barzilai, T. VanZandt, and T. Kenny, "Technique for measurement of the noise of a sensor in the presence of large background signals," *Review of Scientific Instruments*, vol. 69, pp. 2767–2773, 1998.

[54] R. Pallas-Areny and J. Webster, *Sensors and signal conditioning.* John Wiley & Sons, 2001.

[55] J. Rowan, S. andHough and D. Crooks, "Thermal noise and material issues for gravitational wave detectors," *Physics Letters A*, vol. 347:25–32, 2005.

[56] G. van der Poel, "An exploration of active hard mount vibration isolation for precision equipment," Ph.D. dissertation, University of Twente, 2010.

[57] L. Holcomb, "A direct method for calculating instrument noise levels in side-by-side seismometer evaluations," United States Department of the Interior Geological Survey, Tech. Rep. Technical Report 89-214, 1989.

[58] P. Rodgers, "Self-noise spectra for 34 common electromagnetic seismometer/preamplifier pairs," *Bulletin of the Seismological society of America*, 1994.

[59] C. Montag, "Active stabilization of mechanical quadrupole vibrations for linear collider," *Nuclear Instruments and Methods in Physics Research A*, vol. 378, pp. 396–375, 1996.

[60] *P-225, P-235 PICA Power Piezo Stack Actuators Preloaded High-Load Piezo Actuators (HVPZT) w/ Sensor Option*, Physik Instrumente (PI) GmbH & Co, 2010, http://www.physikinstrumente.com/en/products/prorder.php?sortnr=101750.

[61] F. Acernese, G. Giordano, R. Romano, R. D. Rosa, and F. Barone, "Tunable mechanical monolithic sensor with interferometric readout for low frequency seismic noise measurement," *Nuclear Instruments and Methods in Physics Research*, vol. A, pp. 617:457–458, 2008.

[62] Attocube systems ag. [Online]. Available: http://www.attocube.com/

[63] C. Collette, K. Artoos, A. Kuzmin, S. Janssens, M. Sylte, M. Guinchard, and C. Hauviller, "Active quadrupole stabilization for future linear particle colliders," *Nuclear Instruments and Methods in Physics Research A*, vol. 621, pp. 71–78, 2010.

[64] C. Collette, S. Janssens, K. Artoos, A. Kuzmin, P. Fernandez-Carmona, M. Guinchard, R. Leuxe, and C. Hauviller, "Nano-motion control of heavy quadrupoles for future particle colliders: An experimental validation," *Nuclear Instruments and Methods in Physics Research*, vol. 643, pp. 95–101, 2011.

[65] *RW   Type   BK1   bellows*,   2010,   http://www.rw-america.com/products/bellows$_c$ouplings/bk/.

[66] M. Esposito, K. Artoos, P. Fernandez-Carmona, R. Leuxe, and S. Janssens, "Development of advanced mechanical systems for stabilization and nano-positioning of CLIC main beam quardupoles," in *IWAA*, 2012.

[67] K. Artoos, P. Fernandez-Carmona, M. Guichard, and S. Janssens, "Study of the electronics architecture for the mechanical stabilisation of the quadrupoles of the CLIC linear accelerator," *JINST*, vol. 5 C11014, pp. 1–9, 2010.

[68] R. C. Dorf, *Modern control systems*.   New Jersey, USA: Pearson education, 2011, no. ISBN 978-0-13-138310-4.

[69] P. Fernandez-Carmona, *CLIC stabilization hybrid controller v2 manual*, edms:1236325 ed., CERN, 2010.

[70] P. Fernandez-Carmona, K. Artoos, C. Collette, M. Esposito, M. Guichard, S. Janssens, A. Kuzmin, and R. Moron Ballester, "Study of the hybrid controller electronics for the nano-stabilization of mechanical vibrations of CLIC quadrupoles," *JINST*, vol. doi:10.1088/1748-0221/6/12/C12023, pp. 1–11, 2011.

[71] R. Schmidt, G. Schitter, and J. Van Eijk, *The Design of High Performance Mechatronics: High-Tech Functionality by Multidisciplinary System Integration*.   IOS Press, 2011.

[72] E. Anderson, D. Leo, and Holcom, "Ultraquiet platform for active vibration isolation," in *Proc. of SPIE Vol. 2717, Smart Structures and Materials*, 1996.

[73] E. Anderson, J. Fumo, and R. Erwin, "Satellite ultraquiet isolation technology experiment (suite)," in *IEEE Aerospace conference , Big Sky, Montana*, 2000. [Online]. Available: IEEEXplore13_bis.pdf

[74] R. Sugahara, M. Masuzawa, and H. Yamaoka, "Performance of an active vibration isolation system," in *IWAA2004*, 2004.

[75] K. Lan, J. Yen, and J. Kramar, "Active vibration isolation for a long range scanning tunneling microscope," *Asian Journal of Control*, vol. 6.2, pp. 179–187, 2004. [Online]. Available: 3Na-03-07.pdf

[76] Sixmoons, "Industry features," Tech. Rep., 2005, http://www.6moons.com/industryfeatures/he2005/4.html.

[77] J. Holterman and T. de Vries, "Active damping within an advanced microlithography system using piezoelectric smart discs," *Mechatronics*, vol. 14, pp. 15–34, 2004.

[78] J. Spanos, Z. Rahman, and G. Blackwood, "A soft 6-axis active vibration isolator," in *Proceedings of the American Control Conference, Seatle, Washington*, 1995.

[79] J. Fochage, T. Davis, J. Sullivan, T. Hoffman, and D. A., "Hybrid active/passive actuator for spacecraft vibration isolation and suppression." in *SPIE, 2865:104122*, 1996.

[80] J. E. McInroy, "Modeling and design of flexure jointed stewart platforms for control purposes," *IEEE/ASME T*, vol. 7, pp. 95–99, 2002.

[81] LIATO, "Active vibration isolation systems mod 1m dp6," LInks and Associated with Technology Orient (LIATO), Tech. Rep., http://www.liato.co.kr/halcyonics.htm.

Appendix A

Literature overview of vibration isolation benches

A.1 Velocity feedback systems

Two vibration isolation benches were found in the literature, to have mainly a velocity feedback as was described in Fig. 2.1 (top middle panel). Their applications are mainly related to the space industry as it is easy to get a low first resonance frequency in zero gravity, resulting in a high bandwidth for the passive isolation. The velocity or Sky-hook controller is then used to reduce the resonance peak. An overview of the two systems found is shown in Table A.1.

	Ultra quiet platform	SUIT
References	[72]	[73]
Payload mass	10-20 kg	6.2 kg
Actuator	Electro-magnetic	Piezo-actuator with soft spring
First mode	N/F	30 Hz
Sensors	Geophones	Geophones
Configuration	Hexapod	Hexapod
Collocation	Yes	Yes

Table A.1: *Summary table for velocity feedback systems found in literature. (N/F: Not Found)*

A.2 Acceleration feedback systems

Acceleration feedback is used to add virtual mass to the system and hence reduce the first resonance mode, as was explained in section 2.3. This allows for a larger vibration isolation bandwidth behind the now lower resonance frequency. An overview of existing vibration isolation tables using mainly acceleration feedback is shown in Table A.2

	KEK	Molecular measuring machine	MOD-1M Plus
References	[74]	[75]	[76]
Payload mass	500 kg	N/F	20 kg
Actuator	Pneumatic	Piezo-actuator with rubber	Electro-magnetic
First mode	3 Hz	N/F	N/F
Sensor	Accelerometers	Accelerometers	Accelerometers
Configuration	8 actuators	Mallock shell	90 degree angles
Collocation	N/F	Yes	Yes

Table A.2: *Summary table for acceleration feedback systems found in literature. (N/F: Not Found)*

A.3   Force feedback systems

An alternative way to perform acceleration feedback is by using a force sensor. This helps to ensure that an alternating pattern of poles and zeros is kept for structures with a flexible appendage. An overview of different systems using force feedback is shown in Table A.3.

	PALM	JPL hexapod	Honeywell hexapod
References	[77]	[78]	[79]
Payload mass	N/F	N/F	N/F
Actuator	Piezo-actuator	Electro-magnetic	Electro-magnetic
First mode	100 Hz	10-20 Hz	3 Hz
Sensor	Force sensor	Force sensor	Force sensor
Configuration	Hexapod	Hexapod	Hexapod
Collocation	Yes	Yes	Yes
	Univ. Wyoming	ULB soft hexapod	ULB stiff hexapod
References	[80]	[18]	[18]
Payload mass	N/F	N/F	N/F
Actuator	Electro-magnetic	Electro-magnetic	Piezo-actuator
First mode	15 Hz	N/F	N/F
Sensor	Force sensor	Force sensor	Force sensor
Configuration	Hexapod	Hexapod	Hexapod
Collocation	Yes	Yes	Yes

Table A.3: *Summary table for force feedback systems found in literature. (N/F: Not Found)*

A.4   Reverse engineering of a commercial stabilization table

In order to better understand the workings of vibration isolation tables, a commercial vibration isolation table was opened and tests were performed.

A.4.1   Table description

A picture of the Halcyonics MOD-1M Plus vibration isolation system is shown in Fig. A.1 (right panel). Eight piezo electric accelerometers measure the input energy and 8 electro dynamic actuators use this information to aid the stabilization capabilities [76]. A single degree of freedom representation of the working principle is shown in Fig. A.1 (left panel).
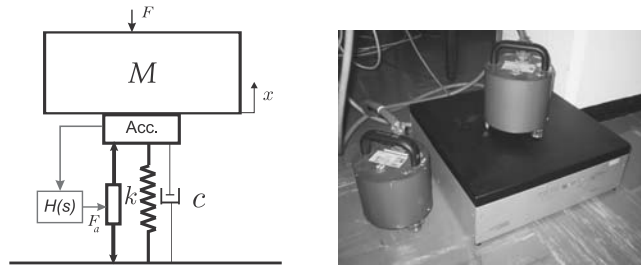

Figure A.1: *Model of a stabilization system (left panel); Photo of the table with the Guralp T6 seismometers (right panel).*

The specifications of the table are shown in Table A.4.

	Range	Units
Frequency Range	0.6 to ∞	Hz
Active corrective forces	vert: ± 8 hor: ± 4	N
System noise	< 50	ng/$\sqrt{\text{Hz}}$ (0.1-200 Hz)
Static compliance ($1/k$)	8	μm/N all directions
Own mass (M)	27.5	kg

Table A.4: *Properties of the Halcyonics MOD-1M Plus vibration isolation system [81]*

The vibration isolation system was opened to better understand the configuration of the actuators inside. Fig. A.2 (left panel) shows a frontal view of the system with the side panel opened. It shows that there are vertical actuators in the corners of the plate and horizontal actuators positioned at 90 degrees difference from the actuator next to it forming a cubic configuration. A schematic top view is shown in Fig. A.2 (right panel).
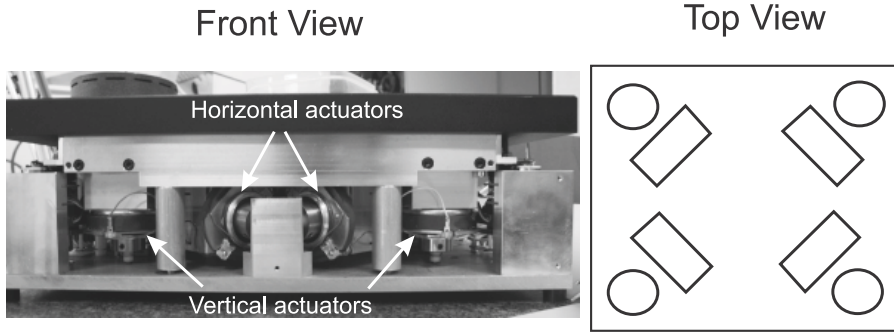
Figure A.2: *Front view of the actuator system inside the Halcyonics MOD-1M Plus (left panel); schematic representation of the top view for the Halcyonics MOD-1M Plus (right panel).*

Load compensation is performed with springs in the four corners of the plate as is shown in Fig. A.3 (left panel). The springs can be tensioned by a motor which, through gears and a threaded bolt, moves up the bottom connection point compressing the spring which applies a counter force to the weight as is shown in Fig. A.3 (right panel). The position of the spring is monitored by a position sensor.
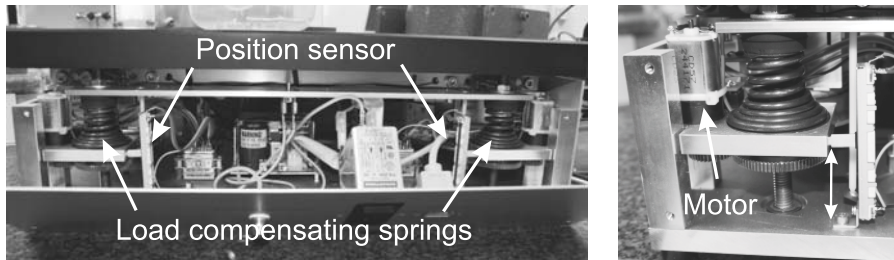

Figure A.3: *Front view of the load compensating system inside the Halcyonics MOD-1M Plus (left panel); zoom on one of the load compensating systems for the Halcyonics MOD-1M Plus (right panel).*

A.4.2   Test results

A test was performed in the Mechanical Measurement laboratory at CERN. The table was put on a flat surface and a seismometer was put on the table and one on the floor. The power spectral density for the floor (Φ_w), the table (Φ_x) measured with the Guralp seismometer, the noise curve of the Halcyonics table 50 ng/$\sqrt{\text{Hz}}$ integrated twice (Φ_n) and the noise curve of the Guralp (Φ_{ngur}) is shown in Fig. A.4.
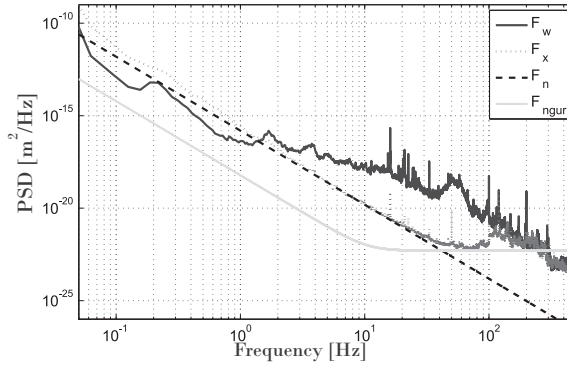
Figure A.4: *Power spectral density of the measurement on the floor* (Φ_w) *and on the table* (Φ_x) *by the Guralp seismometer, the theoretical noise curve of 50 ng/$\sqrt{\text{Hz}}$ two times integrated and the noise curve of the Guralp T6 seismometer*

Fig. A.4 shows that the PSD curve for the stabilized table Φ_x touches the given noise curve of the system. This is confirmed by calculating the coherence γ between the ground signal and the measured vibrations on the stabilization table:

$$\gamma = \frac{|\Phi_{xw}|^2}{\Phi_{xx}\Phi_{ww}}. \tag{A.1}$$

The coherence is shown in Fig. A.5. The low coherence suggests that the stabilization hits the noise curve as noise is largely uncorrelated while an attenuated signal would be still coherent with the original signal.
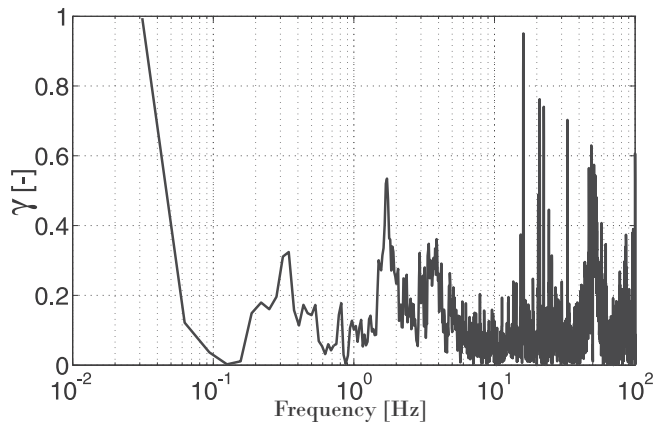

Figure A.5: *The coherence γ between the ground motion w and the motion of the plate x.*

The transfer function is calculated with:

$$T_{wx} = \frac{\Phi_{xw}}{\Phi_{ww}}. \tag{A.2}$$

The transfer function between the measured ground motion w and the measured motion on top of the stabilization table x is shown in Fig. A.6 as a solid curve. The dashed curve represents the transfer function for when the control is off. The dotted curve represents a simulation of a possible control circuit combining a velocity and an acceleration feedback.
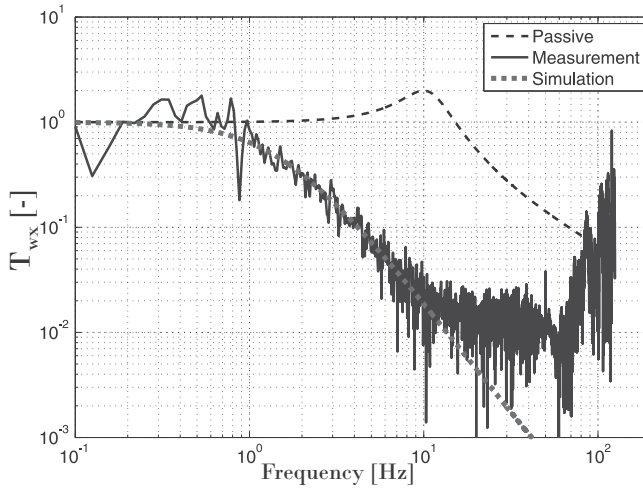

Figure A.6: *The transfer function between the ground motion w and the plate x for the measurement results (solid curve), the passive system (dashed curve) and a simulation with a velocity and acceleration feedback (dotted curve).*

Testing and opening the commercial Halcyonics MOD-1M Plus stabilization table has shown that it uses a cubic configuration for the actuators in order to perform stabilization in both vertical and lateral direction. The stabilization is limited by the noise performance of the accelerometer.